# TOWARD A BETTER UNDERSTANDING OF METEOROLOGY-CHEMISTRY CONNECTION USING REGIONAL MODELLING WITH IMPROVED ATMOSPHERIC CHEMISTRY MODULE

A Dissertation

by

XIAOKANG WU

Submitted to the Office of Graduate and Professional Studies of
Texas A&M University
in partial fulfillment of the requirements for the degree of

DOCTOR OF PHILOSOPHY

| | |
|---|---|
| Chair of Committee, | Yangyang Xu |
| Committee Members, | John W. Nielsen-Gammon |
| | Timothy Logan |
| | Qi Ying |
| Head of Department, | Ramalingam Saravanan |

December 2020

Major Subject: Atmospheric Sciences

# ABSTRACT

Air pollution is an ongoing worldwide problem especially for developing countries. In South Asia, Future projection has shown potentially no slow-down of enhanced emissions (RCP 8.5), while meteorology, a factor may help regulate the local pollution levels, tends to change in the future as well. We identified three key variables: U10, T200 and PBLH that are highly correlated with local pollution levels in India and constructed Hazy Weather Index for India (HWII). HWII helps build a statistical projection model to evaluate the contribution from climate change side. The results suggest that a more favorable atmospheric environment is expected for pollution dispersion in the future, however, such condition is likely to be overwhelmed by enhanced emissions.

In addition to air pollution, heat has raised great concerns in public health field. Based on a model simulation, here we show that when daily average wet-bulb temperature of 25 °C is taken as the threshold for severe health impacts, heat extremes frequency averaged over South Asia increases from 45 days/year in 1997–2004 to 78 days/year in 2046–2054 under RCP8.5 scenario. Even more concerning is the joint occurrence of the heatwave and high-PM hazard (HHH), which would have substantial increases of 175% in frequency and 79% in duration. The alarming increases in just a few decades pose great challenges to adaptation and call for more aggressive mitigation.

Simulations above were conducted using MOZART-MOSAIC chemistry module. Despite being a comprehensive chemistry suite, MOZART-MOSAIC simulations are computationally expensive, making a large area resolution simulation less practical. A modal aerosol module with three lognormal modes (MAM3) was developed by Ma et al., (2014) but suffers two major

deficiencies: (1) the biomass burning emission is ignored and (2) no mechanism that converts VOC to SOA. We perform six simulations (WRF-CAM5) to show progressive improvements in the model against various validation benchmarks.

We tested our updated WRF-CAM5 for cloud-aerosol interactions off the US west coast. We show that the aerosol compositions and distributions play a significant role in regulating the cloud fraction and effective radius in the region.

ACKNOWLEDGEMENTS

I would like to thank my committee chair, Dr. Xu, and my committee members, Dr. Nielsen-Gammon, Dr. Logan, and Dr. Ying for their guidance and support throughout the course of this research.

Thanks also go to my friends and colleagues and the department faculty and staff for making my time at Texas A&M University a great experience.

Finally, thanks to my mother and father for their encouragement.

# CONTRIBUTORS AND FUNDING SOURCES

## Contributors

This work was supervised by a dissertation committee consisting of Dr. Yangyang Xu, Dr. John Nielsen-Gammon, Dr. Timothy Logan and Dr. Qi Ying.

The sources of data are described in each chapter.

## Funding Sources

This work is supported by National Science Foundation. Grant Number: AGS-1841308.

Part of the content in this dissertation is reprinted with modifications and permissions from the following papers:

Wu, X., Xu, Y., Kumar, R., & Barth, M. (2019). Separating Emission and Meteorological Drivers of Mid-21st-Century Air Quality Changes in India Based on Multi year Global-Regional Chemistry-Climate Simulations. Journal of Geophysical Research: Atmospheres, 124(23), 13420-13438.

Xu, Y., Wu, X., Kumar, R., Barth, M., Diao, C., Gao, M., ... & Meehl, G. A. (2020). Substantial Increase in the Joint Occurrence and Human Exposure of Heatwave and High-PM Hazards Over South Asia in the Mid-21st Century. AGU Advances, 1(2), e2019AV000103.

NOMENCLATURE

| | |
|---|---|
| CAM-Chem | Community Atmosphere Model with Chemistry |
| CBMZ | carbon-bond mechanism type Z |
| FINN | Fire INventory from NCAR |
| HHH | heatwave and high-PM hazards |
| HWII | Hazy Weather Index for India |
| MAM3 | modal aerosol module with 3 bins |
| MBL | marine boundary layer |
| MERRA | Modern-Era Retrospective analysis for Research and Applications |
| MOSAIC | Model of Simulating Aerosol Interactions and Chemistry |
| MOZART | Model for Ozone and Related Tracers |
| NCAR | National Center for Atmospheric Research |
| PBLH | planetary boundary layer height |
| PM | particulate matter |
| RCP | Representative Concentration Pathway |
| T | temperature |
| T200 | temperature at 200 hPa |
| Tw | wet bulb temperature |
| U10 | zonal wind at 10m above the surface |
| WRF-Chem | Weather Research and Forecasting model coupled with Chemistry |
| YSU | Yonsei University |

TABLE OF CONTENTS

LIST OF FIGURES

LIST OF TABLES

# CHAPTER I

# INTRODUCTION

Air pollution is currently one of the major health risks along with high blood pressure, tobacco smoking, unsanitary water, and undernutrition (Lim et al., 2012; Lelieveld et al., 2015). Air pollutants include ozone (with its precursors of nitrogen oxides, carbon monoxide, and volatile organic compounds) and particulate matter (PM). Fine particles, i.e., PM with aerodynamic diameter of less than 2.5 μm ($PM_{2.5}$), have raised great concerns, because they can infiltrate the respiratory system and damage human body (Tecer et al., 2008). Growing population exposure to exacerbated $PM_{2.5}$ levels has become a serious public health concern worldwide. It is estimated that six million global annual premature deaths were PM-related (Lelieveld et al., 2015). For many developing countries, excessive amounts of population exposures to $PM_{2.5}$ are especially alarming due to their large population and fragile health care systems (Cohen et al., 2005; Cohen et al., 2017). In China, $PM_{2.5}$ is estimated to have contributed to 1.6 million premature deaths annually, which accounts for 17% of the total deaths (Rohde and Muller, 2015). Similarly, in India, $PM_{2.5}$-related diseases caused an estimated 1.1 million premature deaths in 2012 (David et al., 2019) and 2015 (Cohen et al., 2017; Lelieveld., 2017; Conibear et al., 2018a;) along with 1.24 million premature deaths in 2017 (Balakrishnan et al., 2017).

South Asia is home to more than 1.5 billion people and is under rapid economic growth with an expected population of 2 billion by the mid-21st century (Jones and O'Neil, 2016; Table 1). Among various environmental stresses, two prominent threats are heat extremes (Dash and

Mamgain, 2011) and air quality degradation (Li et al., 2017), both of which are reported to lead to major public health crises (Azhar et al., 2014; Chowdhury et al., 2018).

Table 1. The population of seven nations within South Asia in the Decade 2000 and Decade 2050. Reprinted from Xu et al., (2020).

| | Population (million people) | |
|---|---|---|
| | Decade 2000 | Decade 2050 under SSP5 |
| Afghanistan | 22.1 | 57.3 |
| Bangladesh | 133.5 | 167.8 |
| Bhutan | 2.3 | 1.2 |
| India | 989.1 | 1518.7 |
| Nepal | 23.4 | 43.2 |
| Pakistan | 144.1 | 247.5 |
| Sri Lanka | 17.5 | 19.5 |
| South Asia | 1332.0 | 2055.1 |

Similar to air pollution, heat extremes adversely impact human health by affecting respiratory and cardiovascular systems (e.g. Meehl et al., 2018). The heat hazard for human health is preferably quantified in humidity-related temperature indices (Kovats and Hajat, 2008), such as wet-bulb temperature (Sherwood and Huber, 2010) or heat index (Anderson et al., 2013). These indices are related to the efficacy of releasing heat from the skin to regulate body temperature.

Recent global climate model-based assessments show that the probability of reaching certain critical thresholds (jointly defined using temperature and relative humidity) empirically known to be life-threatening, will continue to rise, especially over South Asia (e.g. Mora et al., 2017) because of the lower climate variability and the higher background humidity. The South Asia region is projected to experience more frequent heat extremes with longer duration and enhanced severity in the future (Russo et al., 2017), which is consistent with observed trends during the past few decades (Pai et al., 2004; Alexander et al., 2016; Dash and Mamgain, 2011; Basha et al., 2017; Yin and Sun, 2018; Khan et al., 2019).

Accurate model simulations of both meteorological and chemistry fields are crucial for studies of heat extremes and air pollutions. Proper numerical representation of atmospheric chemistry calls for accurate juxtaposition and coupling of both meteorology and chemistry processes (Brasseur and Jacob, 2017). There is an intrinsic tradeoff between the comprehensiveness of the model and the computational efficiency (or the availability of computational resources) (Peckham, 2012). A more complicated chemistry scheme generally, albeit not always, has more realistic representations of atmospheric chemistry when compared to a relatively simpler counterpart, because the former scheme considers more species and tracks more reactions that take place (Phoenix et al., 2017). However, comprehensive chemistry modules are less practical for regional simulations over a large domain or for global climate modeling. Since the chemical feedback from the meteorological side is usually non-linear (and vice versa), a realistic representation of both processes is crucial to yield reliable results.

For climate-chemistry models, one of the great challenges for reliable simulations and projections comes from the accurate estimation of cloud radiative effects (Slingo and Palmer, 2011). Among all cloud types, marine boundary layer (MBL) clouds play a crucial role in

regulating Earth's energy Budget (Bony and Dufresne). Due to its high brightness compared to the radiatively dark ocean background, MBL clouds serve the prominent role in back reflecting the incoming solar radiation to space (McFiggans et al., 2000). Despite being an indispensable component in modulating the earth's climate, yet MBL clouds remain as one of the largest uncertainties in future climate projections (Bennartz, 2007). This is because the presence of MBL cloud does not have strong impacts towards longwave cooling rates as the temperature differences are generically low between the surface of the ocean and top of the cloud (Meyer et al., 2013). However, the MBL clouds tend to have significant shortwave radiative impacts (Ahlgrimm et al., 2018) and their future changes remain uncertain (Diaz et al., 2019). Therefore, despite being clear that MBL has net cooling effects for Earth's energy budget, it is debatable that whether MBL clouds' contribution in the future will trend up or down and accordingly, resulting in an uncertain net positive or negative energy contributions to the future Earth's atmosphere.

This dissertation is separated into two parts with four chapters. The first two chapters (Part I) are mostly from two published works (Wu et al., 2019; Xu et al., 2020) and the latter two are based on a model-improvement framework with preliminary analyses of cloud properties and aerosol interactions.

CHAPTER II

# AIR POLLUTION IN INDIA AND ITS INTERACTIONS WITH METEOROLOGY[1]

## 2.1 Introduction

Air pollution in megacities is a longstanding and ongoing problem mainly due to concentrated anthropogenic emissions from transportation and industrial activities, and a lack of effective mitigation measures (Molina and Molina, 2004). For India, the future of urban air pollution problem is especially concerning, because of rapidly expanding urban areas and fast population growth (James, 2011). For example, Delhi is projected to have a 39% increase in premature deaths in future due to excessive $PM_{2.5}$ exposures (Chowdhury and Dey, 2016).

It has long been appreciated that anthropogenic emission sources constitute a critical component for degradation of urban air quality (Querol et al., 2001). Meteorological conditions, however, could also play crucial roles in governing the transport, dispersion and removal of air pollutants (Arya, 1999). For example, ozone variability over Europe has been linked to North Atlantic Oscillation (NAO; Creilson et al., 2003; Doherty et al., 2013) and Arctic Oscillation (AO; Lamarque and Hess, 2004). Ozone variability over the Northern Hemisphere mid-latitudes has also been associated with the El Nino Southern Oscillation (ENSO) variability (Koumoutsaris et al., 2008; Ziemke et al., 2010), especially in the middle and upper troposphere (Langford et al., 1998).

[1] Reprinted with permission from Wu, X., Xu, Y., Kumar, R., & Barth, M. (2019). Separating Emission and Meteorological Drivers of Mid-21st-Century Air Quality Changes in India Based on Multiyear Global-Regional Chemistry-Climate Simulations. Journal of Geophysical Research: Atmospheres, 124(23), 13420-13438.

The role of meteorological variability and change in driving PM pollution is less studied than it is for ozone (Dawson et al., 2014). There is empirical evidence relating synoptic weather with local PM concentration (e.g. Eder et al., 1993; Mahmud et al., 2010; Appelhans et al., 2013), but the physical processes involved are often complex and region-dependent. Previous studies have identified several key meteorological variables that could closely influence air pollution concentration, such as temperature, humidity, wind fields, boundary layer height, clouds, solar radiation, and precipitation (Dickerson et al., 1997; Davies et al., 2007; Jacob and Winner, 2009; Tao et al., 2014; Xu and Lamarque, 2018). These meteorological variables can influence atmospheric physical and chemical processes that determine the formation, transport, dispersion and removal of air pollution. Therefore, quantifying these meteorological variables and their roles in driving air pollution distribution, which might change under future global warming, can provide critical information to more effectively develop the long-term adaptation and regulatory measure. A number of studies focusing over the United States have highlighted the roles of synoptic scale processes (e.g. Fischer et al., 2010; Parrish et al., 2010; Lin et al., 2012) and mid-latitude weather systems (e.g. Tai et al., 2012; Hu et al., 2013) in affecting the surface pollution level. Similarly, the interactions between PM and meteorological conditions have been the subject of many recent studies in China (e.g. Yang et al., 2018; Zhang et al., 2018; Li et al., 2018; Chen et al., 2019). Notably, to better characterize the wintertime haze environment, Cai et al. (2017) developed a Hazy Weather Index (HWI) to link high $PM_{2.5}$ levels in Beijing with meteorological fields and demonstrated that HWI could serve as a reliable indicator for local $PM_{2.5}$ variability. Cai et al. (2017) went further to show that future global warming would induce meteorological conditions leading to higher $PM_{2.5}$ level over Beijing. The worsening effect of future global warming is consistent with a few studies at a global scale (Horton et al., 2014; Allen et al., 2016; Xu and

Lamarque, 2018). The general validity of such an undesirable future projection in pollution-related meteorological conditions, however, remains to be tested for other regions, such as South Asia, where local emission and meteorological conditions can change differently compared to the rest of the world (Lal et al., 2001; Meehl et al., 2005; Sharmila et al., 2015; Jayasankar et al., 2015).

The relative contribution of climate change and local emission sources is also worth investigating quantitatively. For example, the increase in $PM_{2.5}$ emission over India has been suggested by several recent studies to have a dominant effect over climate change in causing future degradation in air quality (Pommier et al., 2018; Venkataraman et al., 2018). But, to what direction and extent the pollution-related meteorological condition will change in future is still largely unquantified. Indian summer monsoon is well known to have a strong control over the distribution of surface pollutants over India (e.g., de Laat and Lelieveld, 2002; Lelieveld et al., 2018). However, a quantitative analysis, especially using multiple variables and a combined index, is less common in previous studies. The global-regional modeling system in Kumar et al. (2018) projects that in 2050, $PM_{2.5}$ level in South Asia will increase by 32% under Representative Concentration Pathway (RCP) 8.5, with an 8% increase in number of days exceeding World Health Organization (WHO) limits. A separation of meteorological influence, however, is not presented in Kumar et al., (2018), which is the focus of our analysis here.

Moreover, we aim to synthesize and modify the meteorological indices as suggested in previous studies (Horton et al., 2014; Cai et al., 2017) to develop a local index (hereafter referred to as Hazy Weather Index for India, HWII) that correlates better with South Asia regional pollution level. The identified key variables in the development and evaluation of HWII will also enable us to build a statistical model to predict the pollution levels based on meteorology alone and to use it to project future $PM_{2.5}$ levels with global climate models even if they do not simulate or archive

chemical output explicitly. To demonstrate the effectiveness of HWII in predicting pollution levels, we select three representative megacities (Delhi, Kolkata and Mumbai) and Indo-Gangetic plain (IGP) in India (Figure 1) due to high $PM_{2.5}$ levels and large population. Note that Mumbai and Delhi are two largest cities and Kolkata ranks at 7th in size, and the IGP region is the home to more than 400 million people.

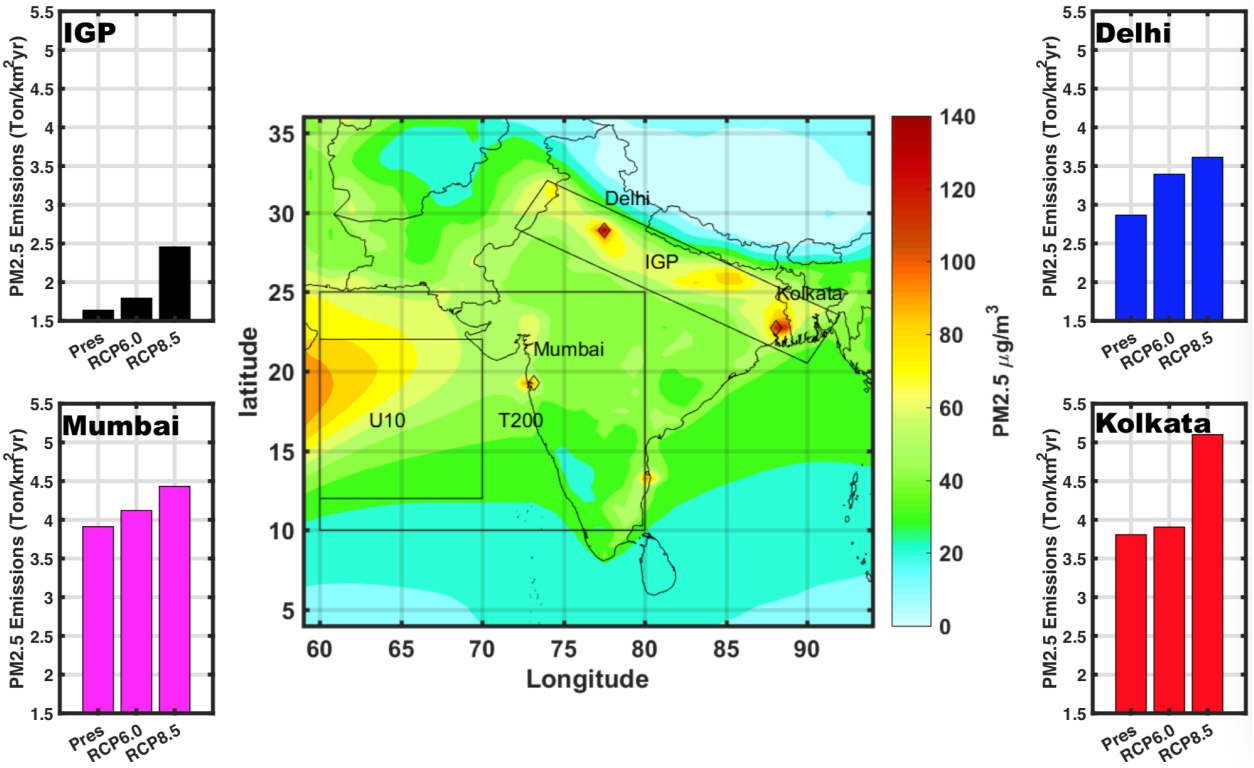


Figure 1. The domain of the simulation showing $PM_{2.5}$ surface concentration during Historical Period with three representative cities and IGP region marked. The two black boxes indicate the selected area for meteorological indicators of T200 and U10. Four side panels show local emission fluxes over three cities and IGP during the Historical Period, and Decade 2050 under two RCP scenarios (RCP6.0 and RCP8.5). Reprinted from Wu et al., (2019).

After describing the model simulations and performance, we present the temporal correlations between $PM_{2.5}$ and various meteorological variables as well as HWII. We then present the results of future projections of $PM_{2.5}$ level using a multivariate linear regression model, followed by a discussion on chemical compositions and physical mechanisms.

## 2.2 Methods

### 2.2.1 Model setup

This study utilizes multi-year air quality simulation as described in Kumar et al. (2018), using a framework called Nested Regional Climate Model coupled with Chemistry (NRCM-Chem). The regional simulation over South Asia in based on Weather Research and Forecasting (WRF) model coupled with Chemistry, version 3.6.1 (WRF-Chem 3.6.1). The WRF-Chem uses outputs from version 1 of the Community Earth System Model (CESM1) (Hurrell et al., 2013) as the meteorological initial and boundary conditions. The 1981 to 2005 CESM1 outputs are bias-corrected based on European Center for Medium-Range Weather Forecasts Interim Reanalysis (ERA-Interim, Dee et al., 2011) following the procedures described in Bruyère et al. (2014). Also, chemical initial and boundary conditions are from the global simulations of Community Atmosphere Model with Chemistry (CAM-Chem; Lamarque et al., 2012), which are available for all RCP scenarios from 1850 to 2100. The chemical boundary conditions are not bias-corrected, however, which is due to the lack of reliable dataset as benchmark. For example, when compared against in situ observations in Delhi collected during earlier 2000s, the simulated $PM_{2.5}$ has a better agreement in terms of overall magnitude and seasonal cycles, than Modern-Era Retrospective analysis for Research and Applications, Version 2 reanalysis product (MERRA2; Gelaro et al., 2017).

Next, we provide some details on the chemical schemes in NRCM-Chem configuration. The Model for Simulating Aerosol Interactions and Chemistry (MOSAIC; Zaveri et al., 2008) in four discrete size bins was selected to represent aerosol processes. MOSAIC treats black carbon aerosols as internally mixed with other aerosol species such as sulfate, ammonium, organic carbon, nitrate, sodium, chloride, methanesulfonate, calcium, carbonate, liquid water, and other inorganics (including dust) within each size bin. Thermodynamic processes such as particle deliquescence, aerosol water content, dynamic gas-particle partitioning, and solid-liquid phase equilibrium in MOSAIC are simulated using an accurate and computationally efficient module known as the Multicomponent Taylor Expansion Method (MTEM; Zaveri et al., 2005). Aerosol particles are allowed to interact with the clouds and the approach of Abdul-Razzak and Ghan (2002) is followed for activation of aerosol particles. Both dry and wet (in-cloud and impaction scavenging) deposition removes aerosol particles from the atmosphere following Binkowski and Shankar (1995) and Easter et al. (2004), respectively. The $PM_{2.5}$ concentration is calculated in NRCM-Chem codes using the equation below:

$$[PM]_{2.5} = [{SO_4}^{2-}]_{2.5} + [{NO_3}^{-}]_{2.5} + [Cl^{-}]_{2.5} + [{NH_4}^{+}]_{2.5} + [Na^{+}]_{2.5} + [BC]_{2.5} + [OC]_{2.5} + [OIN]_{2.5} + [SOA]_{2.5}$$

For gas phase tropospheric ozone chemistry, we have used the Model for Ozone and Related Tracers (MOZART) chemical mechanism (Emmons et al., 2010; Knote et al., 2014). MOZART chemical mechanism contains 143 gas phase species, which participate in 347 reactions including 49 photolysis reactions. The photolysis frequencies of trace gases are calculated using the Fast Troposphere Ultraviolet Visible scheme (Tie et al., 2005) that also allows aerosols to

affect the photolysis rates (Kumar et al., 2014). Dry and wet deposition of trace gases follow Wesely (1989) and Neu and Prather (2012), respectively.

### 2.2.2 Model Simulation

In this study, the NRCM-Chem simulation domain covers 1.53°-44.74°N and 52.58°-107.42°E with 51 vertical layers from surface up to 10 hPa. The simulation included two domains with different resolutions (60 km grid spacing for the entire domain and 12 km grid spacing for a smaller inner domain covering IGP region during the dry season. For detailed simulation set-ups and the evaluation of meteorology, ozone and related gases, readers are referred to Section 2 and Section 3 of Kumar et al., (2018). The dry season is defined as October-May and the wet (monsoon) season is defined as June-September. In this study, we mainly used the outer domain, because the high-resolution inner domain outputs did not include June to September monsoon season. However, we conducted sensitivity test for the IGP by combining the dry season high-resolution data with the wet season lower resolution data. The original hourly model outputs are available, but only daily average $PM_{2.5}$ mass concentrations are analyzed in this study.

Two temporal periods are covered in the simulation: 1997-2004 (hereafter denoted as "Historical Period") and 2046-2054 (hereafter denoted as "Decade 2050"). For Historical Period, emissions are based on the year 2000 level in the Atmospheric Chemistry and Climate Model Intercomparison Project (ACCMIP; Lamarque et al., 2011). For Decade 2050, we choose two emission scenarios of RCP6.0 and RCP8.5. RCP emission scenarios are constructed based on projection of socioeconomic development and have been extensively used in the fifth round of coupled climate model inter-comparison. Moreover, hourly climatological (2000-2014) open

biomass burning emissions are from the Fire INventory from NCAR (FINN; Wiedinmyer et al., 2011), which is based on satellite-detected fire counts at 1 km resolution.

Neither ACCMIP nor RCP emissions include emission of $PM_{2.5}$, which is required for the NRCM-Chem setup. Therefore, $PM_{2.5}$ emission is estimated from the close relationship between CO and $PM_{2.5}$ emissions in EDGAR-HTAP v2 inventory (Janssens-Maenhout et al., 2012) with a high correlation varying from 0.7 to 0.9 over South Asia. The approach of scaling total $PM_{2.5}$ emission with CO might lead to some biases in the projected $PM_{2.5}$ emission under RCP6.0, due to the projected reduction in CO emission, rather than the projected increase in other major species (Table 1 of Kumar et al., 2018). Note, however, that the species of $SO_2$, $NO_x$, BC, OC, $NH_3$ are indeed assumed to increase in our future simulation under RCP6.0, and the scaling based on future CO (decreasing by 28% over South Asia) only affects "other inorganics". Also, the local $PM_{2.5}$ emission is projected to increase in the three representative cities and IGP regions (see Figure 1). The simulated $PM_{2.5}$ surface concentrations for the Historical Period were previously evaluated against seven observational sites in South Asia and 5 out of 7 sites have a monthly mean bias of less than 10% (Kumar et al., 2018). In general, the more populous sites have more accurate simulated $PM_{2.5}$ levels than less populous sites, presumably because of a better estimate of $PM_{2.5}$ emissions in cities. The better $PM_{2.5}$ emission estimate is also potentially aided by a stronger correlation of CO and $PM_{2.5}$ due to similarity of emission sources. For example, in Delhi, the monthly mean bias is 6% with a correlation of~ 0.9, and in Hyderabad (the 4$^{th}$ largest city by population), the monthly mean bias is 2% with a correlation of 0.9. In contrast, Patiala in the state of Punjab, a relatively less populous city (compared to the other three cities in this study, but still with around half million population), has a monthly mean bias of 40%, potentially resulting from the uncertainties of local fire emission. Punjab is at the center of many agricultural burnings during

fall and spring seasons (Sharma et al., 2010), but the fire emission (FINN) in our simulation is satellite-based and has limitation in detecting small-scale agriculture-related burnings (Hawbaker et al., 2008).

Simulated aerosol optical depth (AOD) were also previously compared to the observations retrieved from Aerosol Robotic Network, and similarly, the model outputs successfully capture the high AOD over large cities. For example, in Karachi, the monthly mean bias is less than 1% with a correlation as high as 0.96. Since this study mainly focuses on urban $PM_{2.5}$ levels, such a low level of bias is considered acceptable.

## 2.3 Results

### 2.3.1 Simulated $PM_{2.5}$ and Future Changes

Figure 2 shows probability density function of daily $PM_{2.5}$ levels in the Historical Period and mid-21$^{st}$ century under two different RCP scenarios. Mean $PM_{2.5}$ concentrations (indicated by the vertical dash lines) increase in a warmer climate ("Historical Period < RCP6.0 < RCP8.5") in all cities and IGP. The changes vary in probability distribution of daily $PM_{2.5}$ level for different regions. In Delhi, the Historical Period peak is lower than Decade 2050 peaks for both scenarios. Such a difference indicates not only an increased average $PM_{2.5}$ levels but also more frequent heavy pollution days. In Kolkata, the Historical Period model peak is comparable with the RCP8.5 peak but is slightly higher than the RCP6.0 peak. However, when considering extreme polluted cases (e.g., $PM_{2.5} > 250$ μg/m$^3$), both Decade 2050 cases have higher frequency than the Historical Period. In Mumbai, despite that mean value of $PM_{2.5}$ increase only slightly under RCP6.0 and RCP8.5 (by 9%), the frequency of exceeding 200 μg/m$^3$ daily average increase by ~70% under RCP6.0 and ~260% under RCP8.5. When considering the IGP region as a whole, Historical Period

$PM_{2.5}$ has comparable mean value and probability distribution with RCP6.0 future. However, under RCP8.5 scenario, both mean value and distribution shift rightward significantly (with a 47% increase).

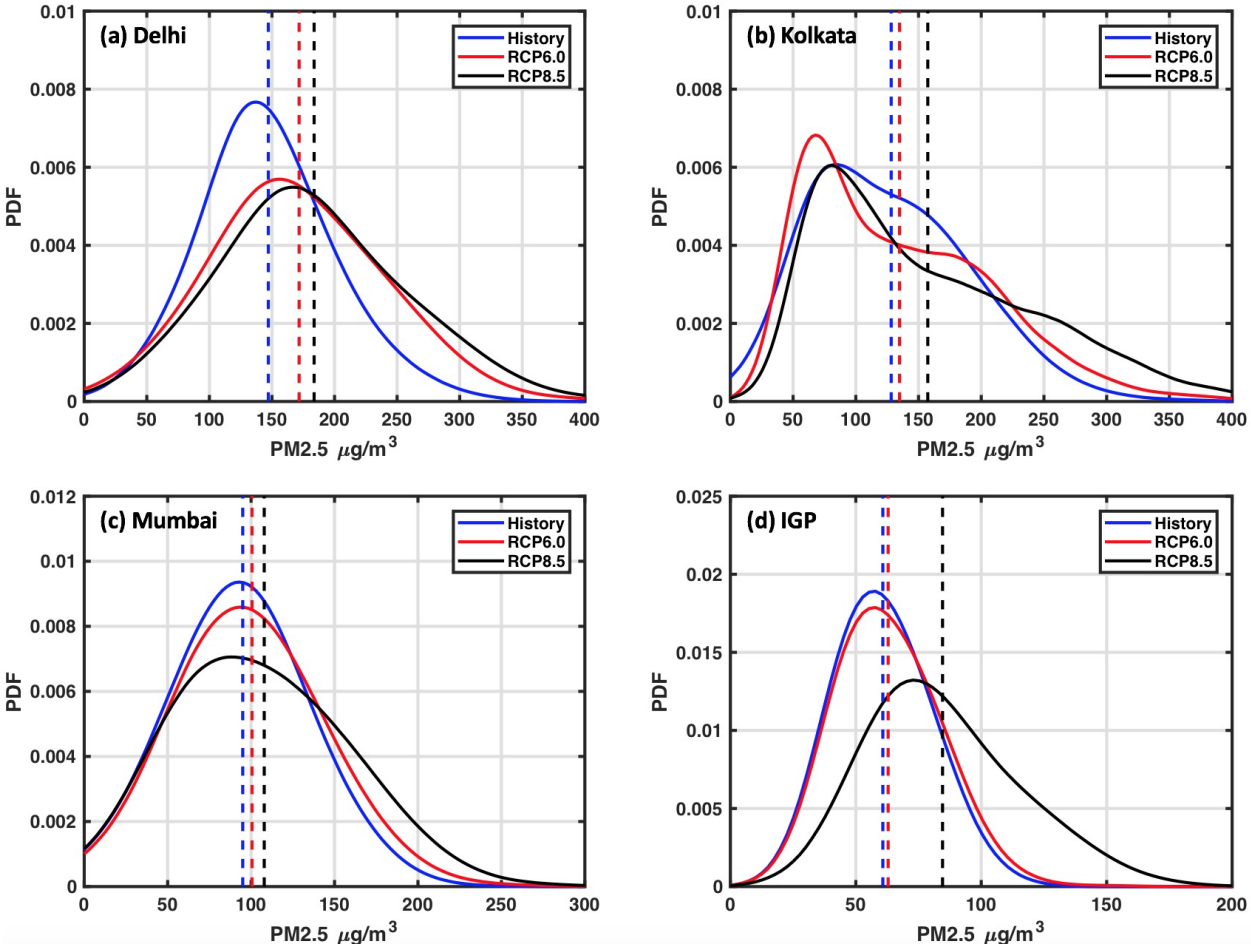


Figure 2. Probability density function (PDF) of $PM_{2.5}$ daily levels for each region ((a) Delhi, (b), Kolkata, (c) Mumbai (d) IGP). Blue curves are Historical Period levels, red curves are Decade 2050 under RCP6.0, and black curves are Decade 2050 under RCP8.5. Dashed lines are temporal average for each case. Reprinted from Wu et al., (2019).

In the RCP8.5 case, $PM_{2.5}$ levels over all three cities and IGP consistently show an increasing trend as in the entire South Asia region as discussed in Kumar et al., (2018). For RCP6.0, Kumar et al., (2018) showed an overall similar $PM_{2.5}$ levels when averaged across the

entire South Asia compared to Historical Period. But for the three megacities and IGP region examined here, $PM_{2.5}$ levels under RCP6.0 are still projected to increase from the current level by 2-11% on average (Figure 1 bar charts).

Based on the simulations here, Delhi is identified as the most polluted city (with mean $PM_{2.5}$ value at ~ 140 $\mu g/m^3$) followed by Kolkata and Mumbai, although Delhi has the lowest local emission fluxes among the three cities (~1 Ton/$km^2$/year , 35% lower than other two cities and only higher than the IGP average, Figure 1). This simple contrast at city level serves to illustrate that $PM_{2.5}$ surface concentration is not only dependent on local/regional emission, but also strongly affected by transport due to meteorological conditions and orography around the cities. Note that Delhi is sandwiched between the towering Himalayas to the north and Deccan Plateau to the South which limits meridional dispersion of emissions. While the contribution of emission is critically important and is the focus of regulatory measures, locally and nationally, the role of meteorology in meeting air quality target in the short-term (a few years) and long-term (a few decades) is often under-appreciated. As a result, there is a tendency to assume that $PM_{2.5}$ levels will respond to emission reduction, while overlooking the potential exacerbating effects of climate change (Horton et al., 2014; Cai et al., 2017; Zou et al., 2017; Chen et al., 2019). Motivated by these earlier studies, in the following sections we aim to understand the relative contribution of meteorology and emission to high $PM_{2.5}$ level, as well as their respective changes in Decade 2050.

### 2.3.2 Effectiveness and Robustness of HWII in Capturing $PM_{2.5}$ Variability

Inspired by the index developed for Beijing (Cai et al., 2017), we tested similar meteorological variables for India but found rather weak correlations. For example, the correlation between $PM_{2.5}$ and meridional wind at 850 hPa (V850) is as low as -0.17 and the correlation

between $PM_{2.5}$ and local precipitation is -0.13. A low correlation with precipitation can be attributed to the prolonged precipitation during monsoon seasons when the $PM_{2.5}$ is depleted as soon as the first rainy day occurs. Deep convection during the monsoon season also lifts aerosols to upper troposphere and lower stratosphere and reduces aerosol concentrations near the surface (Kumar et al., 2015). Therefore, we modified HWI for India (HWII) based on local meteorological features without including local precipitation as a factor. Instead, three selected meteorological variables are regional zonal wind at 10m above the surface (U10), temperature at 200 hPa (T200) and local planetary boundary layer height (PBLH). The averaging area for U10 is 12°-22°N, 60°-70°E and for T200 is 10°-25°N, 60°-80°E (smaller and larger boxes in Figure 1). U10 and T200 are robust indicators of seasonal changes in synoptic meteorology of South Asia. Local PBLH outputs from the bulk Richardson number based on Yonsei University PBL scheme (Hong et al., 2006) are considered instead of regional average, for each individual city. Similar to Cai et al. (2017), to form a simple unitless index (HWII), all three variables are first normalized and then summed as in the equation below:

$$HWII = U10_{normalized} + T200_{normalized} + PBLH_{normalized}$$

We next demonstrate the effectiveness of HWII by showing the correlation between $PM_{2.5}$ levels and HWII. Figure 3 uses Mumbai to provide an example for the Historical Period and future (under RCP8.5) temporal variability of $PM_{2.5}$, individual meteorological variables and HWII. All three weather variables are negatively correlated with the $PM_{2.5}$ levels. The correlation coefficients range from -0.5 (Historical Period PBLH, shown in Y-axis labels) to -0.64 (RCP8.5 U10). The

robust negative correlations imply a strengthened pollution dispersion mechanism should meteorological fields increase in strength with time.

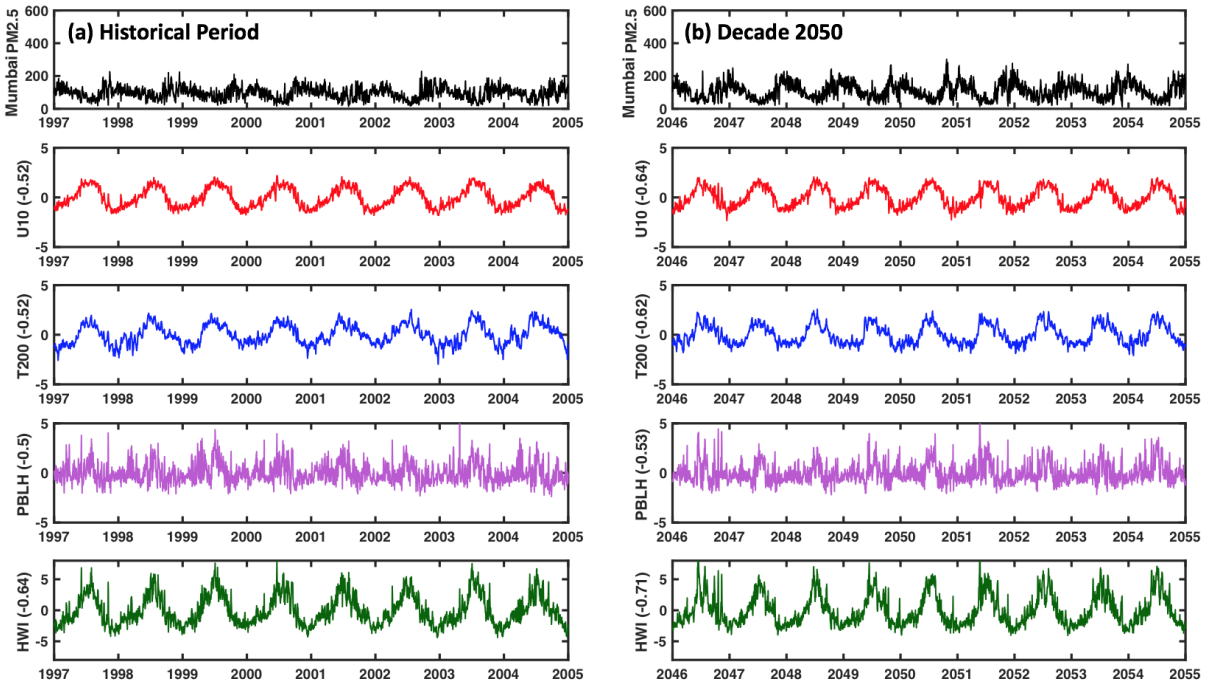


Figure 3. Daily mean $PM_{2.5}$ concentrations ($\mu g/m^3$), three normalized meteorological variables and HWII in Mumbai for (a) Historical Period and (b) Decade 2050 under RCP8.5. Values in the parenthesis of y-axis label are temporal correlations between each variable and $PM_{2.5}$ levels. Reprinted from Wu et al., (2019).

Table 2 summarized the correlation between HWII (along with three individual variables) and local $PM_{2.5}$ levels with 95% confidence intervals. All three variables are negatively correlated with $PM_{2.5}$ levels with correlation coefficients ranging from -0.45 (Delhi, Historical Period, T200) to -0.69 (Kolkata, RCP8.5, PBLH). HWII, as a composite index, usually has a better performance (r at -0.66) in capturing day-to-day $PM_{2.5}$ variability than individual variables (except for Delhi

under RCP6.0 and RCP8.5). One noteworthy point is higher (more negative) correlations with individual meteorological does not necessarily lead to a higher correlation with HWII. For example, averaged over IGP (Historical Period), the $PM_{2.5}$ correlations with three individual variables are: -0.62, -0.53, -0.54, while in Mumbai (Historical Period), the correlations are lower at -0.52, -0.52, -0.5. For IGP, the correlation of HWII (-0.63) is comparable with Mumbai (-0.64). Therefore, HWII, specifically modified for this region, serves as a useful tool to explain the variability and predict changes in $PM_{2.5}$ concentration.

Table 2. Temporal correlations with 95% confidence interval between HWII and $PM_{2.5}$ in three cities and IGP for Historical Period and Decade 2050 under the two warming scenarios. The values in the brackets indicate the lower and upper bound of confidence interval. The bottom row shows the results when the high-resolution model output over IGP during the dry season is used. Values in the parenthesis are correlations between $PM_{2.5}$ and individual U10, T200, PBLH. Reprinted from Wu et al., (2019).

| | Correlations between HWII (U10, T200, PBLH) and $PM_{2.5}$ | | |
|---|---|---|---|
| | Historical Period | RCP6.0 | RCP8.5 |
| Delhi | -0.59 [-0.61 -0.56]<br>(-0.53,-0.45,-0.58) | -0.61 [-0.63 -0.58]<br>(-0.53,-0.45,-0.63) | -0.62 [-0.64 -0.60]<br>(-0.54,-0.48,-0.64) |
| Kolkata | -0.71 [-0.73 -0.69]<br>(-0.59,-0.51,-0.65) | -0.7 [-0.71 -0.68]<br>(-0.58,-0.49,-0.69) | -0.72 [-0.73 -0.70]<br>(-0.59,-0.51,-0.69) |
| Mumbai | -0.64 [-0.66 -0.62]<br>(-0.52,-0.52,-0.5) | -0.64 [-0.66 -0.62]<br>(-0.51,-0.52,-0.52) | -0.71 [-0.73 -0.70]<br>(-0.64,-0.62,-0.53) |
| IGP | -0.63 [-0.65 -0.61]<br>(-0.62,-0.53,-0.54) | -0.61 [-0.63 -0.59]<br>(-0.56,-0.49,-0.6) | -0.71 [-0.73 -0.69]<br>(-0.64,-0.55,-0.7) |
| IGP High-Res | -0.64 [-0.66 -0.62]<br>(-0.62,-0.53,-0.57) | -0.67 [-0.69 -0.65]<br>(-0.64,-0.53,-0.63) | -0.68 [-0.69 -0.66]<br>(-0.60,-0.52,-0.68) |

In addition to outer domain results, we also included the high-resolution inner domain (IGP) for analyses and incorporated the high-resolution IGP data (over the October to May dry season only). For the monsoon season, the analyses were done using the outer domain data only. For the dry season, we now use the high-resolution model output within the inner domain (IGP

region). The correlation between established HWII and IGP $PM_{2.5}$ concentration remains high (Table 2).

The strong correlation as found in the model simulation is further verified by correlations between HWII established from monthly MERRA2 and monthly $PM_{2.5}$ observations from U.S. Consulate General in Mumbai (https://in.usembassy.gov/embassy-consulates/mumbai/air-quality-data/; Table 3). Since the three predictive variables are not direct measurement in MERRA2 reanalysis product, it is ideal to validate MERRA2 using in situ observation. However, the observation is not easy to obtain because, (1) U10/T200 has the definition area over the ocean and (2) PBLH is not a directly measured variable in routine meteorological monitoring, especially back in 1990s in India. Nevertheless, we have compared these three variables in MERRA2 and ERA-interim (not shown) and found a close agreement between the two except MERRA2 tends to overestimate PBLH by 27%. In Mumbai, the correlation between observed $PM_{2.5}$ and MERRA2-derived HWII reaches as high as -0.85 (Table 3), which is comparable with the monthly correlation using model output only. The reason of showing the comparison between model and observation only in the monthly average is that US consulate observations have missing values for multiple days in a month, preventing us conducting the correlation calculation using daily values.

Table 3. Temporal correlations with 95% confidence interval between HWII and $PM_{2.5}$ in Chennai, south India and Mumbai monthly results for Historical Period. The values in the brackets indicate the lower and upper bound of confidence interval. The bottom row shows Mumbai results based on monthly values of MERRA2 meteorology and $PM_{2.5}$ observations from U.S. Consulate General in Mumbai. Values in the parenthesis are correlations between $PM_{2.5}$ and individual U10, T200, PBLH. Reprinted from Wu et al., (2019).

| | Correlations between HWII (U10, T200, PBLH) and $PM_{2.5}$ |
|---|---|
| Chennai (daily) | -0.38 [-0.41 -0.34]<br>(-0.20,-0.18,-0.61) |
| south India (daily) | -0.18 [-0.21 -0.14]<br>(-0.09,-0.14,-0.23) |
| Mumbai (monthly based on model output) | -0.86 [-0.88 -0.84]<br>(-0.81,-0.80,-0.65) |
| Mumbai (monthly based on observations) | -0.85 [-0.87 -0.83]<br>(-0.81,-0.79,-0.59) |

The connection between $PM_{2.5}$ and T200 is strong, but the physical mechanism is less straightforward. Cai et al. (2017) used the $\Delta T$ calculated from the temperature difference between 850 hPa and 250 hPa. But over India, we found weak correlations (less than 0.3) between $PM_{2.5}$ and $\Delta T$. Instead, the upper tropospheric temperature alone has a stronger correlation with $PM_{2.5}$. Studies have suggested that upper-level temperature vertical profile can regulate the pattern and strength of monsoon circulations (Li and Yanai, 1996; Boos and Kuang, 2010). Therefore, T200's influence is not independent from U10 described above.

Instead of affecting the wind pattern in a confined region (like U10), T200 tends to have a broader impact on the overall monsoon circulation for the entire South Asia. Previous studies have shown that one of the robust signatures of the South Asian monsoon onset and withdrawal corresponds to a positive and negative meridional tropospheric temperature (averaged between 200 hPa and 600 hPa) gradient (Goswami and Xavier, 2005; Xavier et al., 2007). The tropospheric temperature gradient has also been used in other studies focused on understanding the response of South Asian monsoon to aerosols. Upper-level temperature profile is also suggested to regulate the pattern and strength of monsoon circulations (Li and Yanai, 1996; Boos and Kuang, 2010). Previous studies (e.g. Ganguly et al. (2012) and Parthasarathy et al. (1990)) used the average temperature of multiple tropospheric layers (200-600 hPa) instead of a single layer. Our tests showed that either average of multiple layers or temperature at a single layer other than 200 hPa also work, but the highest correlation is obtained using T200. For example, the T300 and T600 have the correlation coefficient of -0.4 and -0.33 for Historical Period in Delhi (where T200/$PM_{2.5}$ correlation is -0.45).

The PBLH as a predictor of urban air quality has been extensively studied, and numerous studies have indicated that PBLH governs the convective lifting efficiency from surface into free troposphere, resulting in a vertical ventilation of $PM_{2.5}$ (e.g. Banta et al., 1998; Aumont et al., 2003; Petaja et al., 2016; Tang et al., 2016; Miao et al., 2017). Additionally, for the three representative cities in this paper, such a strong anti-correlation has also been documented in satellite-derived products (Sreekanth et al., 2017).

### 2.3.3 Predicting Future Changes in $PM_{2.5}$ due to Meteorology Only

In this section, we aim to quantitatively answer the following question: how does the future regional climate change affect $PM_{2.5}$ level?

The robust negative correlations between $PM_{2.5}$ and three meteorological variables imply a lower PM level in future when these meteorological variables increase as projected under RCP8.5 (Figure 4). Indeed, both U10 and T200 tend to increase in Decade 2050 (Table 4). U10 is projected to increase by 0.3 m/s and 0.5 m/s under RCP6.0 and RCP8.5, respectively. Similarly, T200 is projected to increases by 1.6 °C and 2.5 °C in the future. The PBLH in Delhi and Mumbai are expected to decrease slightly under RCP8.5, while PBLH in Kolkata and IGP are expected to increase (Table 4).

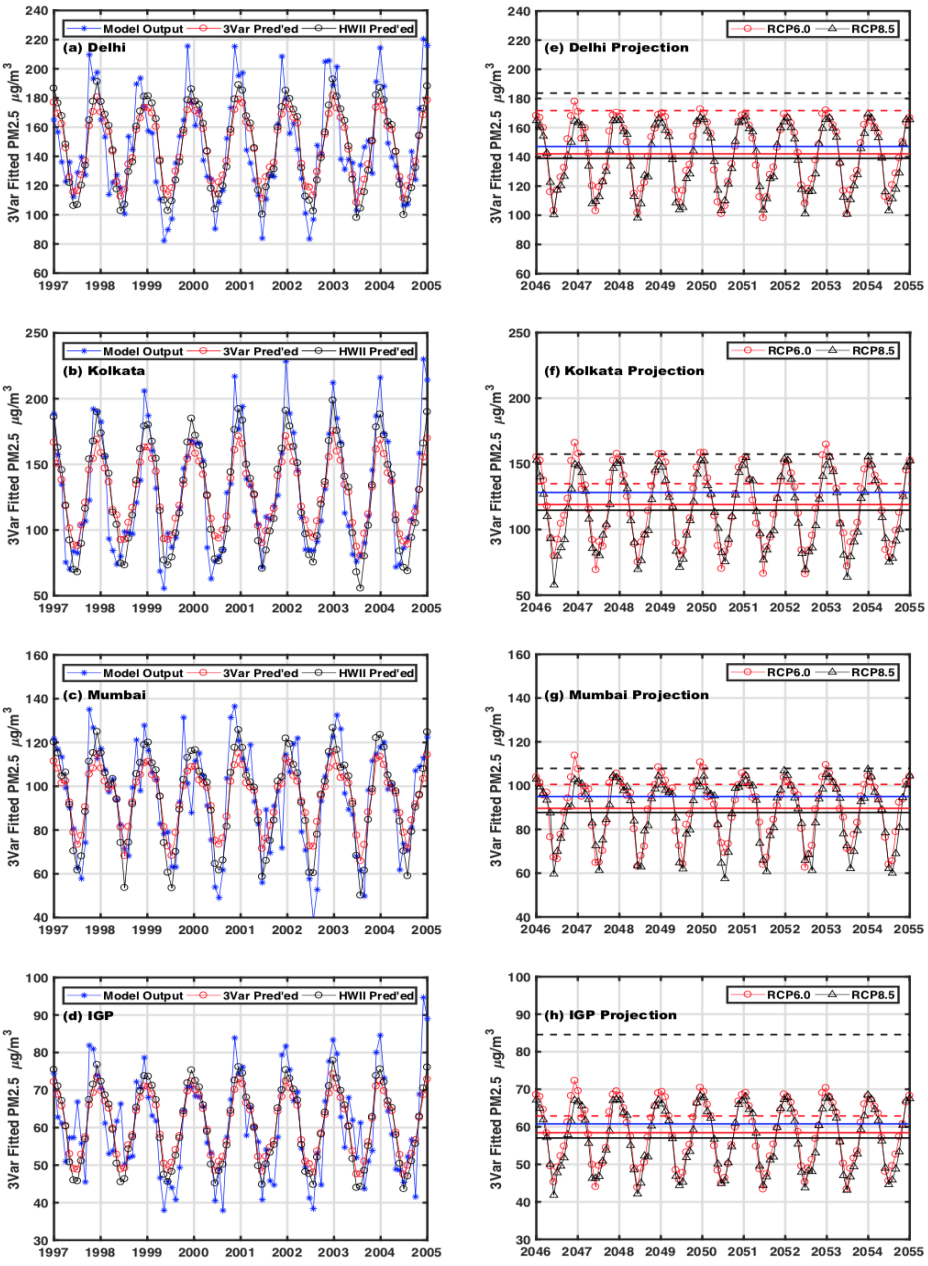


Figure 4. Historical Period monthly averaged $PM_{2.5}$ levels from direct model outputs (blue), statistical predictions using meteorological variables (red) and statistical predictions using HWII (black) over (a) Delhi, (b) Kolkata, (c) Mumbai and (d) IGP. (e)-(h) Predicted Decade 2050 $PM_{2.5}$ levels under two warming scenarios (red for RCP6.0 and black for RCP8.5) for four regions. Solid horizontal lines are for multi-year average of each prediction and dashed horizontal lines are from direct model outputs. Blue solid line is for the multi-year average of Historical Period). Reprinted from Wu et al., (2019).

Table 4. U10, T200, and PBLH in the Historical Period and the changes from Historical Period in the future under two RCP scenarios. Reprinted from Wu et al., (2019).

| | Historical Period | Change under RCP6.0 | Change under RCP8.5 |
|---|---|---|---|
| U10 (m/s) | 2.4 | +0.3 | +0.5 |
| T200 (°K) | 222.8 | +1.6 | +2.5 |
| PBLH (m) (Delhi, Kolkata, Mumbai, IGP) | 584, 473, 554, 555 | -32, +18, +18, +1 | -36, +17, -4, +11 |

Here, we construct a multivariate linear regression model to predict the $PM_{2.5}$ changes solely due to meteorological changes. We perform the linear regression over each city/region and for each meteorological variable. The statistical model is constructed as follows:

$$PM_{2.5}^{predicted} = (a_1\, U10 + a_2\, T200 + a_3\, PBLH + B)/3$$

Where the slopes $a_1$, $a_2$ and $a_3$ were derived from linear regressions applied to the Historical Period model output that is:

$a_1 = \ (PM_{2.5} - b_1 - error_1)/U10,$

$a_2 = \ (PM_{2.5} - b_2 - error_2)/T200,$

$a_3 = \ (PM_{2.5} - b_3 - error_3)/PBLH.$

Where $b_i$ are y-intercepts for each individual predictor and B is the summation of $b_i$ (i=1,2,3). The $error_i$ terms represent the differences between predicted y values using the linear regression and the actual y values. The coefficients in the linear regression model are listed in Table 5.

Table 5. Fitted Linear regression coefficients in the predictive model for $PM_{2.5}$ for three cities and IGP. Reprinted from Wu et al., (2019).

| | $a_1$, $a_2$, $a_3$ | $b_1$, $b_2$, $b_3$ |
|---|---|---|
| Delhi | -4.8,-9.7,-0.083 | 158.4, 2316.8, 195.8 |
| Kolkata | -6.2,-13.3,-0.20 | 143.0, 3087.4, 222.5 |
| Mumbai | -3.3,-8.0,-0.096 | 102.8, 1883.1, 148.4 |
| IGP | -1.9, -3.9, -0.036 | 85.2, 925.6, 80.6 |

The use of a regression-based model with three variables as separate predictors, in addition to HWII alone, is necessary here, even though both approaches can perform fairly well in predicting $PM_{2.5}$ based on Historical Period meteorology (Figure 4, left panel c for Mumbai). Note that HWII is a normalized quantity and it is hard to quantify its change from historical period to future (Figure 5), because when conducting the normalization, the temporal average during the respective periods are already removed. In Figure 5, the T200 is shown with obvious increases

under RCP8.5. U10 has slightly higher values in first half of the climatological year and the increases are more apparent in second half of the climatological year.

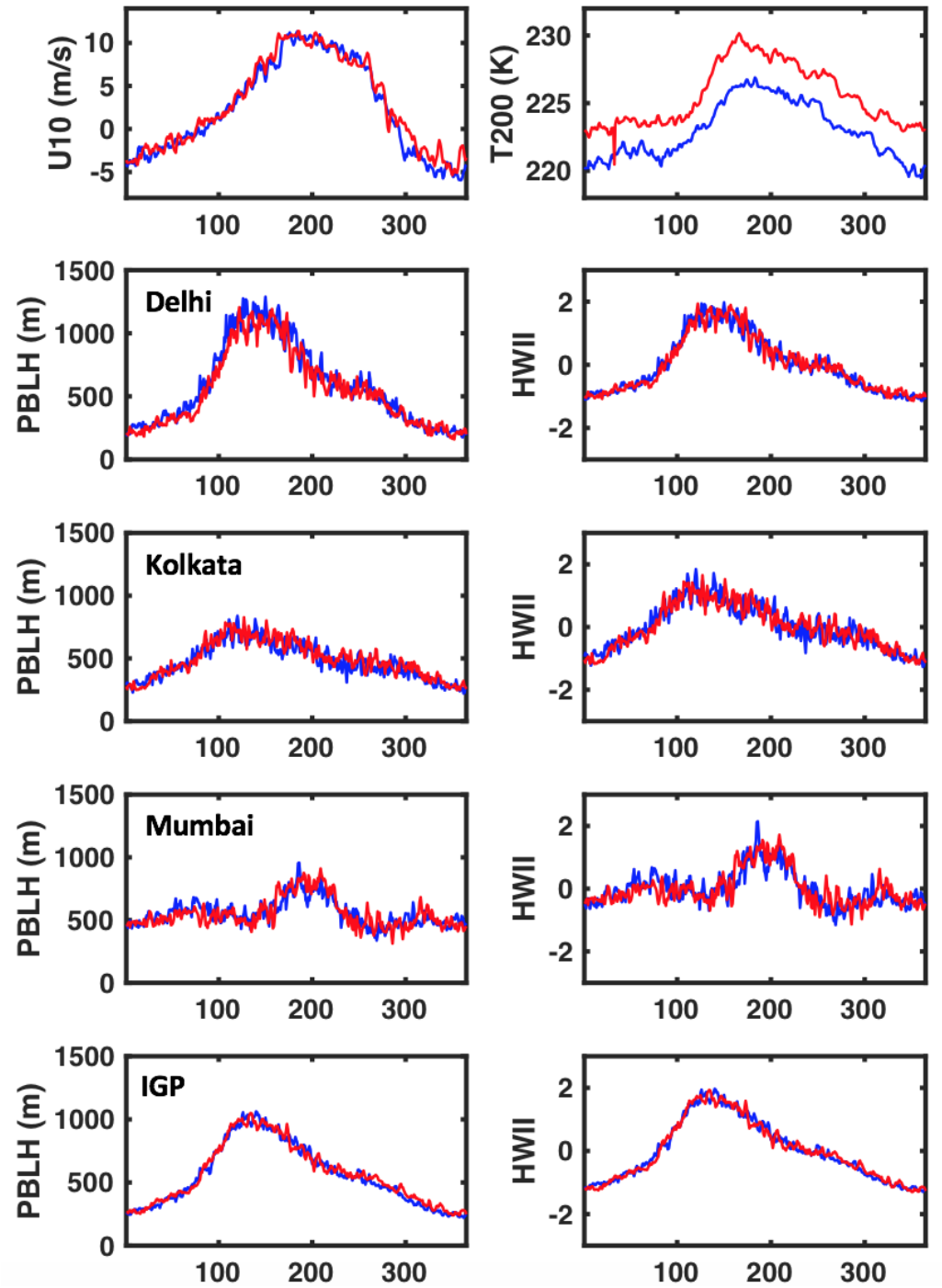


Figure 5. Climatology of three predictive meteorological variables and HWII over three cities and IGP region. Blue curves are for Historical Period and red curves are for RCP8.5. Horizontal axis is for the day in the year. U10 and T200 are the same for all regions (shown in first row). PBLH and HWII for each region are shown in left and right columns, respectively. Reprinted from Wu et al., (2019).

In Figure 4 (left), the statistical prediction of $PM_{2.5}$ levels (red) closely matches the direct model output (blue) for all three cities. The root-mean-square error (RMSE) of prediction is only ~ 13% (with the correlation coefficient as high as ~ 0.9) compared to the direct model outputs. The disagreement mainly comes from difficulty to predict the highest and lowest annual values, presumably due to the weaker seasonal cycles of PBLH compared to the U10 and T200 (see Figure 3). However, the prediction replicates the overall seasonal cycles and matches the annual mean simulated $PM_{2.5}$ levels reasonably well. Note that the primary focus of this study is not to capture monthly peak values of simulated $PM_{2.5}$ levels but to quantify the possibility of a "less polluted" future (in a multi-year average sense) if the changing meteorology is the only factor in play. The mean biases are also negligible (~ 0.1 $\mu g/m^3$, less than 0.1%). The consistency for Historical Period simulation indicates the statistical model of $PM_{2.5}$ can be reliably used in projecting the future changes (see in Figure 4 right panels).

One may question the validity of Figure 3 and HWII by questioning the impacts from seasonal cycles. Indeed, the seasonal cycle is boosting up the performance. However, we should not take seasonal cycle as the only factor in play here. To begin with, we assessed other variables like surface temperature, which should have stronger seasonal cycle compared to T200 because atmosphere gets heated from bottom-up. However, the performance of temperature ($r \sim -0.39$) at surface is not as good as T200 ($r \sim -0.53$). Nonetheless, when considering the seasonal cycles, we should not forget the signal-to-noise ratio for surface temperature profiles as the surface temperature peaks prior to the arrival of monsoon and T200 peaks during the monsoon season. In addition, when considering the DJF only for the IGP, the HWII went from -0.63 to -0.58, which is still high anti-correlations. Also, we should not forget that South Asia is probably the region that

is most heavily impacted by seasonal cycle itself due to its distinctive circulation pattern or monsoon cycle. Monsoon, in essence, comes with the seasonal cycle and removing such cycle from monsoon neglects the dominant climatological system here. U10 and T200 apparently have seasonal cycles and such seasonal cycle is tightly associated with the monsoon patterns. Therefore, the variations presented here for different meteorological variables could be reflections of monsoon intensities and monsoon itself, may ultimately regulate the circulation patterns in this region, leading to variations of PM levels. Under such scenario, both U10 and T200 shall only be considered as indicators for monsoon intensities. Moreover, what we strive to demonstrate here is that we could utilize the meteorology as a tool for future scenario projections. The validity of such projection is shown in Figure 4. In Figure 4, the overall tracking record for the History was fine especially, for 8-year averaged data. When discussing the resulting impact of seasonal cycle, we should keep in mind that the projection for the future is an average of all days in all years instead of a portion or a short period. In addition, we also evaluated the correlations of annual mean values to test its validity for the interannual variability. When using Delhi as an example, the correlation is 0.71, which shall be considered reasonable in this case for the linear fitting results. Therefore, the temporal fluctuation itself should have minimal effects on the final averaged results. Nonetheless, we do acknowledge that removing seasonal cycle here may resulting a lower correlation, however, we should keep this in mind: a region heavily regulated by monsoon cycles is inherently strongly impacted by this circulation pattern.

For all three cities and IGP, meteorology-driven $PM_{2.5}$ change is a decrease of 2%-7% in the future (even including Delhi where the local PBLH is expected to decrease, which should contribute to $PM_{2.5}$ increase by itself). Also, under the warmer RCP8.5 scenario, $PM_{2.5}$ level is

projected to be lower than RCP6.0 case (by 5%). This is expected as RCP8.5 has a larger increase in all three meteorological variables (Table 4).

The contributions toward a projected "cleaner future" are different from individual variables. T200 has the largest contribution (~49%) towards a projected lower $PM_{2.5}$ level, while PBLH has the smallest contribution (<10%). Since T200 increase in future (evident in Figure 5) is the largest contributor to the $PM_{2.5}$ reduction, it is interesting to test the sensitivity of our results to the inclusion of T200. First, the performance of HWII is not sensitive to inclusion of T200. When dropping the T200, the HWII and $PM_{2.5}$ correlation has small variations. For example, the IGP has the correlation coefficient of -0.63 (Table 2) for Historical period with the inclusion of T200 and this value slightly weakens to -0.62 when T200 is taken out of the equation and the Historical Period correlation changes from -0.71 to -0.72 in Kolkata. Though the variations are small, including T200 in the predictive model, however, can help improve the quantitative prediction of $PM_{2.5}$ level. For example, Mumbai in Figure 4 has a RMSE of 13.7 $\mu g/m^3$ when T200 is included and a RMSE of 14.5 $\mu g/m^3$ after removing T200. Second, even after removing T200 from the regression-based predictive model, the other two meteorological factors still predict a decrease in pollution level, but to a less extent. In Delhi, the predicted $PM_{2.5}$ under RCP8.5 is 142 $\mu g/m^3$ (a drop of 3% from Historical Period) without inclusion of T200, compared to a larger decrease of 6% (139 $\mu g/m^3$) when including T200 as a predictor. While the exact mechanism of the relationship between T200 and surface $PM_{2.5}$ is not clear at this time, it appears to change $PM_{2.5}$ predictions considerably.

## 2.4 Concluding Remarks

The HWII consisting of U10, T200, and PBLH, is developed to investigate the connections between meteorology and $PM_{2.5}$ levels in urban environments and IGP of India. We demonstrated that HWII is capable of depicting the day-to-day and season-to-season pollution level in major northern Indian cities. HWII, which combines the variability of three variables, generally have a better predictive skill than individual variables. The high correlation of $PM_{2.5}$ with HWII enables us to statistically predict $PM_{2.5}$ levels using a multivariate linear regression model, and also to apply such a regression model to estimate future changes in $PM_{2.5}$ due to meteorological shifts alone.

We find that under the two warming scenarios (RCP6.0 and RCP8.5) in Decade 2050, the three meteorological variables generally tend to increase leading to a more favorable environment for pollution dispersion. Our results over India are opposite to recent studies over other parts of the world, e.g., Cai et al. (2017) for Beijing and Chen et al., (2019) for eastern China. It implies a careful examination at a regional level is necessary before simply attributing past and future global warming as a source of degraded air quality.

Meanwhile, $PM_{2.5}$ levels are projected in our chemistry-climate model to rise in all three cities with RCP8.5 as the worst case. The overall increase in $PM_{2.5}$ can be attributed to the emissions locally in all three cities that are projected to rise in the future. Accordingly, we conclude that air quality in northern Indian metropolitan areas will greatly benefit from stricter emission regulations. Future works may examine the PM-meteorology correlations by replacing the T200 with tropospheric temperature gradient since T200 is very likely to increase due to global warming

trend (also apparent in Figure 5) and may therefore suffers the prediction biases accordingly. Also, future studies using global or regional chemistry transport models are needed to more rigorously separate the relative influence of emission and meteorology (and the individual mechanisms for the latter) by conducting further simulations such as those with fixed emission and oxidants levels and/or fixed meteorological conditions.

# CHAPTER III

# HEAT AND HIGH-PM HAZARDS[2]

## 3.1 Introduction

Air pollution is an ongoing issue globally. While there have been major efforts to cut air pollution emissions in developing nations, South Asia faces a unique challenge because of ongoing industrialization and urbanization processes. The next few decades will witness a continued increase in air pollution emissions (or only slightly decrease) in certain Shared Socioeconomic Pathways (SSP)/Representative Concentration Pathway (RCP) scenarios (Rao et al., 2017), which is opposite to the projected worldwide reduction including East Asia. Thus, local emissions continue to be the primary driver for air quality issues, while the influence of climate change cannot be ignored as well (Xu and Lamarque, 2018; Wu et al., 2019).

Despite limited case studies on the urban heat island effect worsening air quality (Wilby, 2008) and potential positive feedback to further enhance heat stress (Cao et al., 2016) in megacities, a decade-long continental-scale analysis of the co-occurrence of heatwave and air pollution extremes and their future changes is still missing. Recent examples are analyses of the heatwave and ozone episodes, such as Schnell and Prather (2017) using North American observations and Meehl et al., (2018) using global model output.

[2] Reprinted with permission from Xu, Y., Wu, X., Kumar, R., Barth, M., Diao, C., Gao, M., ... & Meehl, G. A. (2020). Substantial Increase in the Joint Occurrence and Human Exposure of Heatwave and High-PM Hazards Over South Asia in the Mid-21st Century. AGU Advances, 1(2), e2019AV000103.

Similarly, health risks associated with an elevated occurrence of heatwaves and high-PM weather are well studied, but often separately, highlighting a knowledge gap between understanding physical and chemical extremes. The compounding negative effect, when two types of conditions occur simultaneously, has only been studied at limited spatial scales (Stafoggia et al., 2008; Doherty et al., 2009; Jackson et al., 2010; Willers et al., 2016), including wildfire conditions induced by the 2010 Moscow heatwave. However, in the public health field, the synergistic impacts of two factors have raised great awareness on exacerbating health risks (Ren et al, 2006; Nawrot et al., 2007; De Sario et al., 2013; Qian et al., 2008; Katsouyanni et al., 2009; Li et al., 2011).

## 3.2 Methods

### 3.2.1 Main datasets used in this study.

This section briefly summarizes datasets used in this study, and detailed discussions are provided in the following sections.

(a) WRF-Chem model simulation (Kumar et al., 2018) of 8 years for present-day (1997-2004), and 9 years for the mid-21st century (2046-2054) under RCP8.5 and RCP6.0 emission scenarios.

(b) MERRA2 reanalysis products (Randles et al., 2017; Buchard et al., 2017) are used for surface $PM_{2.5}$, and ERA-Interim products (Dee et al., 2011) are used for deriving the wet-bulb temperature.

(c) Ground measurement of daily temperature and relative humidity are from select airports (collected by the India Meteorological Department but downloaded free of charge from Weather Underground database).

(d) Ground measurement of $PM_{2.5}$ in the late 1990s and early 2000s are compiled by Kumar et al., (2018), which are contributed by many observational studies (Pillai et al., 2002; Latha and Badarinath, 2003; Tiwari et al., 2009; Balakrishnaiah et al., 2011; Deshmukh et al., 2013; Tiwari et al., 2013).

(e) Populations for present-day and future decades are based on Jones and O'Neill (2016). The spatially explicit population dataset is from Jones and O'Neill (2016) with a spatial resolution of 1/8º by 1/8º. Before any data analysis related to population exposure, environmental quantities are regridded into the grid cells of population data using MATLAB function (interp2). SSP data is provided every ten years between 2000 (base year) and 2100 (projections). For example, data are available for 2010, 2020, 2030, etc. The Decade 2050 population projection (with 2 billion population in South Asia, Table 1) is based on Shared Socioeconomic Pathway (SSP) 5 scenario (fossil-fueled development for the economy), which is consistent with RCP8.5 emission pathway. Other SSP scenarios compatible with other RCPs are available in Jones and O'Neill (2016) but are not used in this study.

### 3.2.2 Model

This study uses multi-year simulations conducted using a Nested Regional Climate model coupled with Chemistry (NRCM-Chem) that is based on the Weather Research and Forecasting (WRF) model coupled with Chemistry (WRF-Chem, version 3.6.1) as described in Kumar et al. (2018). The model uses Model for Ozone and Related chemical Tracers, version 4 (MOZART-4) (Emmons et al., 2010) for gas-phase chemistry and simulates major aerosol species including sulfate, nitrate, ammonium, organic carbon, black carbon, dust and sea-salt using the Model of Simulating Aerosol Interactions and Chemistry (MOSAIC) (Zaveri et al., 2008).

The model domain covers the entire South Asia and surrounding oceanic regions (1.5º-44.7ºN and 52.6º-107.4ºE) using two domains with coarser horizontal grid spacing (60 km) for the outer domain; and finer horizontal grid spacing (12 km) for the smaller inner domain that encompasses the Indo-Gangetic Plain and the Himalayan region. All grid cells have the same area in this configuration. The simulation within the high-resolution inner domain only covers dry seasons (October to May) of each year. The model includes 51 vertical layers up to 10 hPa.

The MOSAIC model includes a sophisticated aerosol thermodynamics module to simulate the effects of changes in temperature and humidity on gas-particle partitioning and on the intraparticle solid-liquid phase equilibrium. Meteorology and chemistry are fully coupled in NRCM-Chem and feedback to each other at every time step. Aerosols affect the meteorology by interacting with both the radiation and clouds, and the corresponding changes in meteorology (temperature, pressure, winds, solar radiation, planetary boundary layer height, and precipitation) affect trace gases and aerosols via feedback to atmospheric chemical kinetics, dry and wet deposition, transport, biogenic emissions, and boundary layer mixing. Fire emissions and land use types were kept constant between the present-day and future simulations to limit the number of drivers contributing to future changes in air quality.

### 3.2.3 Simulations

The historical simulation ("Decade 2000") is from 1997 to 2004, and the future simulation ("Decade 2050") is from 2046 to 2054. The simulation is driven by large-scale meteorological and chemical boundary conditions from a global climate model that has been bias-corrected against past ERA-Interim (Bruyere et al., 2014). The evaluation of present-day climate and air quality also show reasonable agreement (see evaluations in supplement) and identified meteorological bias was

further corrected before our analysis (see supplementary materials for details). In a nutshell, we subtracted a geographically varying climatological bias as a function of time of the year ( historical simulation against ERA-Interim) from both the historical and future simulations.

Due to high resolution and complex chemical scheme, Kumar et al. (2018) only performed three sets of decade-long time-slice simulations, as opposed to a continuous century-long transient simulation such as in Xu and Lamarque (2018). Note that the decade-long time span of our simulation is still considerably longer than the most previous simulation with fine-resolution chemistry-climate models that usually lasted for weeks to months. The multi-year simulation with hourly output (averaged in this study to daily mean) of meteorology and chemistry is crucial to capture the behavior of extreme events (heatwave and high-PM) and estimate future changes in their frequency.

### 3.2.4 Scenarios

The Decade 2000 simulation is driven by large-scale meteorological boundary conditions generated by Community Earth System Model version 1 (CESM1; Hurrell et al., 2013), which is bias-corrected towards the reanalysis data (European Reanalysis, ERA-Interim) (Dee et al., 2011). The bias correction procedure is detailed in Bruyere et al., (2014). The chemical initial and boundary conditions are provided by a global atmospheric chemistry model (Community Atmospheric Model version 4 with Chemistry, CAM4-Chem) (Lamarque et al., 2012), driven by the same meteorological fields from CESM1. Thus, the meteorological boundary conditions used for WRF-Chem are consistent with the chemical boundary conditions in these runs.

The emission dataset was taken from the Atmospheric Chemistry and Climate Model Intercomparison Project (ACCMIP) (Lamarque et al., 2013). The simulated $PM_{2.5}$ surface

concentration for the "Decade 2000" was evaluated against seven observational sites in South Asia, and five out of seven sites have a climatologically monthly mean bias of less than 10%. Note that in this paper we use "PM" as a broader term to refer those health-adverse fine particles ($PM_{2.5}$, particulate matter with a diameter less than 2.5 um) while excluding the contribution of larger particles (>2.5 um) that could also be important for surface visibility.

The Decade 2050 simulation is driven by CESM1 output under two future emission scenarios: Representative Concentration Pathway (RCP) 8.5 ($CO_2$-equivalent of 630 ppm in 2050) and RCP6.0 (505 ppm at 2050). The two scenarios considered are the two higher ones in the RCP database, and the global $CO_2$ emission is tracking RCP8.5 closely (as of 2018, Figure 6), justifying the focus on the two higher emission scenarios as opposed to the two lower ones. The $PM_{2.5}$ emission in South Asia stays largely the same under RCP6.0, compared to the Historical Period. But for RCP8.5, a 77% increase in total emission from the Historical Period level is projected. All four RCP scenarios could not be run because of limited computational and storage resources.

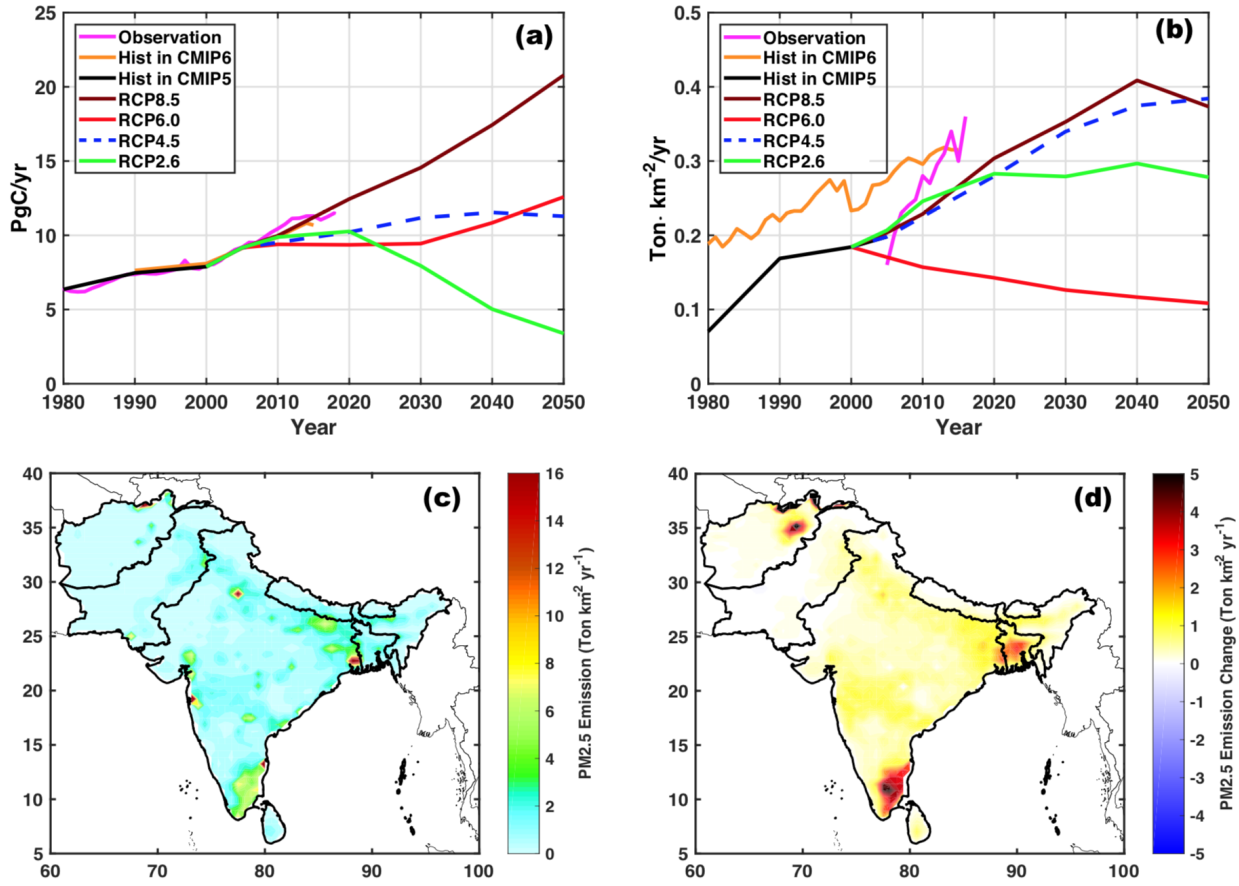


Figure 6. (a) Global emission of Carbon (due to fossil fuel and land use) and (b) Indian emission of $SO_2$ under different projections. RCP4.5 curves are dashed to distinguish from the RCP8.5 curve in (b). The "History" is according to CMIP5 and CMIP6 protocol. Future emissions (after 2005) are from four RCP scenarios (van Vuuren et al., 2011). The $CO_2$ "observation" is from Le Quere et al., (2018). The Indian $SO_2$ "observation" is based on satellite estimates in Li et al., (2017). (c) Emission of $PM_{2.5}$ (ton km-2 yr-1) over South Asia in Decade 2000 and (d) its change in Decade 2050 under RCP8.5. Reprinted from Xu et al., (2020).

We note that the current global emission of $CO_2$ is tracking RCP8.5 closely (as of 2018, see Figure 6). The satellite-based $SO_2$ emission estimate (Li et al., 2017) is even higher than the RCP8.5 projection and more in line with the recently released CMIP6 emission dataset (SSP).

These provide a strong justification for focusing on the higher emission scenario such as RCP8.5 as opposed to the lower ones.

### 3.2.5 Calculation of the wet-bulb temperature (Tw)

Many previous heat extremes analyses only considered temperature alone (e.g., Meehl and Tebaldi, 2004; Xu et al., 2015), but more recent studies have accounted for humidity impact on the heat stress (e.g., Kovats and Hajat, 2008). A recent assessment of heat extremes related mortality suggested that a combination of temperature and humidity is a better metric to quantify health risks (Mora et al., 2017). That is, under high humidity conditions, human exposure to a lower temperature can induce the same level of risk compared to higher temperature exposure but under lower humidity conditions. Here, we account for both temperature and humidity variations by computing the wet-bulb temperature (Tw; Sherwood and Huber, 2010). Tw should not be confused with the wet bulb globe temperature (WBGT) that additionally accounts for the effect of wind speed and solar radiation (or the simplified form by assuming moderate radiation and light wind speed as in Willett and Sherwood, 2012; Knutson and Ploshay, 2016).

In practice, wet bulb temperature (Tw) can be measured by wet bulb thermometers as the environment saturation ratio of water vapor is reached. Here Tw is computed following Stull (2011) from the daily average of T (temperature, "dry-bulb"; unit: ºC) and RH (relative humidity; unitless, ranging from 0 to 100%).

$$T_w = T \cdot \operatorname{atan}\left[0.151977(100 \cdot \mathrm{RH} + 8.313659)^{\frac{1}{2}}\right] + \operatorname{atan}(T + 100 \cdot RH) - \operatorname{atan}(100 \cdot RH - 1.676331) + 0.00391838(100 \cdot RH)^{\frac{3}{2}} \operatorname{atan}(0.023101 \cdot 100 \cdot RH) - 4.686035$$

Depending on the data availability, RH is calculated in the following two ways.

(1) From the WRF-Chem model output, RH is calculated from T (temperature; unit: K), p (air pressure; unit: Pa) and q (specific humidity; unitless).

$$e_s = e_0 \exp\left(\frac{L_v}{R_w}\left(\frac{1}{T_0} - \frac{1}{T}\right)\right)$$

$$\omega_s = \frac{R_a}{R_w}\frac{e_s}{p - e_s}$$

$$\omega = \frac{q}{1 - q}$$

$$RH = \frac{\omega}{\omega_s}100\%$$

(2) From the ERA-Interim dataset, RH is calculated from T, p, and $T_{dew}$ (dew point temperature; unit: K).

$$e_s = e_0 \exp\left(\frac{L_v}{R_w}\left(\frac{1}{T_0} - \frac{1}{T}\right)\right)$$

$$e_{dew} = e_0 \exp\left(\frac{L_v}{R_w}\left(\frac{1}{T_0} - \frac{1}{T_{dew}}\right)\right)$$

$$RH = \frac{e_{dew}}{e_s}\frac{p - e_s}{p - e_{dew}}100\%$$

In the equations above, $e_0$ (611 Pa) is the reference water vapor pressure, and $e_s$ and $e_{dew}$ are the water vapor pressure at saturation and at dew point temperature, respectively. w and $w_s$ are water vapor mixing ratio (water vapor vs. dry air, unitless) at any given temperature or at saturation. $T_0$ (273 K) is the reference temperature. $L_v$ ($2.5*10^6$ J/kg) is the latent heat of water vaporization (from liquid to gas). $R_a$ (287 J/kg/K) is the specific gas constant for dry air. $R_w$ (461.5 J/kg/K) is the specific gas constant for water vapor. Calculation of daily Tw has little differences from the mean-taking method, i.e., from the average of hourly Tw or from mean daily T and RH (Figure 7).

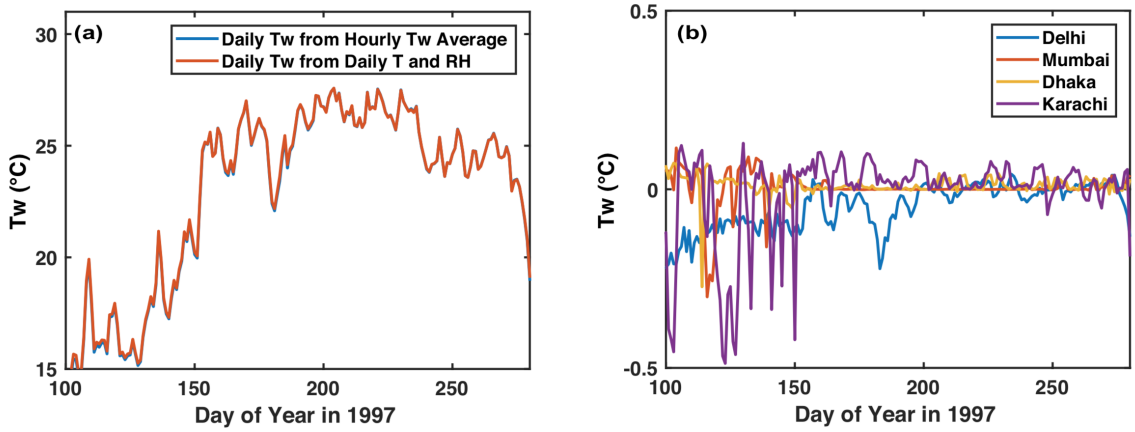


Figure 7. (a) Daily Tw in warm season (day 100 to 280) of 1997 calculated from two methods: (red) Daily Tw calculated from daily mean temperature and RH and (blue) Daily Tw calculated from hourly Tw for Delhi. (b) Tw differences induced by two calculation methods for four focused cities). Reprinted from Xu et al., (2020).

### 3.2.6 Threshold for defining heatwave and high-PM extremes

Here we adopt daily average Tw at 25ºC as the threshold for heat extremes in this analysis. This is close to the "deadly" threshold (red line in Figure 8) as reported in Mora et al., 2017 who established this threshold based on hundreds of heat-related deadly events during 1980 and 2014 and recorded daily temperature and humidity (but treated separately, not jointly using Tw).

In the context of weather extremes, the question often arises as to "how extreme" certain thresholds should be. Previous studies have used a higher threshold of 35ºC to identify deadly or even fatal extreme heat (Kang and Eltahir, 2018), which is the physical limit to heat removal from the body. Note that Lelieveld et al., (2014) used daily max temperature of 35ºC as the threshold, which is close to 25ºC Tw at 40% RH as in the two India heatwave events we identified (Figure 8), but not the wet-bulb temperature.

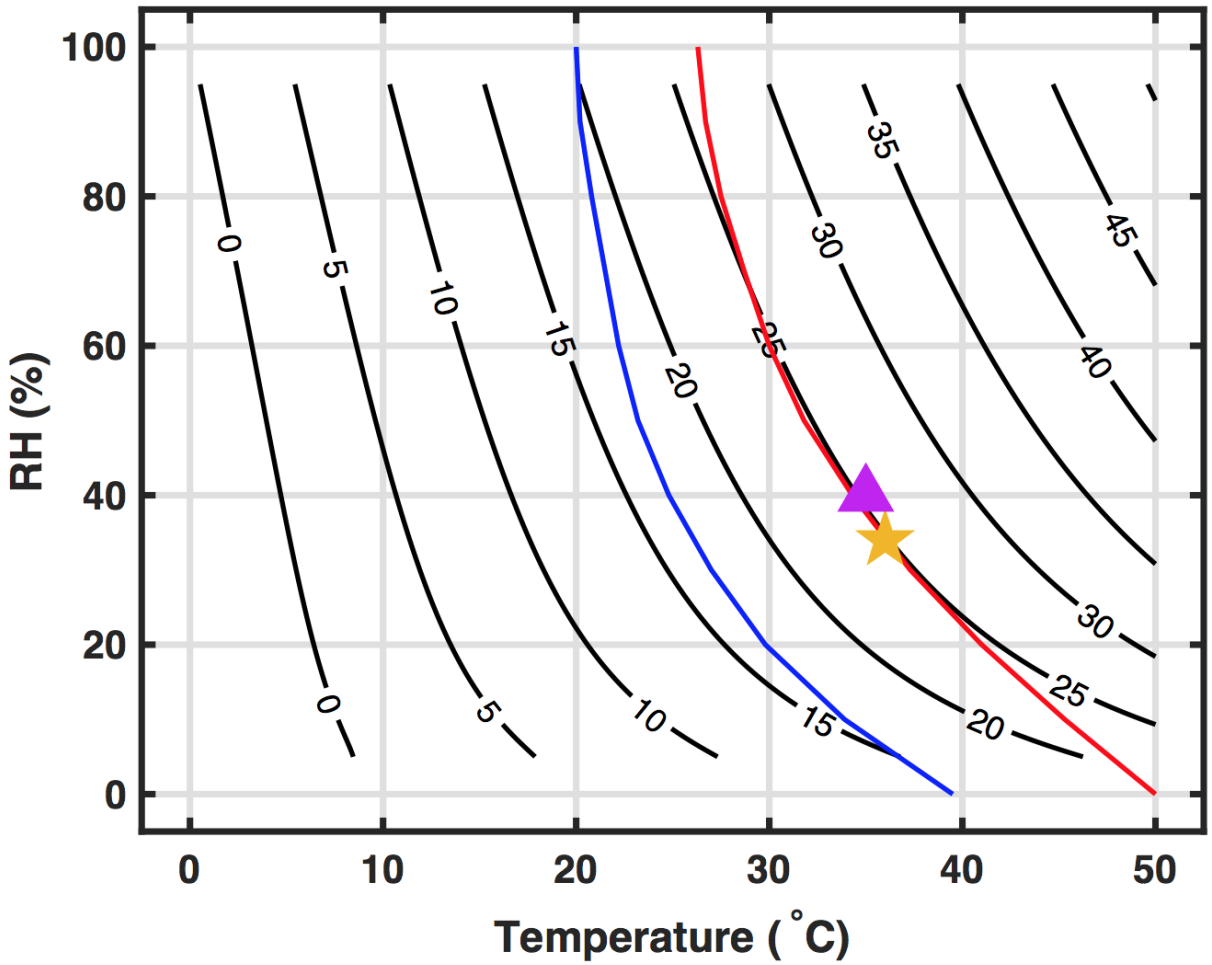


Figure 8. Tw as a function of temperature and relative humidity. The 25ºC Tw is close to the "deadly" threshold established in Mora et al., (2017) (red line, with 95% lethal events already occurring at this level). The blue line (Tw between 15ºC to 20ºC) is a weaker definition of heat extremes when the lethal events start to occur. Yellow star indicates a multi-week heat extremes event in Ahmedabad (in Western India) during May 2010 (T=36ºC, RH=34% from ERA-Interim monthly value; Azhar et al., 2014). The purple triangle indicates a heat extremes event in Allahabad (near central Indo-Gangetic Plain) during May, 2015 (T=35ºC, RH=40% calculated from ERA-Interim monthly value; Burke, 2015). Reprinted from Xu et al., (2020).

In our case, using the 25ºC threshold allows more samples to enter the analysis and provides a more robust statistical analysis. However, the results with a higher threshold (e.g. Tw

of 28ºC, Table 6) would be qualitatively similar, the processes would be the same, and the basic results would not change with the caveat that the higher threshold would, of course, represent more lethal conditions. We also conducted a sensitivity test in Karachi using the threshold of daily maximum Tw>35ºC (Table 6) following Kang and Eltahir (2018), which suggests that RCP8.5 could see a 720% increase in heat extremes frequency.

Table 6. South Asia frequency (day/year) and duration (day) of heat extremes by applying different thresholds. All results are based on the original Tw (or T) without bias correction. The threshold of T (daily mean temperature) and Tw_max (daily maximum wet-bulb temperature) is deliberately selected so that the Decade 2000 frequency is similar to the frequency when using Tw of 25ºC as the threshold (48 days). Reprinted from Xu et al., (2020).

| | Frequency (day/year) | | | Duration (day) | | |
|---|---|---|---|---|---|---|
| Threshold definition | 2000 | 2050 RCP6.0 | 2050 RCP8.5 | 2000 | 2050 RCP6.0 | 2050 RCP8.5 |
| Tw > 25ºC | 48 | 66 | 76 | 6 | 9 | 11 |
| Tw > 25ºC but individual extreme event to be >2 days | 38 | 54 | 65 | 7 | 12 | 18 |
| Tw > 18ºC | 168 | 183 | 191 | 75 | 119 | 141 |
| Tw > 28ºC | 2 | 5 | 10 | 1 | 1 | 2 |
| T > 31ºC | 49 | 56 | 63 | 8 | 9 | 10 |
| Tw_max > 26ºC | 48 | 60 | 77 | 6 | 7 | 9 |
| Tw_max > 35ºC (as in Kang and Eltahir, 2018), for Karachi only | 0.5 | 0.2 | 3.6 | 0.3 | 0.1 | 1.3 |

As acknowledged in Mora et al. (2017), previous assessments on deadly heat events have focused on developed nations in the Northern Hemisphere mid-latitudes (Europe and North

America). The applicability of the same threshold to tropical and developing nations remain to be tested using large-scale public health data. Here, we justify the robustness of the 25ºC Tw threshold with limited case studies over South Asia. The yellow star and purple triangle in Figure 8, both close to Tw of 25ºC, correspond to two heat extreme events, which reportedly killed more than 1300 people (see Figure 8 caption for details).

It has become clear to the climate and health research community that the humidity effect needs to be accounted for in heat extreme health impact studies (Sherwood, 2018). To put Tw in the perspective of two other temperature/humidity related heat metrics, Tw during the 2010 Ahmedabad event is 24.8ºC (T=36ºC, RH=34%), and this is equivalent to 37.2ºC in "heat index" (using the formula of http://www.wpc.ncep.noaa.gov/html/heatindex.shtml; Matthews et al., 2017, also called "apparent temperature"; Russo et al., 2017; Herring et al., 2016) and 41.6ºC (in "humidex" using the formula of https://memory.psych.mun.ca/tech/js/humidex) (Barnett et al., 2010). Such a high value of heat index is classified as "extreme caution" (https://www.weather.gov/safety/heat-index) by the National Oceanic and Atmospheric Administration (NOAA), and such a high value of humidex is classified as "great discomfort" by the Canadian meteorologists (https://en.wikipedia.org/wiki/Humidex). Other more complex indices that use factors beyond the relative humidity may be more relevant to health impacts, such as WBGT (Liang et al. 2011) or UTCI (Universal Thermal Climate Index; Jendritzky et al., 2012). Sustained exposure to high $PM_{2.5}$ environment (such as 100 $\mu g/m^3$) is conducive to cardiopulmonary mortality and lung cancer (Turner et al, 2011). The threshold of defining high-PM extremes days is here set to 60 $\mu g/m^3$ of daily mean surface concentration of $PM_{2.5}$ following India air quality standard (CPCB, 2009). The 60 $\mu g/m^3$ value is larger than the "unhealthy" level of the 25 $\mu g/m^3$ recommended by the World Health Organization (WHO, 2005), the 55.5 $\mu g/m^3$

level of "unhealthy" recommended by the Environmental Protection Agency of the US (EPA, 2012), but it is smaller than the 75 μg/m$^3$ definition of "severe air pollution" recommended in China (Jin et al., 2016). Sensitivity sensitivities (Figure 9) show the results are not particularly sensitive to the selection of threshold other than the expected absolute value change.

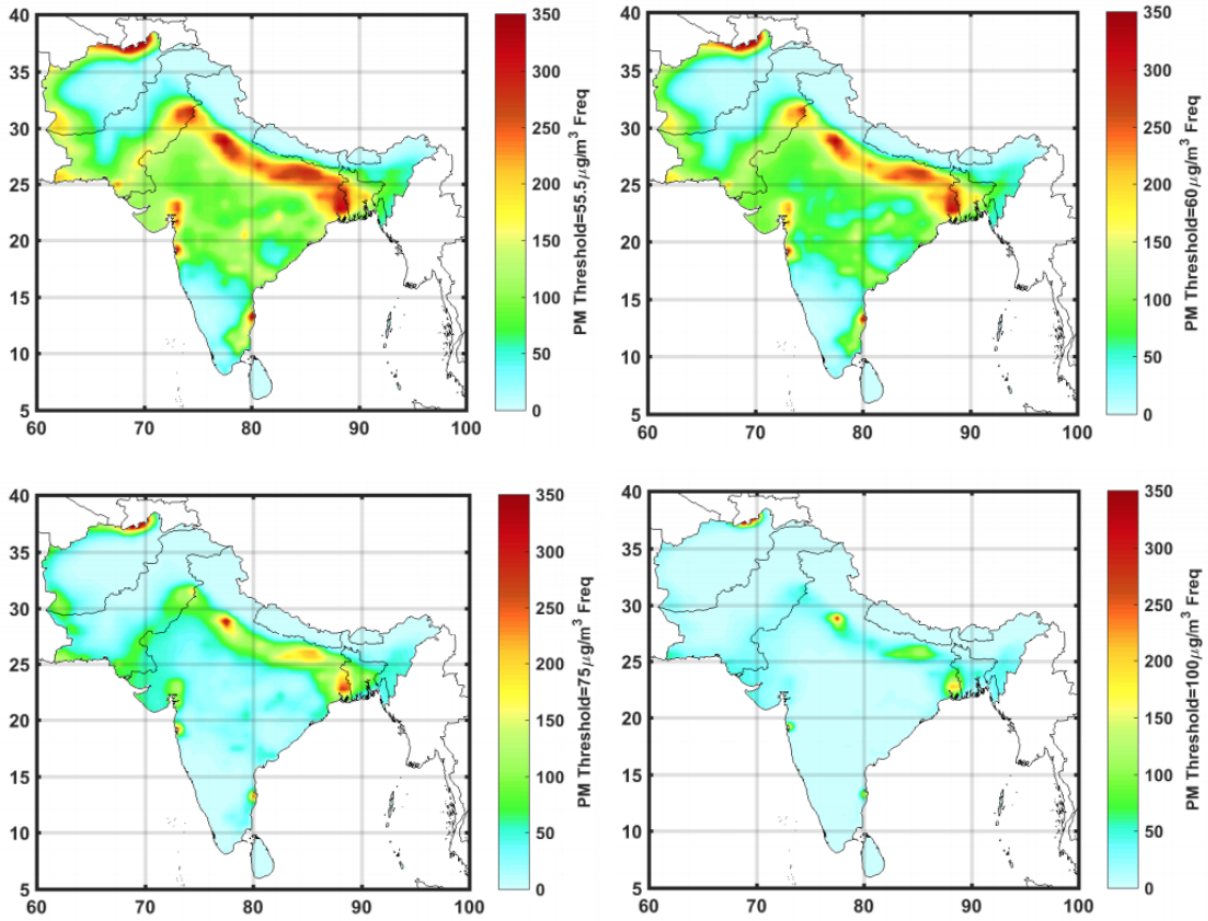


Figure 9. Spatial distribution of Haze extremes frequency (day/year) during the Decade 2000. Note that the Haze extremes frequency varies with different thresholds (55.5, 60, 75 and 100 μg/m$^3$). Reprinted from Xu et al., (2020).

### 3.2.7 Statistical metrics of occurrence of extreme events (heatwave and high-PM)

To quantify the occurrence of the heatwave and high-PM extremes, the daily value of Tw and surface concentration of $PM_{2.5}$ is calculated for all grid points of the model output. Having established a certain threshold (section 4), days with values higher than the threshold are classified as extreme days. The *frequency* (days/year) and the mean *duration* (days) of extreme events are calculated for each year, and then the multi-year average for the Decade 2000 and the Decade 2050 under RCP6.0/8.5 is taken to remove the interannual variability of regional climate. Using a stronger definition of extreme events that requires the duration of any individual events to be at least 2 days (e.g., Xu et al., 2015 and references within), the frequency numbers in Table 7 would be lower (see Table 6), but not significantly, due to the low weather variability and long-lasting nature of tropical heat extremes in this region.

Table 7. (a) Tw (ºC), frequency of heat extremes (day/year), duration (day), and relative intensity. The numbers are for the Decade 2000 and Decade 2050 under two scenarios. The numbers in parentheses of South Asia row are based on original model output and the numbers in brackets are from ERA-Interim. (b) same as (a), but for haze events. Reprinted from Xu et al., (2020).

| (a) heat | Tw (°C) | | | Frequency (day/year) | | | Duration (day) | | | Relative Intensity (°C above 25) | | |
|---|---|---|---|---|---|---|---|---|---|---|---|---|
| | 2000 | 2050 RCP 6.0 | 2050 RCP 8.5 | 2000 | 2050 RCP 6.0 | 2050 RCP 8.5 | 2000 | 2050 RCP 6.0 | 2050 RCP 8.5 | 2000 | 2050 RCP 6.0 | 2050 RCP 8.5 |
| Afghanistan | 6.4 | 7.3 | 7.4 | 0 | 0 | 0 | 0 | 0 | 0 | 0.0 | 0.1 | 0.1 |
| Bangladesh | 22.2 | 23.6 | 24.2 | 156 | 191 | 211 | 14 | 18 | 21 | 1.3 | 1.8 | 2.2 |
| Bhutan | 8.5 | 9.9 | 10.6 | 0 | 1 | 2 | 0 | 0 | 0 | 0.0 | 0.1 | 0.0 |
| India | 18.7 | 19.8 | 20.3 | 53 | 81 | 97 | 5 | 8 | 9 | 0.6 | 1.0 | 1.1 |
| Nepal | 9.8 | 11.0 | 11.6 | 9 | 16 | 21 | 1 | 1 | 2 | 0.1 | 0.2 | 0.2 |
| Pakistan | 13.2 | 14.1 | 14.3 | 44 | 53 | 59 | 6 | 6 | 7 | 0.8 | 1.2 | 1.7 |
| Sri Lanka | 23.9 | 24.7 | 25.2 | 60 | 153 | 212 | 4 | 7 | 13 | 0.3 | 0.6 | 0.8 |
| South Asia | 15.9 (15.0) [16.7] | 16.9 | 17.3 | 45 (48) [47] | 67 | 78 | 5 (6) [5] | 6 | 8 | 0.6 (0.7) [0.6] | 0.9 | 1.0 |

Table 7 continued.

| (b) haze | $PM_{2.5}$ (μg/$m^3$) | | | Frequency (day/year) | | | Duration (day) | | | Relative Intensity (μg/$m^3$ above 60) | | |
|---|---|---|---|---|---|---|---|---|---|---|---|---|
| | 2000 | 2050 RCP 6.0 | 2050 RCP 8.5 | 2000 | 2000 | 2050 RCP 6.0 | 2050 RCP 8.5 | 2000 | 2000 | 2050 RCP 6.0 | 2050 RCP 8.5 | 2000 |
| Afghanistan | 39.3 | 31.2 | 46.5 | 59 | 39.3 | 31.2 | 46.5 | 59 | 39.3 | 31.2 | 46.5 | 59 |
| Bangladesh | 54.9 | 64.7 | 76.0 | 123 | 54.9 | 64.7 | 76.0 | 123 | 54.9 | 64.7 | 76.0 | 123 |
| Bhutan | 19.3 | 15.3 | 21.8 | 4 | 19.3 | 15.3 | 21.8 | 4 | 19.3 | 15.3 | 21.8 | 4 |
| India | 45.8 | 43.6 | 60.3 | 83 | 45.8 | 43.6 | 60.3 | 83 | 45.8 | 43.6 | 60.3 | 83 |
| Nepal | 24.7 | 23.2 | 30.1 | 11 | 24.7 | 23.2 | 30.1 | 11 | 24.7 | 23.2 | 30.1 | 11 |
| Pakistan | 42.2 | 46.4 | 55.5 | 69 | 42.2 | 46.4 | 55.5 | 69 | 42.2 | 46.4 | 55.5 | 69 |
| Sri Lanka | 25.1 | 24.6 | 27.0 | 1 | 25.1 | 24.6 | 27.0 | 1 | 25.1 | 24.6 | 27.0 | 1 |
| South Asia | 43.5 | 41.9 | 56.4 | 75 | 43.5 | 41.9 | 56.4 | 75 | 43.5 | 41.9 | 56.4 | 75 |

In addition to quantities of the number of days of extremes, the severity of extremes is also important. The relative intensity of extreme events is reported here in an anomalous sense, as the difference between quantities averaged within extreme days and the selected threshold. A large relative intensity (ºC or $\mu g/m^3$) indicates a severe departure from the threshold and has been suggested as a predictor for heat stress-related mortality (Rocklov et al., 2012).

We define a fourth metric here, accumulated relative intensity, as the product of frequency (days/year) and relative intensity (ºC or $\mu g/m^3$). The concept of accumulated relative intensity for heat stress is similar to the cooling degree days ((temperature - 22ºC) * number of days with the temperature higher than 22ºC) that has been widely used in assessing the demand for air conditioning (Miller et al., 2008; Shi et al., 2016).

## 3.3 Results

### 3.3.1 Humidity-amplified heat stress

With the daily average wet-bulb temperature (Tw, as in Stull, 2011) of 25ºC as the threshold, heat extremes frequency is as high as 100-200 days/year over the coastal regions and the Indo-Gangetic Plains during the Decade 2000 (Figure 10), with a prolonged duration of more than 15 days particularly over the foothills of the Himalayas. The high values of Tw in the southern coastal regions are due to high humidity and in the Indo-Gangetic Plain due to high temperature (Figure 11). Under the RCP8.5 scenario, the future occurrence of heat extremes is projected to increase from 45 days/year (averaged over the seven countries within South Asia) to 78 days (a 73% increase; Table 7 and Figure 12) and with a mean duration of heat extremes events of over 14 days in cities such as Delhi (Table 8).

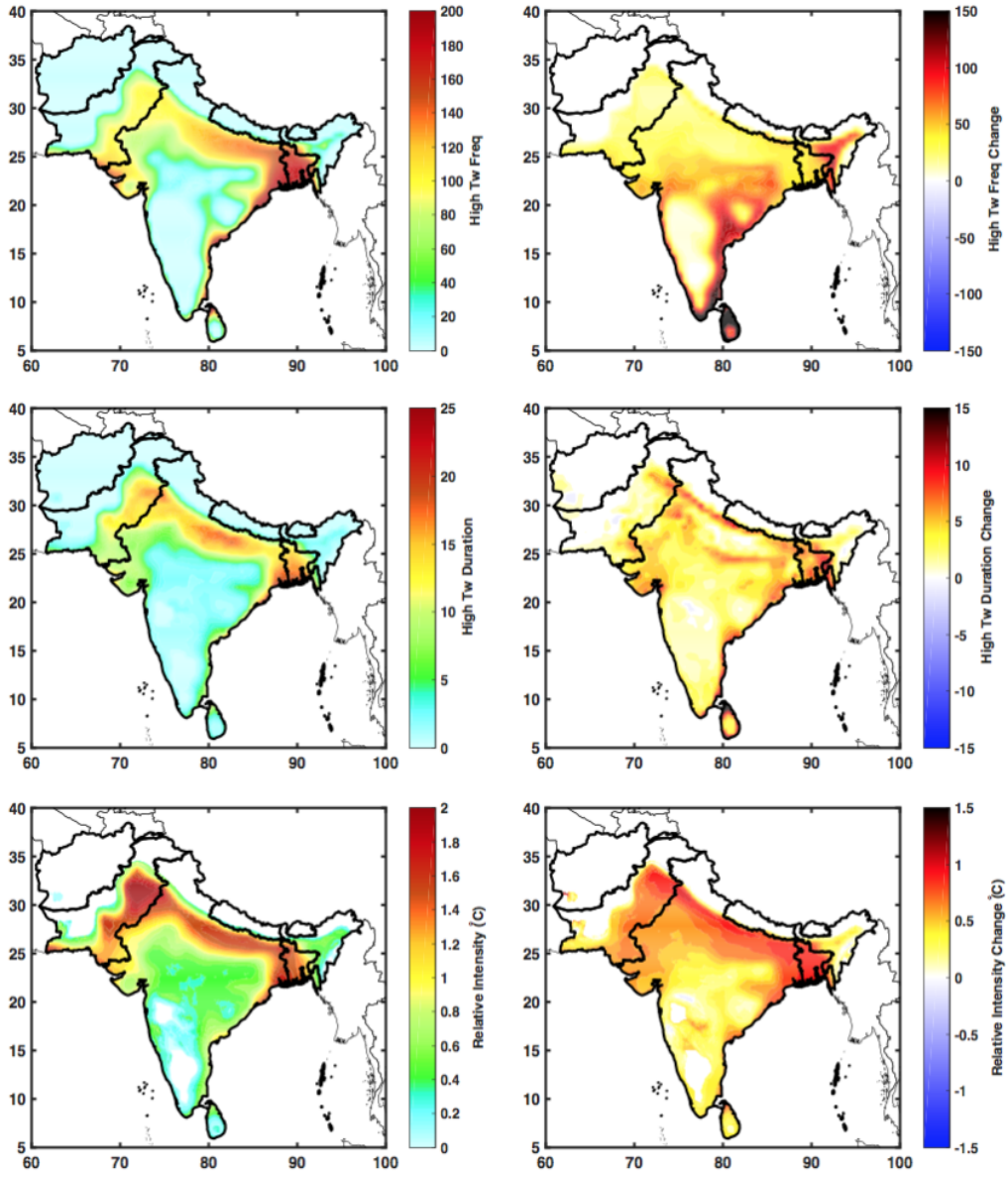


Figure 10. (Top row) Frequency of heat extremes (days/year) at Decade 2000 and its change at Decade 2050 under RCP8.5. (Middle row) Duration (days). (Bottom row) Relative intensity (ºC). The white areas are regions where no heat extremes occur in the Decade 2000. Reprinted from Xu et al., (2020).

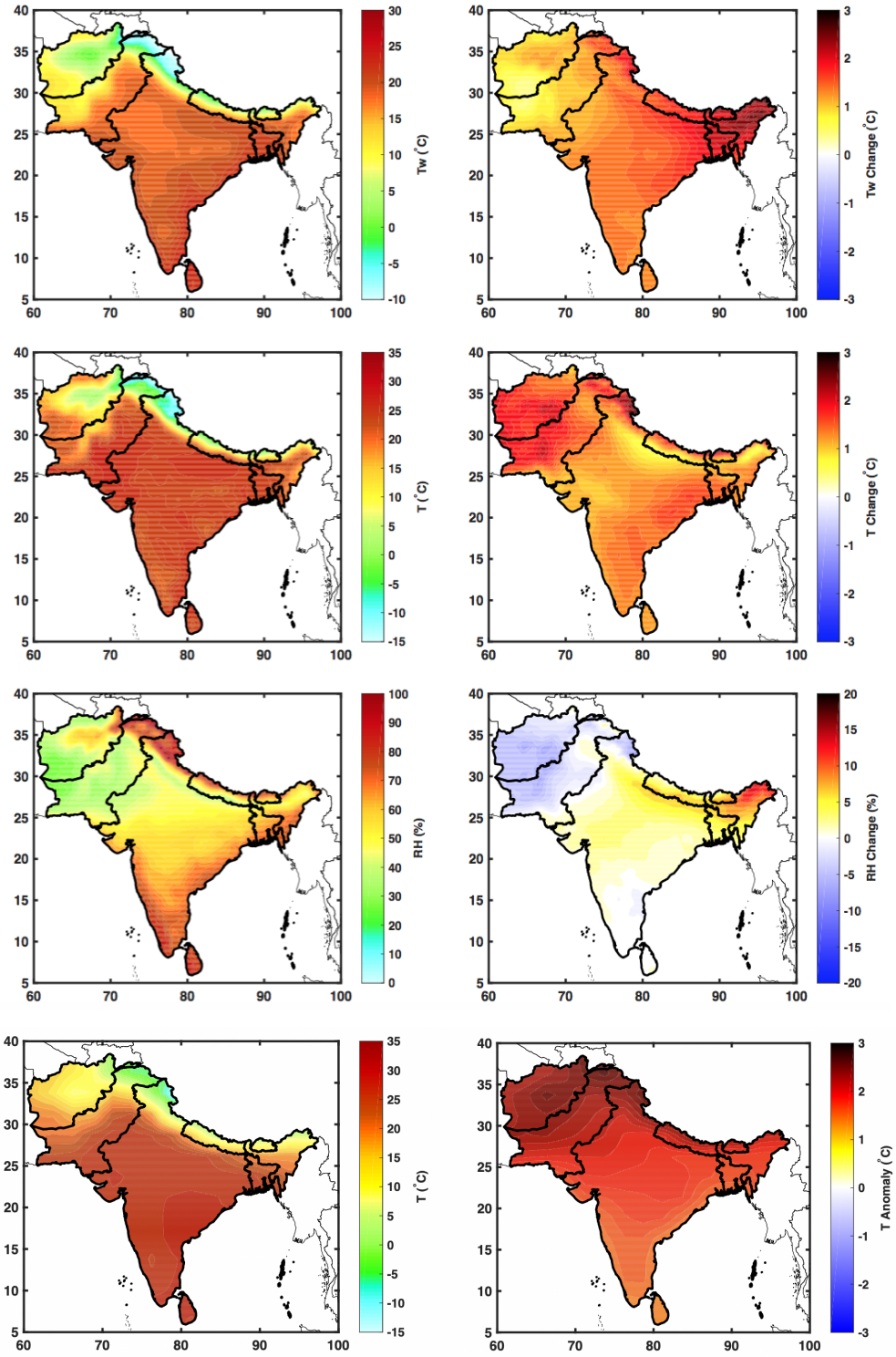


Figure 11. (First row) Bias-corrected Tw in Decade 2000 and the change in Decade 2050 under RCP8.5. (Second row) T. (Third row) RH. (Fourth row) T as in the second row but from 19 CMIP5 models (Source: KNMI Climate Explorer). Reprinted from Xu et al., (2020).

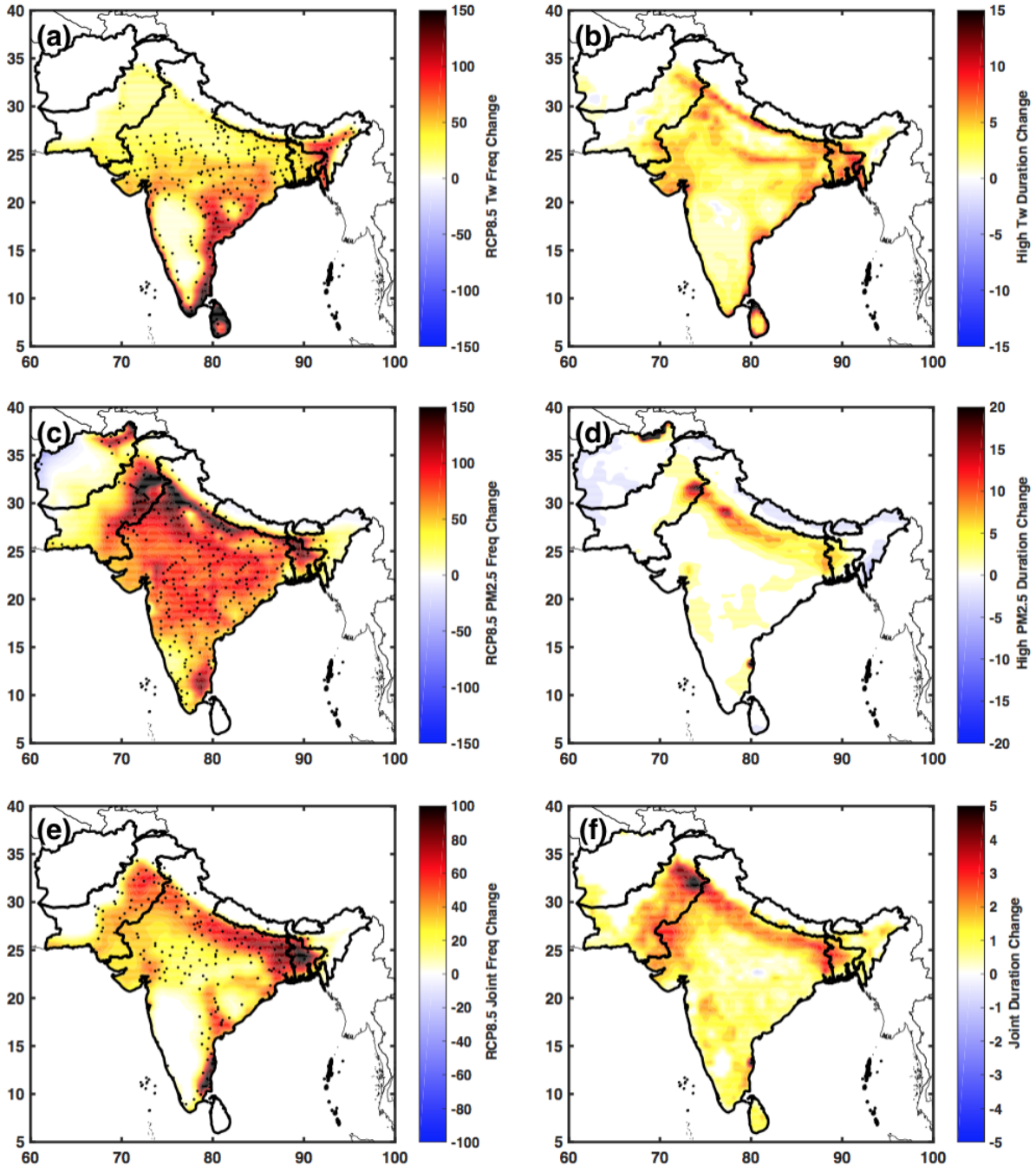


Figure 12. Future change (Decade 2050 minus Decade 2000) under RCP8.5 in frequency (days/year) of (a) heat extremes, (c) high-PM extremes and (e) HHH. Stippling indicates regions with statistically significant positive change at the 1% confidence level using the Student's t-test. (b), (d) and (f): Same as the left column, but for the mean duration (day). Reprinted from Xu et al., (2020).

Table 8. Similar to Table 7, but for individual cities. The city scale is defined as 1 model grid box of 60 km * 60 km that is closest to the city center. In the case of using high-resolution 12 km model output, the domain for one city covers 25 grid boxes. Reprinted from Xu et al., (2020).

| (a) heat | Tw (°C) | | | Frequency (day/year) | | | Duration (day) | | | Relative Intensity (°C above 25ºC) | | |
|---|---|---|---|---|---|---|---|---|---|---|---|---|
| | 2000 | 2050 RCP 6.0 | 2050 RCP8.5 | 2000 | 2050 RCP 6.0 | 2050 RCP 8.5 | 2000 | 2050 RCP 6.0 | 2050 RCP 8.5 | 2000 | 2050 RCP 6.0 | 2050 RCP8.5 |
| Delhi, India | 17.5 | 18.8 | 19.1 | 109 | 127 | 134 | 14 | 16 | 18 | 1.6 | 2.2 | 2.5 |
| Mumbai, India | 21.7 | 22.3 | 22.6 | 13 | 69 | 88 | 2 | 5 | 5 | 0.3 | 0.6 | 0.7 |
| Dhaka, Bangladesh | 21.3 | 22.9 | 24.7 | 183 | 215 | 231 | 16 | 23 | 20 | 1.4 | 2.0 | 2.4 |
| Karachi, Pakistan | 19.8 | 20.8 | 22.5 | 113 | 145 | 162 | 8 | 10 | 10 | 1.3 | 2.0 | 2.0 |
| Delhi, India (using 12km data) | 16.4 | 17.6 | 18.0 | 91 | 111 | 117 | 14 | 21 | 26 | 1.4 | 1.8 | 2.1 |

Table 8 continued.

| (b) haze | $PM_{2.5}$ (μg/$m^3$) | | | Frequency (day/year) | | | Duration (day) | | | Relative Intensity (μg/$m^3$above 60) | | |
|---|---|---|---|---|---|---|---|---|---|---|---|---|
| | 2000 | 2050 RCP 6.0 | 2050 RCP 8.5 | 2000 | 2050 RCP 6.0 | 2050 RCP 8.5 | 2000 | 2050 RCP 6.0 | 2050 RCP 8.5 | 2000 | 2050 RCP 6.0 | 2050 RCP 8.5 |
| Delhi, India | 147.1 | 171.7 | 183.7 | 352 | 353 | 356 | 46 | 51 | 65 | 80.9 | 116.0 | 127.1 |
| Mumbai, India | 95.0 | 100.6 | 107.9 | 298 | 304 | 298 | 15 | 15 | 16 | 46.3 | 51.6 | 62.2 |
| Dhaka, Bangladesh | 70.9 | 79.3 | 101.2 | 206 | 229 | 271 | 7 | 8 | 9 | 33.8 | 41.7 | 61.0 |
| Karachi, Pakistan | 59.3 | 65.5 | 71.8 | 130 | 145 | 178 | 5 | 5 | 5 | 33.1 | 40.9 | 42.7 |
| Delhi, India (using 12km data) | 146.7 | 177.9 | 186.4 | 350 | 346 | 355 | 40 | 29 | 59 | 90.9 | 125.2 | 120.1 |

The intensification of heat extremes shown above is comparable to previous studies over this region when the uncertainty of regional warming projection is considered. In this study, there is projected regional warming of 1.6ºC from Decade 2000 to Decade 2050 (similar to Chaturvedi et al., 2012; 1.4ºC for Tw as in Table 7). More informative than the absolute value of change projected by a single model is how much of the enhancement, as shown above, can be mitigated by adopting a (moderately) low carbon emission pathway (e.g. RCP6.0). Our Decade 2050 simulation under RCP6.0 suggests the increase in frequency and duration in RCP8.5 can be cut by 33% and 66%, respectively, over South Asia (Table 7). The relative magnitude is largely consistent with simulated lower regional warming (1.0ºC increase from now to mid-century in RCP6.0 compared to a 1.6ºC increase in RCP8.5), suggesting the scalability of heat extremes statistics shown here to other low-warming scenarios (e.g. RCP2.6), at least for this region. The fractional increase quantified in previous studies is somewhat different due to various definitions of heat extremes, which are discussed next.

The daily averaged Tw of 25ºC, at the 88th percentile of climatological Tw over South Asia (Table 7), may seem not very "extreme", but indeed corresponds to the level of heat stress experienced in two major multi-week heatwave episodes (May 2010 and May 2015) in India that reportedly led to thousands of deaths (Figure 8). As a sensitivity test, using a weaker threshold of 18ºC of Tw (the blue line in Figure 8, when the heat-related causality just started to be reported as in Mora et al., 2017), the Decade 2000 occurrence is more frequent at 168 days/year and the fractional increase into the future is much weaker (14%, Table 6) than when the 25ºC Tw is used as the threshold.

The lower thresholds of 18ºC and 25ºC Tw (following Mora et al., 2017) are established empirically based on numerous multi-days to multi-week heatwave events that have led to major

casualty to vulnerable groups such as children and elderly. The lower threshold of Tw should be clearly distinguished from Tw thresholds of 30ºC to 35ºC adopted in some earlier studies (Sherwood and Huber, 2010; Lemke and Kjellstrom, 2012; Van Oldenborgh et al., 2017; Kang and Eltahir, 2018; Table 6), which refers to a lethal physiologic limit that can cause instantaneous hyperthermia, even to healthy active outdoor workers, within just a few hours of exposure (presumably during the daytime).

When a higher threshold of Tw 28ºC is adopted as a sensitivity test, the Decade 2000 frequency is much rarer (2 days/year averaged across South Asia) compared to hundreds of days with heat stress when the lower thresholds of Tw were used, and the fractional increase in the future is, understandably, much stronger (>400%, Table 6). This is similar to the case when using a strict definition of heat extremes by requiring individual episodes to be at least two consecutive days (e.g., Xu et al., 2018). The relative future increase in frequency under this stricter requirement will also be larger (71% as opposed to 65%, Table 6).

Earlier studies, if using temperature alone without considering the humidity effect, omit the documented evidence that the human body responds negatively to high humidity conditions (Liu et al., 2014). Using temperature alone would underestimate the future increase of heat extremes. For example, if a threshold of T>31ºC is selected (intentionally) that leads to a Decade 2000 frequency close to 48 days/year (similar to Tw>25ºC, Table 6), the same model projects a 14-29% increase in frequency vs. 38-58% using Tw, and a 13-20% increase in duration vs. 50-83% using Tw. The reason for the underestimation is that relative humidity over these tropical regions is projected by the latest global climate models to increase with global warming as well (Figure 13, Figure 11; see also Dai, 2006; Sherwood and Fu, 2014).

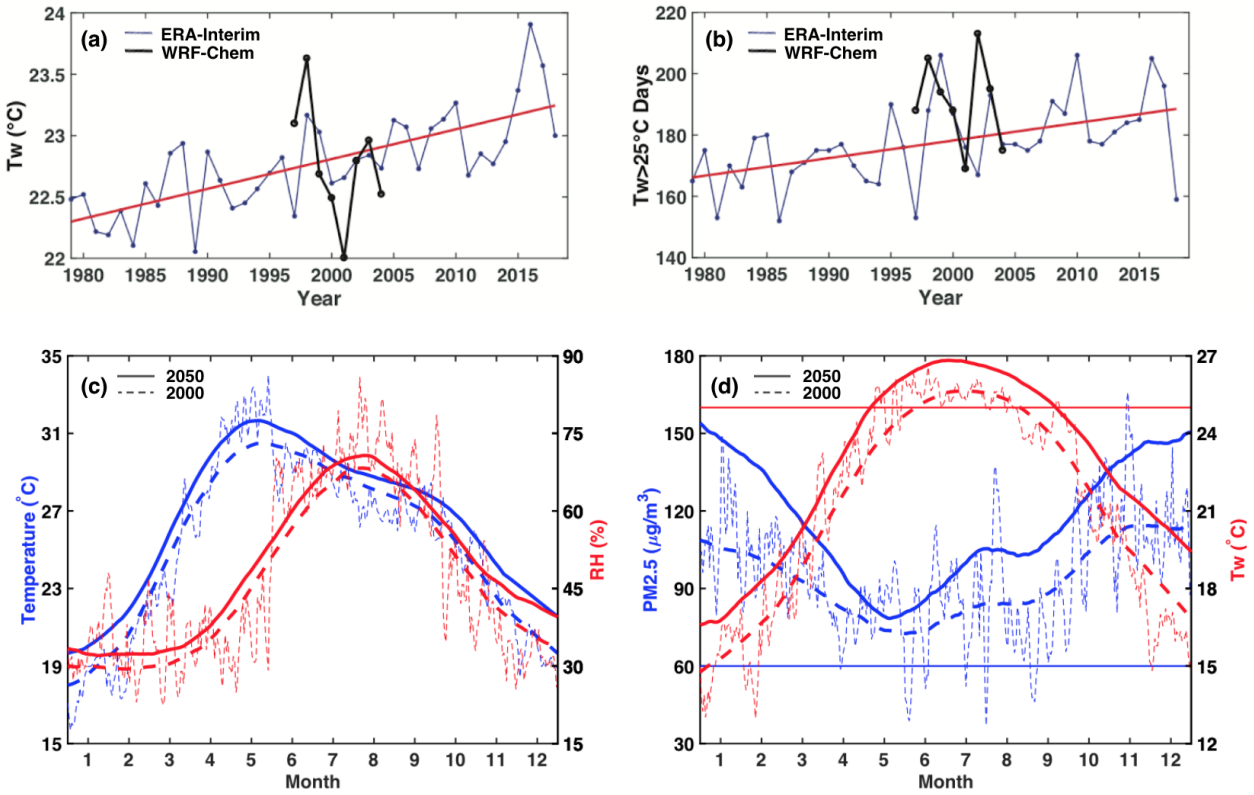


Figure 13. Simulated and observed changes over Dhaka, Bangladesh. (a): Tw in ERA-Interim (the thin blue line) and WRF-Chem (the thick black line). The red line is the linear fit of ERA-Interim data. (b): same as (a) but for heat extremes frequency (day/year) (c): Climatologically averaged temperature based on WRF-Chem (blue, left Y-axis) and relative humidity (red, right Y-axis) as a function of the month. The thick dashed lines are for the Decade 2000, and the thick solid line is for the Decade 2050). The thin dashed lines with high-frequency fluctuation are the daily time series in the year of 1997. (d): same as (c), but for WRF-Chem simulated $PM_{2.5}$ and Tw (after the bias correction). Reprinted from Xu et al., (2020).

Even if the relative humidity stays the same, there will still be an underprediction of heat stress risks if using T alone, just because of the greater health effect of moisture in a warmer climate (Figure 8). The additional benefit of combining temperature and humidity in heat stress assessments is that the model deficiency in simulating the two (Figure 14; Willett and Sherwood,

2012) tends to offset. Similarly, the model discrepancies in projecting temperature and relative humidity tend to be the opposite (Fischer and Knutti, 2013).

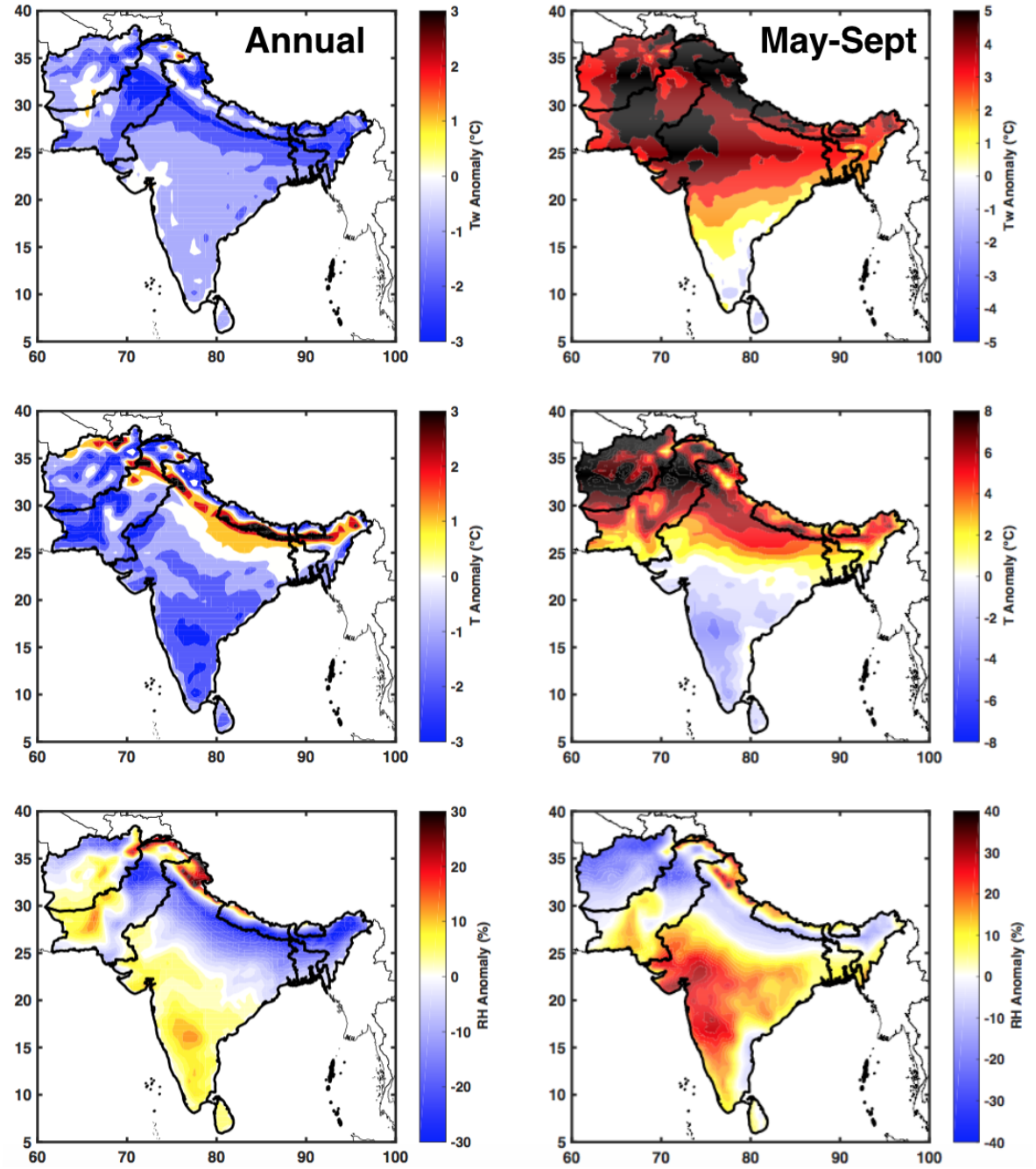


Figure 14. (Top) The bias of simulated Tw in WRF-Chem, when contrasted to ERA-Interim during the Decade 2000. (Left) the annual average. (Right) warm-season only, including May to September. (Middle) Same as the top panels but for temperature. (Bottom) Same as the top panels but for relative humidity. Values are only shown for seven South Asian countries (Afghanistan, Bangladesh, Bhutan, India, Nepal, Pakistan and Sri Lanka) within the thicker borderlines. Reprinted from Xu et al., (2020).

A potential underestimation of future increase in heat stress is also likely in previous studies (e.g. Im et al., 2017) if using daily maximum temperature instead of daily mean temperature (unless the specific health and economic concern are lost labor hours and occupational mortality of outdoor workers). There is only a 25-60% increase in frequency when a Tw_max threshold of 26ºC is used (with the intention that a similar Decade 2000 frequency is found, Table 6), in contrast to the daily mean Tw used in this study (with a 38-58% increase in frequency). The future increase in health risk, when using Tw_max instead of daily averaged Tw as here, can be underestimated because: (a) cooler nights can provide a relief period for the human body to rest and recover (Obradovic et al., 2017) and (b) nighttime temperatures tend to increase faster than daytime temperatures under global warming (Davy et al., 2017).

Are the simulations here (close to 10 years in each case) long enough to provide a robust projection of regional climate change? One may question that a single realization of 8 to 9 years, might not be sufficient because a single decade of simulation can be heavily influenced by the phase of decadal variability mode such as AMO. We argue our results are robust for the following two reasons: First, our simulation for Decade 2000 is highly constrained by observed meteorology (using ERA-Interim as the benchmark for bias correction) and thus represents the real meteorology as observed during those 8 years. Second, our Decade 2050 simulation is driven by boundary conditions provided by multiple runs from a global climate model (CESM1), and thus has effectively accounted for the decadal fluctuation of the climate system.

Are the projected changes here similar to other global climate models? The mean temperature for the South Asia region is 20.2ºC in the Decade 2000. At the Decade 2050, this region would experience a 1.5ºC warming compared to the Decade 2000 under RCP8.5 and a 1.0ºC warming under RCP6.0. These numbers are within the uncertainty range of global climate model

output in Coupled Model Intercomparison Project phase 5 (CMIP5), consistent with the fact that CESM1 has a moderate climate sensitivity compared with other CMIP5 models. For reference, the CMIP5 models yield a mean 2050 warming of 1.6ºC for RCP8.5 (Figure 11, fourth row) and 1.2ºC for RCP6.0 with an uncertainty of a few tenths of a degree (also seen in Figure 11 of Chaturvedi et al., 2012).

### 3.3.2 Human exposure to elevated heat risks

Due to negative health consequences, it is important to assess human exposure to heat extremes and the reasons for future changes. We find that population-weighted heat extremes frequency in the Decade 2000 is 83 days/year, larger than the area-weighted estimate (45 days/year) and is projected to increase by 51% to 125 days/year under RCP8.5 (Table 9). The population projection (under the SSP5 scenario; Jones and O'Neill, 2016) are spatially resolved and are consistent with the socio-economic drivers of RCP emissions. Similar results were also found for the increase in heat extremes duration to 13 days (under RCP8.5) from 9 days in the Decade 2000 (Table 9).

Table 9. Similar to Table 7 but for population-weighted results, as opposed to area-weighted results. Note the higher values here compared to Table 3, because co-location of population and extreme events tend to enhance risks, in particular for haze (part b of this table). Reprinted from Xu et al., (2020).

| (a) heat | Tw (°C) | | | Frequency (day/year) | | | Duration (day) | | | Relative Intensity (°C above 25) | | |
|---|---|---|---|---|---|---|---|---|---|---|---|---|
| | 2000 | 2050 RCP 6.0 | 2050 RCP 8.5 | 2000 | 2050 RCP 6.0 | 2050 RCP 8.5 | 2000 | 2050 RCP 6.0 | 2050 RCP 8.5 | 2000 | 2050 RCP 6.0 | 2050 RCP 8.5 |
| Afghanistan | 6.0 | 7.3 | 7.4 | 0 | 0 | 0 | 0 | 0 | 0 | 0.3 | 1.1 | 2.5 |
| Bangladesh | 22.3 | 23.4 | 24.4 | 166 | 200 | 219 | 14 | 19 | 21 | 1.3 | 1.9 | 2.2 |
| Bhutan | 11.3 | 13.9 | 14.5 | 0 | 3 | 7 | 0 | 1 | 1 | 0.0 | 0.0 | 0.1 |
| India | 20.4 | 21.6 | 22.1 | 77 | 109 | 125 | 8 | 11 | 12 | 0.9 | 1.4 | 1.6 |
| Nepal | 14.5 | 16.8 | 17.3 | 20 | 42 | 53 | 2 | 4 | 5 | 0.4 | 0.8 | 0.9 |
| Pakistan | 16.8 | 18.4 | 18.7 | 74 | 92 | 101 | 10 | 11 | 14 | 1.5 | 2.0 | 2.2 |
| Sri Lanka | 23.7 | 24.6 | 25.1 | 43 | 131 | 193 | 3 | 6 | 11 | 0.3 | 0.5 | 0.7 |
| South Asia | 19.9 | 21.0 | 21.4 | 83 | 110 | 125 | 9 | 11 | 13 | 1.0 | 1.5 | 1.7 |

Table 9 continued.

| (b) haze | $PM_{2.5}$ ($\mu g/m^3$) | | | Frequency (day/year) | | | Duration (day) | | | Relative Intensity ($\mu g/m^3$ above 60) | | |
|---|---|---|---|---|---|---|---|---|---|---|---|---|
| | 2000 | 2050 RCP 6.0 | 2050 RCP 8.5 | 2000 | 2050 RCP 6.0 | 2050 RCP 8.5 | 2000 | 2050 RCP 6.0 | 2050 RCP 8.5 | 2000 | 2050 RCP 6.0 | 2050 RCP 8.5 |
| Afghanistan | 73.3 | 69.8 | 82.9 | 60 | 19 | 89 | 4 | 3 | 70 | 13.3 | 9.8 | 22.9 |
| Bangladesh | 88.2 | 94.7 | 106.7 | 137 | 184 | 216 | 5 | 7 | 9 | 28.2 | 34.7 | 46.7 |
| Bhutan | 70.9 | 48.1 | 67.6 | 7 | 4 | 28 | 2 | 1 | 2 | 10.9 | 5.4 | 10.3 |
| India | 80.4 | 82.1 | 95.1 | 123 | 113 | 200 | 5 | 5 | 9 | 20.4 | 22.1 | 35.1 |
| Nepal | 70.2 | 66.0 | 72.6 | 25 | 29 | 77 | 3 | 2 | 4 | 10.2 | 8.4 | 13.4 |
| Pakistan | 79.2 | 86.0 | 93.1 | 105 | 143 | 206 | 4 | 6 | 10 | 19.9 | 26.0 | 33.3 |
| Sri Lanka | 68.3 | 55.8 | 69.2 | 1 | 1 | 3 | 2 | 1 | 2 | 8.3 | 2.3 | 9.2 |
| South Asia | 80.6 | 82.6 | 94.7 | 118 | 117 | 194 | 5 | 5 | 11 | 20.6 | 22.7 | 34.7 |

The population-weighted average in Table 9 tends to be larger than the area-weighted results (Table 7) because populations are concentrated in the Indo-Gangetic Plain and coastal regions (Figure 15) where the heat extremes also tend to increase the most (Figure 10). The co-location of heat extremes and population density is particularly worrisome considering the lower-income and GDP over the Indo-Gangetic Plain (Im et al., 2017), which suggests that the most vulnerable population groups will be subject to stronger heat extremes in the future.

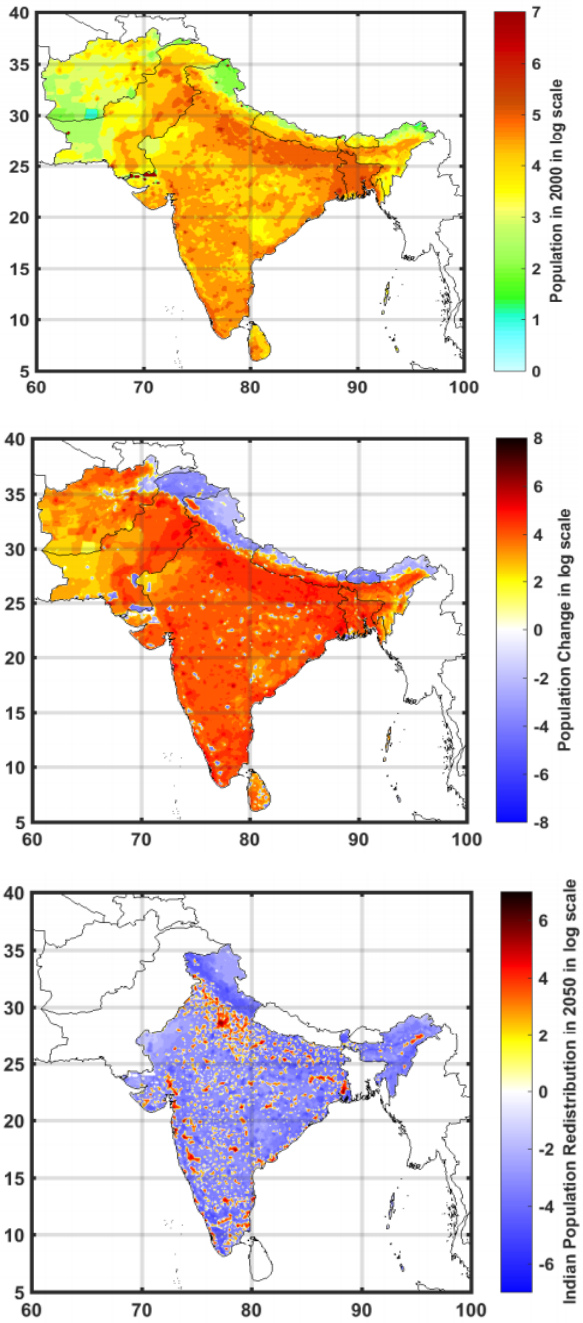


Figure 15. (Top and Middle Rows) Decade 2000 population count and its change at Decade 2050. Note the logarithmic scale (1 for 10, 2 for 100, 3 for 1000, -1 for -10, -2 for -100, -3 for -1000, etc.) (Bottom row) India population redistribution at Decade 2050 only due to migration, so that the regional average of this figure is zero. Only the redistribution of the population within India is considered in the bottom panel because it can be interpreted as the effects of demographic shift due to domestic factors (e.g., urbanization). Reprinted from Xu et al., (2020).

Human exposure to heat extremes is dominated by three nations: Bangladesh, India, and Pakistan. Over India, 189.7 billion people-days of heat exposure per year are projected in Decade 2050 (Table 10), a 149% increase from the Decade 2000. Another health-related quantity is "accumulated relative intensity", which is the product of frequency (number of days) and relative intensity (Tw within extreme events minus the selected threshold) (Table 10 and Figure 16). This quantity factors in both the prolonged exposure and the severity of heat extremes. Decade 2050 will see 338 billion people ºC days/year (under RCP8.5), a daunting 258% increase from the Decade 2000. The larger relative increase (258% vs. 149%) is consistent with the enhanced severity of heat extremes (with the relative intensity increasing from 1.0 to 1.7ºC) (Table 9 and Figure 10).

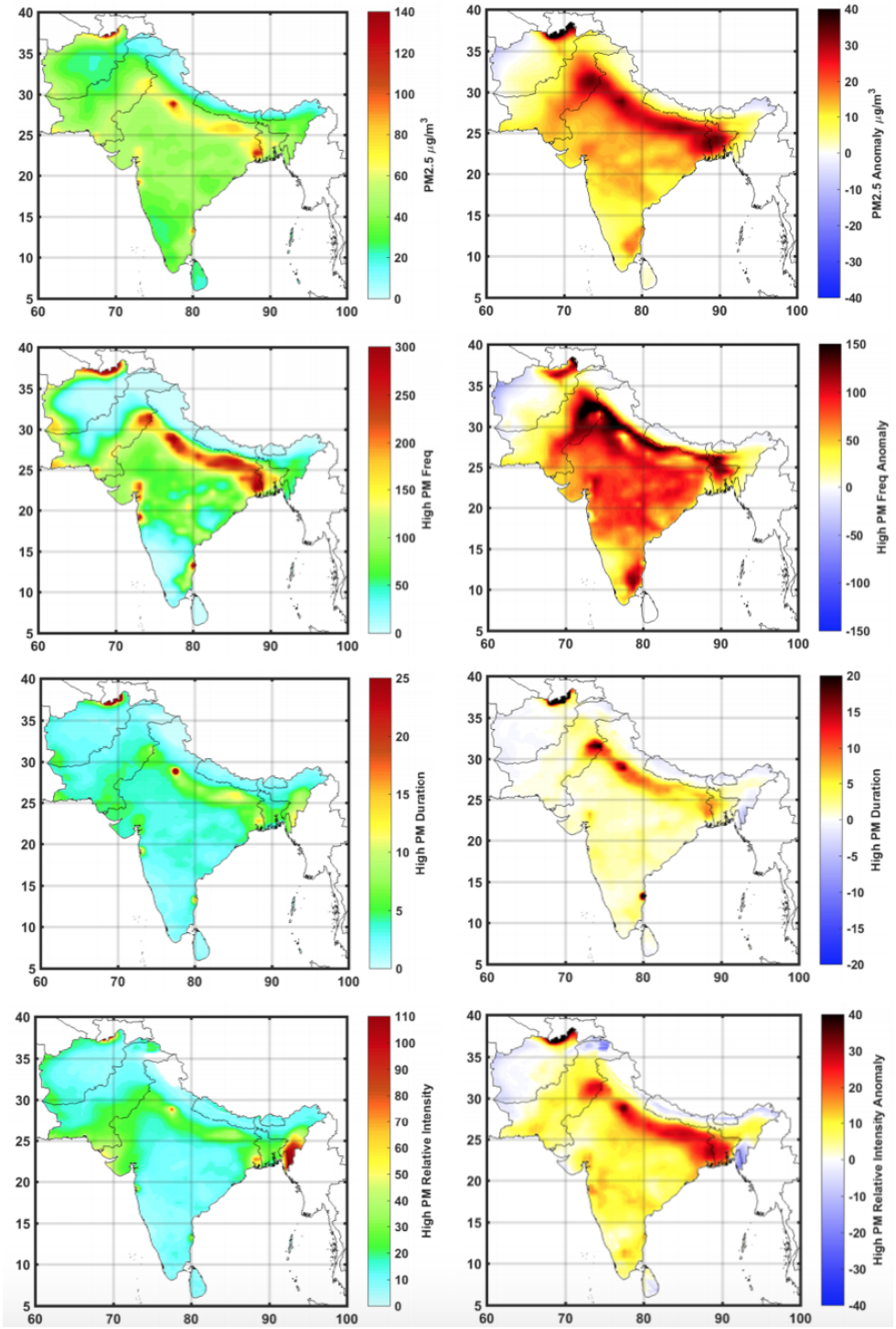


Figure 16. Similar to Figure 11, but for haze extremes. $PM_{2.5}$ concentration, haze extremes frequency, duration and relative intensity in the left column and changes at the Decade 2050 under RCP8.5. Reprinted from Xu et al., (2020).

Table 10. Population exposure to heat and haze extremes. Reprinted from Xu et al., (2020).

| (a) heat | Frequency exposure (billion person*day/year) | | | Accumulated Relative Intensity exposure (billion person*°C*day/year) | | |
|---|---|---|---|---|---|---|
| | 2000 | 2050 RCP6.0 | 2050 RCP8.5 | 2000 | 2050 RCP6.0 | 2050 RCP8.5 |
| Bangladesh | 22.1 | 33.5 | 36.7 | 30.5 | 65.1 | 83.7 |
| India | 76.2 | 165.2 | 189.7 | 94.4 | 266.9 | 338.1 |
| Pakistan | 10.6 | 22.6 | 24.9 | 17.3 | 48.6 | 58.7 |
| South Asia | 110.2 | 225.8 | 257.3 | 142.8 | 383.6 | 485.5 |

| (b) haze | Frequency exposure (billion person*day/year) | | | Accumulated Relative Intensity exposure (billion person*μg/$m^3$*day/year) | | |
|---|---|---|---|---|---|---|
| | 2000 | 2050 RCP6.0 | 2050 RCP8.5 | 2000 | 2050 RCP6.0 | 2050 RCP8.5 |
| Bangladesh | 18.3 | 30.9 | 36.3 | 512.4 | 1089.2 | 1744.9 |
| India | 121.7 | 171.1 | 303.0 | 3322.2 | 5531.4 | 12637.8 |
| Pakistan | 15.1 | 35.4 | 51.1 | 349.4 | 1027.0 | 1896.2 |
| South Asia | 157.0 | 240.0 | 398.9 | 4224.1 | 7674.0 | 16597.3 |

The increase in population exposure is due to three factors: future warming, population growth, and to a lesser extent, population redistribution arising from migration and urbanization.

The warming alone explains 41% of the total increase, while the population growth explains about 39% (Table 11). Interestingly, the redistribution of population in India (Figure 1, while keeping total population fixed) also contributes 1.5% (1.6 billion people-day/year) of the total increase in human exposure to heat extremes (Table 11), which is due to future urbanization and well-captured urban heat island effects in this high-resolution regional climate model (Figure 10). We note that the exposure numbers presented here are the maximum potential human exposure (Mishra et al., 2017) that do not account for the time spent indoors with active cooling (which could also change from now to future due to air conditioning penetration into household in developing countries (Auffhammer, 2014)), which requires estimates of sub-daily population distribution in cities.

Table 11. Separating the contribution of population growth and heat/haze conditions to increased human exposure (unit: billion person*day/year). The percentage of relative contribution to the total increase in the Decade 2050 under RCP8.5. The population redistribution (but not population growth) for India contributes to 1.5% (1.7 billion person*day/year) of the change in human exposure to heat extremes and 4.7% (4.0 billion person*day/year) of the change in human exposure to haze extremes. Reprinted from Xu et al., (2020).

| | Change in haze exposure due to population growth | Change in haze exposure due to $PM_{2.5}$ emission increase | Change in heat exposure due to population growth | Change in heat exposure due to climate change |
|---|---|---|---|---|
| Bangladesh | 1.2 (10%) | 8.9 (71%) | 5.7 (39%) | 7.0 (48%) |
| India | 17.7 (21%) | 43.9 (51%) | 42.3 (37%) | 46.3 (41%) |
| Pakistan | 2.1 (14%) | 7.1 (47%) | 8.5 (59%) | 3.2 (23%) |
| South Asia | 21.6 (19%) | 60.2 (52%) | 57.1 (39%) | 59.7 (41%) |

In addition to the absolute value of human exposure, other important factors worth assessing are the fractions of population and land exposed to the prolonged heat extremes. In the Decade 2000, about 61% of the population within South Asia experienced heat extremes for more than 60 days per year, while in the future, 80% of the population will experience similar extreme heat conditions (Table 12). We estimate the total land fraction impacted by heat extremes for more than 60 days to be 35% in the Decade 2000 (Figure 17). That number will grow to 56% (RCP8.5)

or 48% (RCP6.0) in the Decade 2050. Those estimates are robust regardless of whether the model simulated Tw is corrected based on reanalysis or not (Table 12).

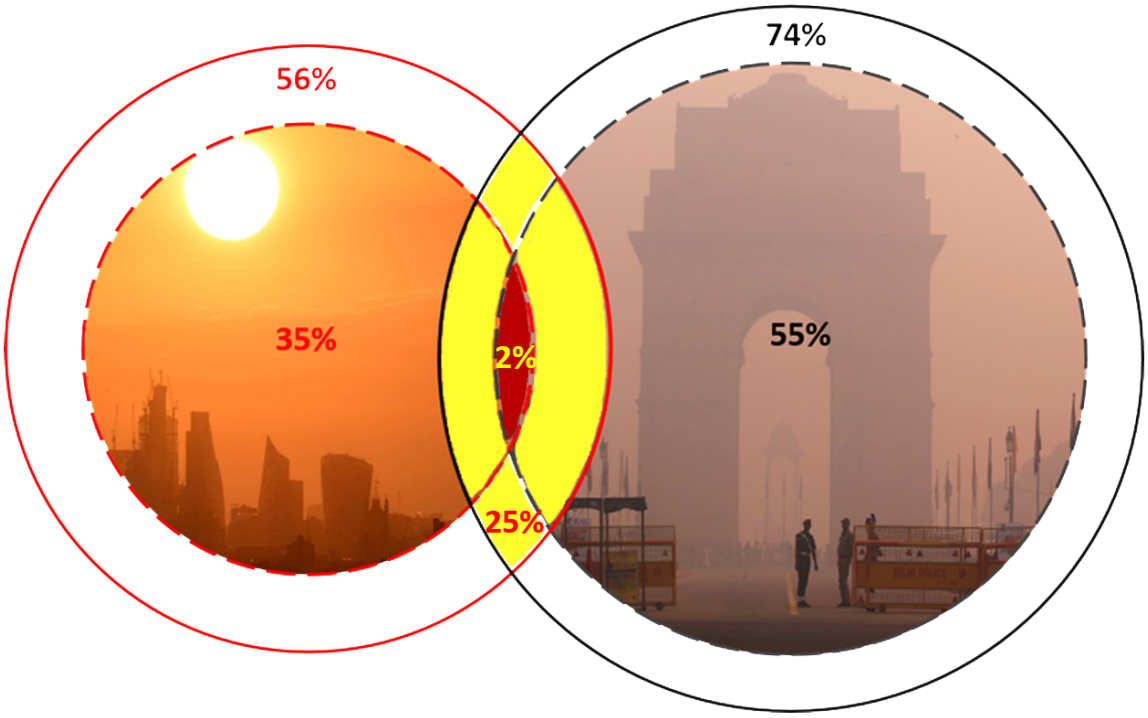


Figure 17. An illustration of the land fraction impacted by prolonged (60 days or more) extremes. The area of each circle corresponds to the South Asia land fraction with prolonged heat (red) and high-PM (black) extremes (Table 2a). The smaller dash circles are Decade 2000 and the larger solid circles are Decade 2050. The overlapping area of smaller dash circles (red) and larger solid circles (yellow) corresponds to the multi-fold increase in the land area subjected to prolonged HHH (from 2% to 25%). The inserted images represent heat (left, credit: Skynews) and high-PM conditions (right, India Gate, credit: ibtimes.co.in). Reprinted from Xu et al., (2020).

Table 12. (a) The land area fraction within South Asia that is exposed to 60 or more days of heat extremes and high-PM extremes, and 60 more days of joint events of heatwave and high-PM. (b) The population fraction. The numbers in parentheses are based on the original model output. Reprinted from Xu et al., (2020).

| (a) Area fraction | Heat > 60 days | high-PM > 60 days | heatwave and high-PM > 60 days |
|---|---|---|---|
| Decade 2000 | 35% (37%) | 55% | 2% (3%) |
| Decade 2050 under RCP6.0 | 48% (49%) | 41% | 10% (9%) |
| Decade 2050 under RCP8.5 | 56% (54%) | 74% | 25% (24%) |

| (b) Population fraction | Heat > 60 days | high-PM > 60 days | heatwave and high-PM > 60 days |
|---|---|---|---|
| Decade 2000 | 61% (64%) | 73% | 8% (9%) |
| Decade 2050 under RCP6.0 | 74% (74%) | 62% | 24% (21%) |
| Decade 2050 under RCP8.5 | 80% (80%) | 90% | 52% (50%) |

### 3.3.3 A Hazier Future

Air pollution has been recognized as a modulating factor, which can affect the health impact of heat extremes (Gosling et al., 2009). Similar compounding effects have also been found when assessing air quality-related mortality as a function of background temperature (Jackson et al., 2010). We next describe the characteristics of high-PM extremes before discussing the joint occurrence and risk.

When using daily average surface $PM_{2.5}$ mass concentration of 60 μg/m3 as the definition of high-PM extremes (CPCB, 2009), we find an increase in the frequency and duration of high-PM extremes by 76% and 125%, respectively, from its Decade 2000 values of 75±9 days/year (frequency) and 4 days (mean duration) (under RCP8.5; Table 7). This is in line with the mean $PM_{2.5}$ concentrations increase of 30% driven by an increase in regional PM emissions of 77% in RCP8.5 (Figure 6), while the climate change itself facilitates a stronger removal of $PM_{2.5}$ (Wu et al., 2019).

When using other threshold levels suggested by the World Health Organization, Environmental Protection Agency of the United States, or Chinese agencies, the main pattern of high-frequency regions remains the same, but the magnitude of future change would vary (Figure 9). If a lower threshold of air pollution is used, more days (actually most of the days in some cities) will be classified as "high-PM extremes", and its fractional increase into the future will be rather small. We here use a higher threshold of $PM_{2.5}$ to illustrate to the "extreme" nature of high-PM issues. Note that we also adopted a similar philosophy in choosing a higher threshold of heat (25ºC in Tw), again, to emphasize the rarity and extremity of those events.

Similar to heat extremes, population-weighted results are considerably higher than area-weighted results for the high-PM extremes. The population-weighted average of high-PM

extremes frequency is 118 days/year (Table 9) compared to the area-weighted average of 75 days/year (Figure 18). This is a direct result of the strong co-location of emission sources (Figure 6), $PM_{2.5}$ concentrations (Figure 16), and the urban population (Figure 15).

The population exposure to high-PM extremes frequency (number of people who experience extremes multiplied with the number of days exposed to the extreme; person*day/year) is projected to increase under RCP6.0 and RCP8.5 scenarios by 154% and 293% (Table 10), respectively. The lower population exposure to high-PM extremes under RCP6.0 is also largely due to lower emission growth. The population exposure to the accumulated relative intensity is 4.2 trillion people*$\mu g/m^3$*day/year in the Decade 2000 and will increase by 293% in the Decade 2050. Note that the larger fractional change in accumulated relative intensity (as the product of frequency and relative intensity) indicates that the severity of high-PM extremes is getting worse (Figure 16). The multi-fold increase in human exposure is again driven by both population growth and worsening air quality. But in the case of high-PM extremes, the population growth plays a smaller role (19% due to population growth vs 52% contributed by the hazier atmosphere). This is different from the stronger role of population growth for determining the increase in exposure to heat extremes (43% due to population growth vs 38% due to warming). The urbanization effect is also more important for high-PM (4.7% as opposed to 1.5% for heat shown previously).

Since major air quality improvement initiatives have been planned by local governments, we also quantified the high-PM occurrences at the city level. Within South Asia, many cities are subject to a major increase in high-PM extremes but with different levels of severity (Table 8). For example, Mumbai is projected to experience a 34% increase in relative intensity. Cities such as Karachi are prone to the future growth of high-PM weather frequency by 37%, but some other cities appear to already experience ~300 days of high-PM extremes during the Decade 2000. The

city-level results are not particularly sensitive to the spatial resolution of the model simulation. When the 12 km resolution simulation over the inner domain is utilized (higher than the 25 km used by Im et al., 2017, but lower than the 4 km grid resolution used by Hu et al., 2015 for the smaller California domain), both the present-day and future $PM_{2.5}$ in Delhi remain largely invariant compared to the 60 km simulation. However, the relative intensity for high-PM extremes documented here is slightly higher at 90.9 as opposed to 80.9 $\mu g/m^3$.

### 3.3.4 heatwave and high-PM hazards (HHH)

Lastly, we quantify the joint heatwave and high-PM hazards (HHH), which has been largely missing in all previous studies. The Decade 2000 frequency for HHH is low at 12±2 days/year for South Asia (Figure 18), and 13 days/year for India. In the Decade 2050, the frequency would increase to 33±5 days/year, a 175% rise (under RCP8.5), much higher than the relative increase in heatwave or high-PM alone (73% to 76%). A stronger enhancement in HHH is also seen for other extreme quantities such as the mean duration (with a relative increase of 79%) and the relative intensity (with an increase of 0.4 ºC and 7.0 $\mu g/m^3$) (Figure 18 and Figure 19).

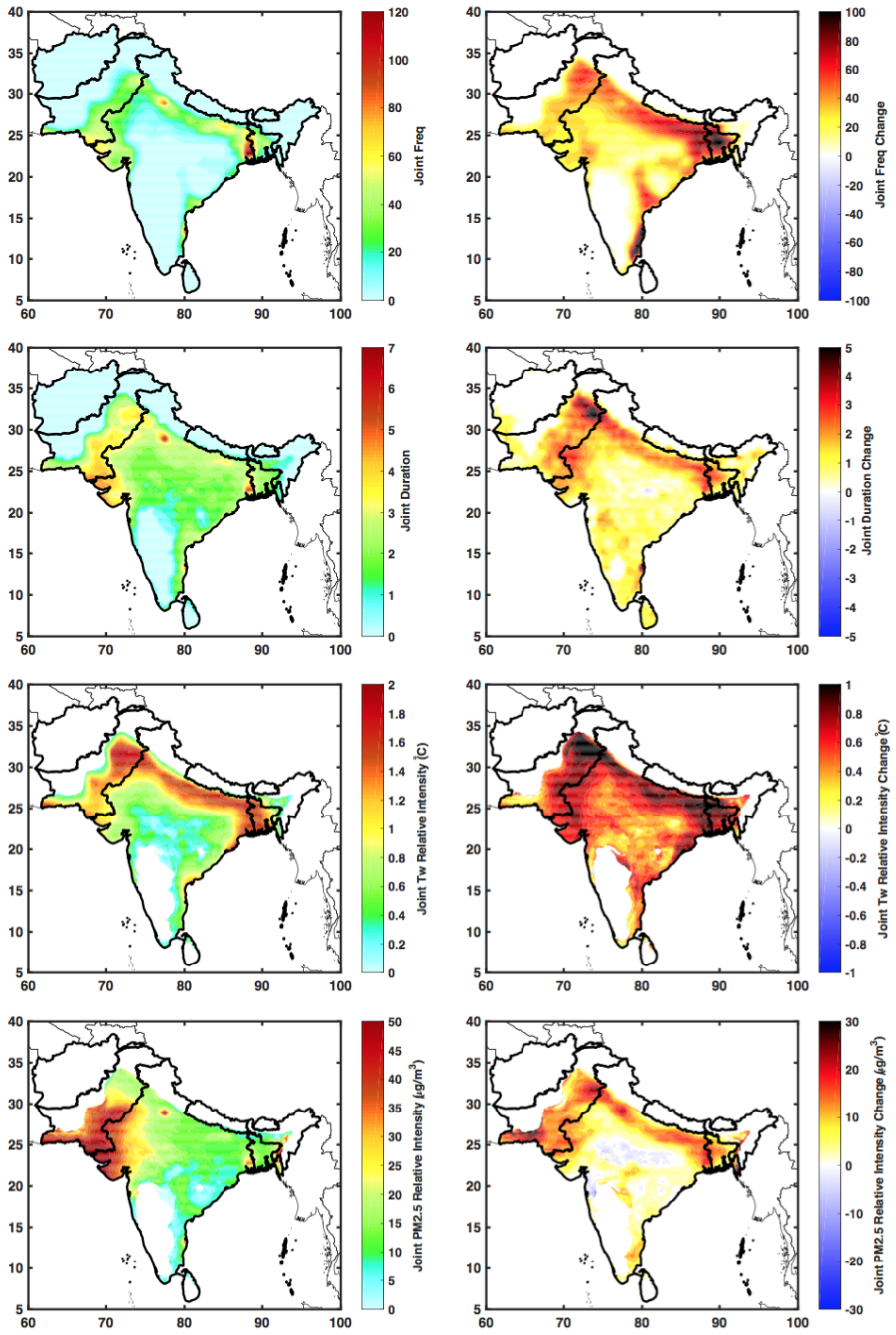


Figure 18. (Top) Frequency of joint heat and haze hazards (HHH, Tw>25ºC and PM>60 μg/m$^3$) in the Decade 2000 and the change in the Decade 2050 under RCP8.5. (Middle row) duration. (Bottom two rows) relative intensity (in ºC and μg/m$^3$). The white area in the thicker borderline is regions where no heat extremes occur in the Decade 2000. Reprinted from Xu et al., (2020).

The changes in HHH are driven mostly by a larger increase over the spring to summer transitional period and that results in a greater number of days falling into the high-Tw/high-PM quadrant as illustrated in Figure 19 using the data over the four cities. Figure 13 (bottom panels) shows the seasonal variation of temperature, RH, Tw, and $PM_{2.5}$. Moist monsoon season is relatively cooler than the pre-monsoon season but accounting for the humidity effects leads to an extended "hot" season (see Tw during April to October in Figure 13). A key feature is the extension of pre-monsoon high-PM (pollution season) into the monsoonal season, and concurrently, the extension of heat extremes into pre-monsoon season. These two factors, when simultaneously occurring, contribute to the multi-fold increase in the frequency of the joint hazards.

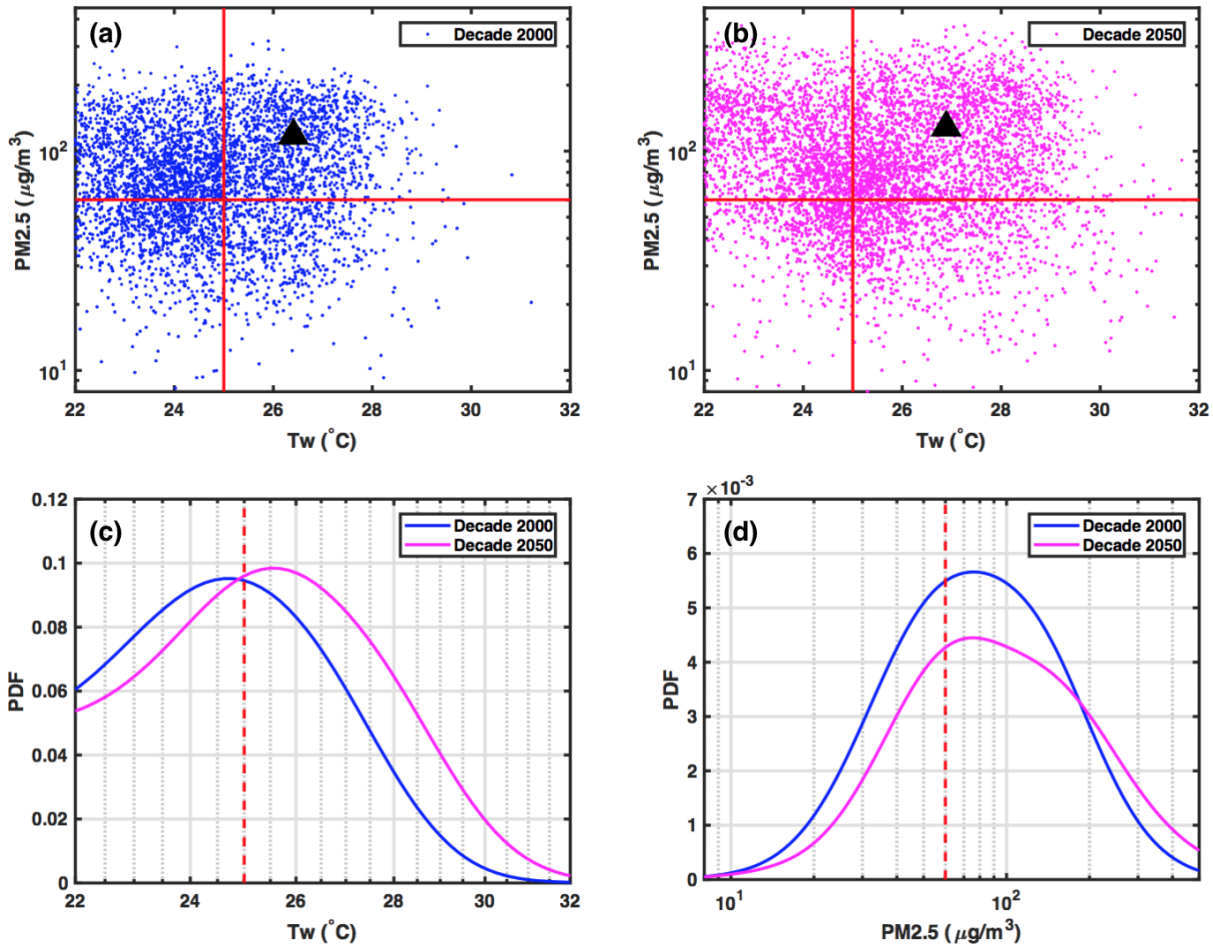


Figure 19. (a) and (b): The daily values over four major cities (Delhi, Mumbai, Dhaka, and Karachi). The X-axis is for Tw and the Y-axis (in logarithmic scale) is for $PM_{2.5}$ surface concentration. (a) is for the Decade 2000 and (b) is for Decade 2050 under RCP8.5. Red horizontal and vertical lines are thresholds for heatwave and high-PM extremes. Black triangles indicate the average of all HHH events in the upper right quadrant. (c) and (d): Probability density function (PDF) for Tw and $PM_{2.5}$ over the four cities. Red dashed lines are thresholds for the heatwave and high-PM extremes. Reprinted from Xu et al., (2020).

The rarity of HHH frequency in the Decade 2000 also means there is a larger relative change in the future for area and population impacted by prolonged HHH events (a factor of 12 increase for exposed land area, and a factor of 6.5 increase for the exposed population; Table 7). The multi-fold increase in the land or population fraction affected by HHH, as opposed to the 31-

60% increase in heat-affected and 23-35% high-PM-affected land or population fraction, when computed separately, is the most remarkable message of this study (Table 7 and Figure 1). The multi-fold increase in land exposed to HHH is illustrated in Figure 17 by the overlapping area of black and red circles and will pose significant difficulties for adaptation. Given the potential underestimation of HHH health impacts, our results suggest a major increase in HHH-related mortality is on the horizon. Evidence-based quantification of HHH related mortality is clearly needed to account for the compounding effects of two types of extremes, and also to avoid double-counting when linearly adding the mortality estimates from empirical approaches.

Although beyond the scope of the paper, one can investigate extreme ozone (e.g., >70 ppb) because many of these regions are very prone to temperature-ozone overlap. Therefore, it will be interesting to assess the occurrence of all three. Our model simulates ozone concentration well (Kumar et al., 2018), even though one limitation of the current WRF-Chem simulations is that it does not include ozone-radiation interactions, which might be not as large as aerosol effects.

However, in general, the monthly mean value rarely exceeds 70 ppb (see Dhaka in Figure 4 of Kumar et al., 2018), thus ozone is less of concern for local air quality as of now. Note that it is possible the NOx to VOC ratios will change and ozone will be in exceedance in the future, which has started to happen in China. For North America and other regions, the co-occurrence of heat extreme and ozone can also be very important, as recently studied by Schnell and Prather (2017) and (Meehl et al., 2018). Thus, the extreme occurrence of all three could be a very interesting question to look at in future studies, for other regions.

## 3.4 Concluding Remarks

Heat extremes occurrence worldwide has increased in the past decades, especially when accounting for the amplification due to the humidity effect and urban heat island influences. At the same time, many cities are facing severe air pollution problems featuring high-PM episodes (high concentration of particulate matter due to various sources) that last from days to weeks. Despite the potential compounding effects on vulnerable population groups and complex dynamical-physical-chemical interactions, the characteristics and potential predictive skills of the co-occurrence of heatwave and high-PM hazards (HHH) have not been extensively studied. Although previous studies have suggested common meteorological drivers for these two types of extremes (Schnella and Prather, 2017) and potential amplifying feedbacks (Cao et al., 2016), an integrated assessment of human exposure to the joint occurrence of heatwave and high-PM extremes and possible future changes has been missing (except for a few studies at local scale; Doherty et al., 2009; Jackson et al., 2010).

A regional-scale assessment for the present-day heatwave and high-PM occurrence and future changes is presented here. The most crucial result here is that the frequency of these rare HHH events would increase by 175% in the future, which is in contrast to the 73-76% increase when heatwave or high-PM are assessed individually. Consequently, the land fraction affected by prolonged exposure to HHH events will increase by more than 10-fold rather than 35 to 60% when the heatwave or high-PM are studied separately. The unprecedented worsening of air quality and regional climate, if occurring in just a few decades, pose great challenges to adaptation. If the air pollution emission were not elevated as much as in projected in RCP8.5, then the high-PM extreme will not worsen. For example, under RCP6.0, the frequency of high-PM will decrease by 11% and HHH will only increase by 58%.

Our results suggest that the thermodynamic effect of regional warming leads to the increase in heat extremes, and the PM emission increase (as assumed in RCP8.5) is the first-order factor leading to an increase in the high-PM extremes. Other questions remain. How would atmospheric circulation (stagnation) and precipitation play a secondary role? How do the high-PM and heat interact with each other (e.g. heat extreme amplifying the high-PM concentration or a high-PM layer mitigating the intensity of urban heat island)? Those will need to be addressed in future studies because of the limitation of the current model set up. The main purpose of this study is to bring forth a greater awareness of the potential larger increase in the coincidence of two stressors. Our results have broad implications, both scientifically and societally. The quantification, projection, and communication of joint risks of the co-occurrence of physical and chemical weather extremes are important for public health and urban planning. The mechanisms have been examined before for individual cases, but the findings are often scattered amongst different research communities with limited integration. A holistic view of the health impacts of the heatwave and high-PM hazards (HHH) is therefore urgently needed.

### 3.5 Summary of the PM and Heat

we constructed a composite index: HWII, which utilizes the ambient meteorology to predict the $PM_{2.5}$ levels and we expect a more favorable environment for air pollution dispersions in Indian Subcontinent by 2050s. However, the simulated results suggested that the future pollution levels tend to increase. The contradiction comes from the enhanced emissions, which tend to overwhelm the favorable meteorological fields in the future.

In addition, we presented a regional-scale assessment for present-day heat and haze occurrence and along with their future changes. We selected three major metrics: frequency,

duration and relative intensity to characterize the occurrences of heat and haze extremes. Under RCP 8.5 scenario, all metrics are projected to increase while maintaining an RCP 6.0 pathway is much more ideal from the public health perspective. Moreover, the rare heat and haze hazards (HHH) would have large future increases, in contrast to smaller increases in heat or haze when assessed individually and such alarming increases are only few decades away, posing great challenges for adaptations.

# CHAPTER IV

# IMPROVE CBMZ-MAM3 IN THE WRF-CAM5

## 4.1 Introduction

Atmospheric chemistry is closely related to air quality, climate change, and human being's livelihood. Subjects range from the ozone hole in Antarctica (Thompson et al., 2011) to air pollution in major metropolitans (Molina and Molina, 2004) and from rising global $CO_2$ levels (Pachauri et al., 2014) to climate forcings of air particles (Maria et al., 2004) are all within the scope of such a research field. The Weather Research and Forecasting (WRF) model (Skamarock et al., 2005) coupled with Chemistry (WRF-Chem; Fast et al., 2006; Grell et al., 2005) has wide applications in both research and forecast areas of atmospheric chemistry with general applicability. The utilizations of WRF-Chem includes, but is not limited to, air quality predictions (Kumar et al, 2019), future climate-chemistry projections (Kumar et al., 2018; Xu et al., 2020), meteorology-pollution interactions (Wu et al., 2019), Aerosol-cloud interactions (Feng and Ramanathan, 2010), atmospheric energy budget investigations (He et al., 2018), the characterization of biomass burnings (Grell et al., 2011) and examinations of regional visibility degradation (Durdina et al., 2017), etc.

One of the most important aspects of atmospheric chemistry simulations carried out by WRF-Chem is the proper selection of chemistry schemes. In WRF-Chem, chemistry schemes consist of multiple modules with different treatments of chemistry for three phases: gas, aerosol and aqueous phases (Grell et al., 2005 ； Galin et al., 2007). For each phase, the treatment and processing are represented by individual modules. Depending on the complexity of the desired simulation, one may choose a chemistry suite to contain all or part of the three phases' modules

(Barnard et al., 2010). For example, a simple aerosol-only module: Goddard Global Ozone Chemistry Aerosol Radiation and Transport (GOCART; Chin et al., 2000) may be simulated even without ozone chemistry in WRF-Chem (chem_opt=300) with only 18 chemical species tracked. In contrast, Model for Ozone and Related Tracers with Model for Simulating Aerosol Interactions and Chemistry (MOZART; Emmons et al., 2010) Chemistry with 8 sectional bins of Model for Simulating Aerosol Interactions and Chemistry (MOSAIC; Zaveri et al., 2008) suite (chem_opt=202), the most complicated chemistry set-up in the current WRF-Chem model, would involve modules from all three phases. Such a chemistry suite could track as many as 143 gas species and all major aerosols like sulfate, nitrate, ammonium, black carbon (BC), organic carbon (OC), etc. with more than 300 reactions (Emmons et al., 2010)

While more complicated model setups usually have better representations of real world air chemistry, the potentially expensive demands for computational resources may sometimes prohibit chemical parameterizations at ultra-high levels (Shrivastava et al., 2011). Therefore, tremendous amounts of effort have been made to simplify the chemical representations in global and regional models while maintaining certain levels of accuracy. For example, the Modal Aerosol Module (MAM) is a chemistry module that was originally developed for the Community Atmosphere Model version 5 (CAM5), the atmospheric component of the Community Earth System Model version 1 (CESM1; Liu et al., 2012). MAM is capable of treating major aerosol species including BC, OC, sulfates, sea salts, dust, etc. with a reasonable accuracy (e.g., $SO_4$ simulations; Liu et al., 2012) and computational cost.

In addition to the large domain concern, model spatial resolution could be another major issue to limit the complexity of chemistry modules (Emmerson and Evans, 2009). For climate-chemistry models, doubling the horizontal resolution leads to at least a factor of eight increase for

computational needs (Bey et al., 2001). Therefore, when focusing on a local feature with demands of high resolutions (e.g., convective clouds and terrain-complex domains), a regional model usually becomes the preferred choice over a global model (Gu et al., 2011). Moreover, for long-term simulations, testing the simulation set-ups with a regional model implementation ahead of a global one can not only be resource-saving but also time-efficient (Gan et al., 2015).

Although the application of modal or bulk aerosol approach in WRF-Chem can be dated back as early as 2004 (Peckham et al., 2017 and references therein), a version of the three lognormal modes of the MAM scheme (MAM3) was first implemented to WRF-Chem by Ma et al., (2014). Ma et al., (2014) adopted the CAM5 physics suite and transplanted the MAM3 module to WRF-Chem, called WRF-CAM5. However, studies utilizing such set-up are very limited and remain in the infantile stage. Studies utilizing the WRF-CAM5 set-ups have shown that in East Asia, there are consistently low biases for simulated chemical species and aerosol optical depth (AOD) against the observations (He et al., 2017; Zhang et al., 2015). Additionally, Ma et al., (2014) noticed that during the DC-8 flight campaign of boreal spring in 2008 in Alaska for Arctic Research of the Composition of the Troposphere from Aircraft and Satellites (ARCTAS), the observed BC could be 3 orders of magnitude higher than simulations. Ma et al., (2014) did not fully address this discrepancy but implied that the low model biases against observations were possibly related to the coarse simulation grid and showed improvements, albeit still two orders of magnitude off, with higher resolutions.

In the MBL, clouds are a crucial component of the Earth's energy budget while they remain as one of the largest uncertainties in climate simulations (Bony and Dufresne). Particularly, the presence of substantial MBL clouds off the California coast makes these clouds highly susceptible to the influences of continental aerosols (Painemal et al., 2015). In June 2013, A C-9 class ship,

serving as part of Marine ARM (Atmospheric Radiation Measurement) GPCI (Global Energy and Water Cycle Experiment (GEWEX)-Cloud System Study (GCSS)-Pacific Cross-section Intercomparison) Investigation of Clouds (MAGIC; Painemal et al., 2015) missions, made a round trip between Los Angeles, CA and Honolulu, HI. This MAGIC field campaign provides valuable data for model evaluations in this study.

Initial test runs using WRF-CAM5 indicate abnormally low aerosol concentrations and unrealistic spatial distributions particularly regarding the locations in the vicinity of biomass burning regions. This could be a consequence of an inconsistent implementation for the WRF-CAM5 model when compared to the CESM1 model (Liu et al., 2012; Ma et al., 2014). Therefore, in this study, we aim to improve the CBMZ-MAM3 chemistry modules in the current WRF-CAM5 model to address the following deficiencies:

(i) The biomass burning emission is completely ignored for both aerosol-phase (MAM3) and gas-phase (CBMZ) chemistry.

(ii) The mechanism that converts VOC to SOA is not included.

We describe the model set-ups and modifications in Section 2. We compare the original and enhanced simulation results against various benchmarks, including surface observations, satellite observations, and reanalysis products in Section 3. The aforementioned modifications and improvement are presented in a progressive manner in the following sections to understand the role of different implementations.

## 4.2 Methods

### 4.2.1 WRF-CAM5 model

We use version 3.9.1.1 of the WRF model (Skamarock et al., 2008) coupled with Chemistry (Fast et al., 2006; Grell et al., 2005) with CAM5 for the physics mechanism and CBMZ and MAM3 for gas- and aerosol-phase chemical mechanisms, respectively, in this study (referred to as WRF-CAM5 hereafter). The simulation domain spans from 180°-93°W and 9°-55°N (Figure 20) with 27 vertical layers up to 100 hPa. The horizontal grid spacing is uniformly defined to 36 km × 36 km. The surface processes are simulated by the unified NOAH land surface model (Tewariet al., 2004). The 1-month simulation period spans from June 1st, 2013 to June 30th, 2013 were used for model assessment, which covers the observational periods of the MAGIC campaign. The meteorological initial and boundary conditions were from the 6-hourly National Centers for Environmental Prediction Final Analysis (NCEP-FNL; NCEP, 2000) and the simulated meteorology was nudged to NCEP-FNL every 6 hours. Chemical initial and boundary conditions are from the global simulations of the Community Atmosphere Model with Chemistry, version 5 (Lamarque et al., 2012). Longwave and shortwave radiation processes are parameterized by applying Rapid Radiative Transfer Model developed for General Circulation Models (RRTMG; Iacono et al., 2008).

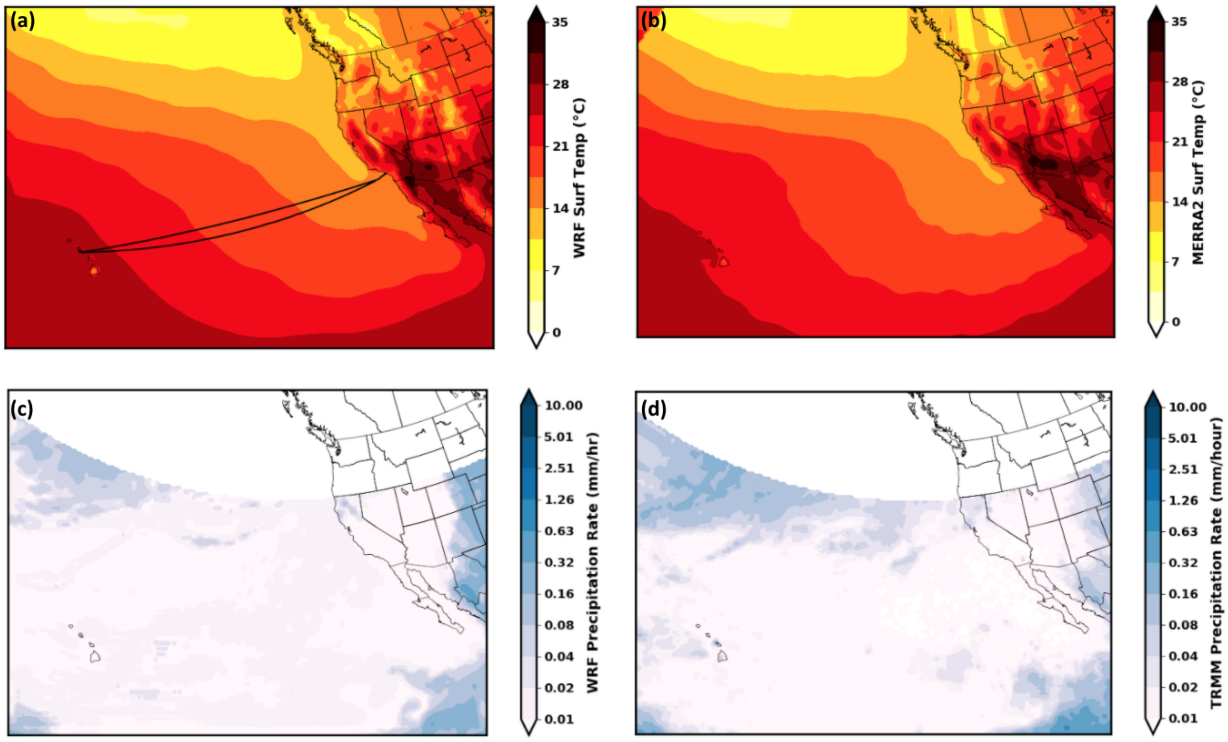


Figure 20. Surface temperature in (a) WRF-Chem simulation and (b) MERRA2 product. Ship track of the MAGIC campaign is shown in panel (a). The map shows the entire domain of the simulation. Precipitation in (c) WRF-Chem simulation and (d) TRMM observation. The white areas from WRF-Chem simulations are due to truncation to match TRMM latitude coverage. Note that the color bars are in log scales.

### 4.2.2 Chemistry configurations: CBMZ-MAM3 (for enhancement) and MOZART-MOSAIC

MAM has two versions: MAM3 and MAM7. In this study we use MAM3, which is specifically designated for computational demanding simulations. MAM3 is an aerosol module that has been widely applied in global models (e.g., CAM5; Liu et al., 2012; Xiao et al., 2014; Gantt 2014) for its economical computational cost (Liu et al., 2012). MAM3 simulates major aerosol species like: BC, OC, dust, sulfates, sea salts but without nitrate chemistry. In WRF-

CAM5, the MAM3 is frequently linked with CBMZ gas chemistry (Peckham et al., 2017) and such combination is defined as chemistry option 503 in simulation set-ups.

We run simulations with two suites of gas-phase and aerosol phase chemistry: CBMZ-MAM3 (Zaveri and Peters, 1999; Liu et al., 2012) and MOZART-MOSAIC) (Emmons et al., 2010; Zaveri et al., 2008). The former one is the one we strive to improve in WRF-CAM5 as a workable configuration for reasons described in the Introduction, while the latter one is the most comprehensive and expensive chemistry scheme in WRF-Chem, serving as a benchmark. Ideally, we want to use the same physical schemes for the two simulations to isolate the chemistry impact, but this will result in chemistry-physics compatibility issues that either cause model syntax errors or yield unrealistic simulation results.

Table 13 summarizes the details of key differences between the two chemistry configurations. For the CBMZ-MAM3 simulation, the planetary boundary layer (PBL) processes are parameterized by using University of Washington shallow convection and moist turbulence schemes (Park and Bretherton, 2009); while for MOZART-MOSAIC simulation, the PBL scheme is chosen to be Yonsei University (YSU) PBL scheme (Hong et al., 2006). We use different PBL schemes because the MAM3 chemistry module requires the CAM5 PBL scheme while such a scheme is not compatible with MOZART-MOSAIC setups. For cloud microphysics schemes, the CBMZ-MAM3 simulation uses the CAM5 Morrison-Gettleman scheme (Morrison et al., 2009) and MOZART-MOSAIC simulation adopts scale-resolved cloud physics representation by Morrison two-moment scheme (Morrison et al., 2009). In addition, the photolysis schemes of trace gases in WRF-CAM5 are set differently for two suites, by default. The CBMZ-MAM3 suite is coupled with Fast-J photolysis (Wild et al., 2000) and the most ideal photolysis option for MOZART-MOSAIC simulation is Fast Troposphere Ultraviolet Visible (Tie et al., 2005).

Table 13. Different physical and chemical schemes used in the CBMZ-MAM3 and MOZART-MOSAIC simulations.

| | WRF-CAM5 with CBMZ-MAM3 | WRF-Chem with MOZART-MOSAIC |
|---|---|---|
| Chemistry | CBMZ | MOZART |
| Aerosol | MAM3 | MOSAIC (4-bins) |
| Photolysis | Fast-J | Madronich F-TUV |
| Emission | RADM2 gas emissions to CBMZ with MAM 3 aerosols | MOZART + aerosols emissions |
| Microphysics | CAM5: Morrison and Gettleman | Morrison double-moment |
| Cumulus | CAM5: Zhang-McFarlane | Grell-Freitas |
| PBL | CAM5: Univeristy of Washington | Yonsei University |

MOSAIC simulates most major aerosol species like BC, sulfate, ammonium, OC, nitrate, sodium, chloride (Cl) with 4 or 8 size bins. This study uses the 4-bin version. The MOZART-MOSAIC suite is considered to be more chemically sophisticated because it involves 143 gas-phase species with 347 reactions, while CBMZ-MAM3 uses the bulk mechanism and approaches the detailed chemical species in lumped-group mechanism (Liu et al., 2012). Therefore, we would

expect more realistic simulation results from the MOZART-MOSAIC benchmark given its more comprehensive representation of chemical processes.

### 4.2.3 Emissions

For anthropogenic emissions, we use the United States Environmental Protection Agency (EPA) National Emissions Inventory (EPA-NEI). Then, we patch the NEI emissions with the version 2 of the Emission Database for Global Atmospheric Research (Janssens-Maenhout et al., 2015) developed as a part of Hemispheric Transport of Air Pollution (EDGAR-HTAP v2) project to update continental US emissions. EPA-NEI has a spatial resolution of 12 km and EDGAR-HTAP has a spatial resolution of 1° × 1°. Both datasets are regridded to match with simulation domains. We conduct patching because we have higher confidence in EPA products over the continental US, while a portion of our simulation domain is outside the EPA boundaries (e.g., the emissions from Hawaii) requiring the global emission dataset.

For EPA's emissions, the latest NEI inventory is for the year 2014 (1-year difference from our simulation year). For EDGAR, the latest emissions are for the year 2010 (3-year difference). EPA distinguishes the emissions by weekdays and weekends assuming weekday emissions are stronger in urban areas compared to the weekends (Janssens-Maenhout et al., 2015). A weekday in 2014 could be a weekend in 2013 and vice versa. Therefore, we conduct the calendar adjustment and make sure the emissions follow the 2013 weekday and weekend patterns. We map the EPA-NEI emissions to the WRF-CAM5 model grids by utilizing the Sparse Matrix Operator Kernel (SMOKE) Modeling System to yield hourly anthropogenic emission input data. The EDGAR emissions are for diurnal cycles only (hour 0 UTC to 23 UTC) without weekday-weekend discrimination and therefore, do not require an adjustment as above.

For biomass burning emissions, we use the Fire Inventory from NCAR (FINN; Wiedinmyer et al., 2011), a widely-used satellite-based fire detection inventory with a horizontal resolution of 1 km. For biogenic emissions, we use the Model of Emissions of Gases and Aerosols from Nature (MEGAN; Guenther et al., 2006), which is affected by environmental conditions.
In addition, we also perform a sensitivity simulation by enhancing the aerosol and VOC emissions by three times. The simulation is implemented by adding a scaling factor to the emission module and therefore boosting the read-in inventory values by three-fold.

### 4.2.4 Data for model assessment

#### 4.2.4.1 MERRA2 Reanalysis Product

Accurate model simulations are critical for representations of any physical or chemical processes. Therefore, we use the Modern-Era Retrospective analysis for Research and Applications, Version 2 (MERRA2, Gelaro et al., 2017) for simulation validations of meteorology, chemical species and AOD. Although the MERRA2 should not be trusted as a truth, it has been tested for its acceptable authenticity in our study domain (Randles et al., 2017; Reichle et al., 2017). MERRA2 has a relatively comprehensive variable category, allowing us to evaluate both meteorological and chemical variables. MERRA2 archives the results from 1980 onward and we use monthly data of June 2013 for evaluation. Since reanalysis products are spatially gridded, utilizing the MERRA2 product enables us to conduct model validations for large-scale spatial patterns.

#### 4.2.4.2 Ground observations from EPA, IMPROVE, AERONET

In addition to the reanalysis product, we also validate both meteorology and chemistry against ground-based observations. For both surface temperature and CO mixing ratios, we use EPA Air Quality System (AQS) for validations (EPA, 2017) as EPA AQS has both meteorological and chemical data in archive. AQS has been extensively applied for both meteorological and chemical validations in our study domain (e.g., Dury et al., 2010; Kharol et al., 2017; Zhang et al., 2018) and therefore, we select six urban areas within the domain for model evaluation, including Irvine, CA, San Diego, CA, Salt Lake City, UT, Denver, CO, Seattle, WA and Phoenix, AZ. These sites are all within the simulation domain (western part of the US) with large amount of populations (>300,000). In addition, they are spatially separated and therefore ideally for testing the validity of model performances in different regions.

The simulated AOD results are compared to the Aerosol Robotic Network (AERONET; Holben et al., 1998) by the National Aeronautics and Space Administration (NASA). AERONET is a ground-based remote sensing aerosol network using Sun- and sky-scanning radiometers to measure aerosol optical properties (Dubovik and King, 2000). Similar to the EPA AQS sites, we select six AERONET sites within the simulation domain for model evaluation, including CalTech, CA, Santa Monica, CA, Kelowna, BC, White Sands, NM, Hermosillo and Neon-Civalla, CO.

Finally, the simulated surface BC and OC concentrations are compared to the Interagency Monitoring of Protected Visual Environments (IMPROVE) network. The IMPROVE network primarily measures the elementary carbon and OC at national parks and national monuments (Chow and Watson, 2002). Like EPA AQS and AERONET sites, we select six IMPROVE network sites for model evaluation, including Phoenix, AZ, Fresno, CA, Puget Sound, WA, Lava Beds, CA, Great Basin, NV and San Rafel, CA.

#### 4.2.4.3 Satellites Observations

Apart from ground-based observations, we also include the satellite products for further validations due to their broad spatial coverages. For precipitation, we compare the simulated results with the daily total accumulated precipitation products from Tropical Rainfall Monitoring Mission (TRMM; Adler et al., 2000). The performance of TRMM has been extensively examined in North America with relatively reliable results (Yamamoto et al., 2008). Since the WRF-CAM5 simulation treats the precipitation in an accumulation manner, the final results are shown in a unit of the monthly total. We convert the precipitation from both TRMM product and simulation results to hourly fluxes for comparisons.

For AOD validations over the ocean, we use the state-of-art Cloud-Aerosol Lidar and Infrared Pathfinder Satellite Observations (CALIPSO) retrievals (Painemal et al., 2019). Using CALIPSO for validations over the ocean is a widely adopted approach (Lu et al., 2014). CALIPSO has a relatively narrow swath (~ 60 km) because the beam is directed at a fixed angle near nadir and therefore may only cover 1-2 grid cells at one time step. In this study we compare the CALIPSO retrieval to the closest simulation grid for each time-step and take the average on a daily basis. We then show the comparison between WRF-CAM5 simulated AOD and CALIPSO retrieved results.

#### 4.2.4.4 MAGIC Ship Campaign

In addition to ground-based observations and satellite retrievals, the MAGIC ship campaign (Painemal et al., 2015) serves as a supplemental data source for observations over the ocean. In June 2013, a campaign vessel made a round trip between Los Angeles, CA and Honolulu,

HI (Figure 20a). In this study, we use the observations of surface temperature and AOD from the MAGIC campaign to evaluate our simulations over the East Pacific. The temperature data of the MAGIC campaign was collected every 1 minute while the AOD data were collected intermittently without specific temporal range. To match the simulation in time, the surface temperature data are taken for hourly averages and AOD data are taken for daily averages.

For summarized and detailed data sources and variables used for model assessment in this study, readers are referred to Table 14.

Table 14. The source of observations used for validations.

| Data sources | Variables |
|---|---|
| Aerosol Robotic Network (AERONET) | AOD |
| Interagency Monitoring of Protected Visual Environments (IMPROVE) | surface concentrations of BC and OC |
| Environmental Protection Agency (EPA) | surface temperature;<br>surface concentration of CO |
| The Modern-Era Retrospective analysis for Research and Applications, Version 2 (MERRA2) | surface temperature;<br>surface concentration of BC, CO, OC;<br>AOD |
| Tropical Rainfall Measuring Mission (TRMM) | precipitation |
| Cloud-Aerosol Lidar and Infrared Pathfinder Satellite Observations (CALIPSO) | AOD |
| MAGIC ship campaign for 2013 June | surface temperature, AOD |

### 4.3 Model Enhancements

We make enhancements to two major WRF-CAM5 modules: MAM3 and CBMZ to mitigate the two deficiencies (i.e., missing biomass burning emission processes in both MAM3 and CBMZ, and missing VOC-to-SOA conversion mechanisms). In this study, we solve these two issues by focusing on the emission part first and implement the VOC conversion process afterward.

Therefore, we perform 6 sets of simulations in total with 4 progressively showing model improvements; one simulation adopts the increased emissions; one benchmark run with the more sophisticated MOZART-MOSAIC chemistry suites. All simulations use the same chemical and meteorological initial and boundary conditions. Specifically, these all simulations are summarized as:

(a) the basic run with original WRF-CAM5 setups (Baseline).

(b) Including the capability of ingesting biomass burning emissions of aerosols in MAM3 (AddingBBaerosol).

(c) In addition to (b), including the capability of ingesting biomass burning emissions of gaseous species in CBMZ (AddingBBgas).

(d) In addition to (b) and (c), including conversion mechanisms from VOCs to SOAs through an intermediate product called SOAG (SOA gas; see Section 3.2 for details) (AddingSOA).

(e) In addition to (b), (c), and (d), increasing biomass burning emissions by 3 times from the inventory (TriplingEmission).

(f) A benchmark run with the MOZART-MOSAIC chemistry suite (MOZART-MOSAIC).

### 4.3.1 Enhancements to Ingest Biomass Burning Emissions in CBMZ-MAM3

Adding the capability of ingesting biomass burning emissions in the CBMZ-MAM3 chemistry suite involves supplying the emitted species to these two modules separately. The first step is to add emitted aerosol phase species to the MAM3 module. We add three major biomass burning emitted aerosols, including BC, Primary OC (POC), and sulfate, to the MAM3 read-in

module. MAM3 partitions the aerosols into three-modes: Aitken, Accumulation, and Coarse. In this modification, we add all species to accumulation mode for simplicity. By default, the BC and OC should primarily be read into the accumulation mode (Liu et al., 2012) while sulfate could exist in all three modes. We add all species to accumulation mode because this is the most dominant mode.

Next, we add gas-phase biomass burning emitted chemical species to the CBMZ module. The following primarily emitted gas species are added: $SO_2$, $NO_2$, NO, $NH_3$, CO, $CH_3COCHO$, $CH_3OH$, $C_2H_5OH$, $C_5H_6O_2$. Among all species listed, $SO_2$ has the oxidation mechanism to produce aerosol phase product (e.g., sulfate) while for NOx species (NO and $NO_2$), such a mechanism is not possible because MAM3, by default, does not have the nitrate chemistry mechanism integrated (Liu et al., 2012).

### 4.3.2 Enhancements to Allow VOC to SOA Conversion

Apart from missing biomass burning emissions, another major issue with the current MAM3 module in WRF-CAM5 is the failure of simulating SOA. SOA may consist of more than 50% of total aerosols in certain areas (Kanakidou et al., 2005) and previous observations have indicated a dominant role of secondary originated sources for total organic matters (Tsigaridis and Kanakidou 2007). SOA is primarily formed by oxidation of various VOCs (Camredon et al., 2007). This poses an inherent challenge for numerical modeling due to a large amount of VOC types ($> 10^3$ ; Park et al., 2013). Therefore, a more applicable approach is to group VOCs either by molecules or structures (Middleton et al., 1990). However, both approaches can still be computationally demanding depending on the number of groups simulated by the model, and the

complexity of SOA-related chemistry one may desire to simulate. Built to accommodate global models, MAM3 picked a simplified and less costly pathway.

MAM3 treats the formation of SOA in a bulk mechanism from a predefined intermediate variable called SOAG (SOA gas; Liu et al., 2012). SOAG is calculated from summing up VOCs by groups (alkanes, toluene, isoprene, etc.) and assign individual yielding factors to each specific species (Liu et al., 2012), describe in the equation below

$$SOAG = \sum_{i=1}^{n} C_{VOC_i} * yield_i$$

where $C_{VOC_i}$ is the concentration of individual VOC species in parts per billion (ppb) that converts to SOAG and $yield_i$is the corresponding empirically determined yielding factors. The typical range for yielding factors are between 5% to 25% (Liu et al., 2012).

To accomplish this task, we follow Liu et al., (2012) to add six groups of VOC species and the intermediate variable (SOAG) to the MAM3 module. These added VOC species are big alkanes, big alkenes, isoprene, toluene, monoterpenes, hydroxyacetone (a.k.a. acetol). Among these six groups of species, the first five species are defined in Liu et al., (2012), while the last species (hydroxyacetone) is further added in this study. Adding such species can significantly improve the simulation results as we examine the FINN inventory, hydroxyacetone is the dominant species among all emitted VOCs. In fact, the hydroxyacetone's contributions towards SOA formation have been documented by several previous studies (e.g., Zhou et al., 2018; Fu et al., 2008).

For yielding factors, all species are assumed to be 15% except for isoprene and monoterpenes, which were assumed to be 4% (Kroll et al., 2006) and 25% (Ng et al., 2007), respectively. The yielding factors for big alkanes and big alkenes here are higher than the values

(5%) used in Liu et al., (2012). However, we found a better model performance by using higher-yielding values instead of lower ones (e.g., 5%). Moreover, the adoption of 5% yielding factors for big alkenes species was also empirically assumed in Liu et al., (2012).

### 4.3.3 Modifications to Enhance Emissions

For the final modification, we conduct the sensitivity test for emission enhancements after two major modifications are completed above. For the emission enhancement, we define a new emission scaling factor in the MAM3 module and multiply it with the ingested emissions from the inventories. Then the updated emissions are passed to any subsequent modules.

### 4.3.4 Modifications to Other Related Modules

In addition to the two chemistry modules modified above, we have edited other accompanying modules that use either these modules or their output variables for further processing. There are three additional modules serving these purposes (Figure 21), including the chemistry driver module, the emission driver module, and the plume rise module. For the chemistry driver and emission driver modules, the required modifications are to add newly incorporated variables from biomass burning emissions, pass these variables to the two chemistry modules, and additionally define and compute a new species variable for SOAG.

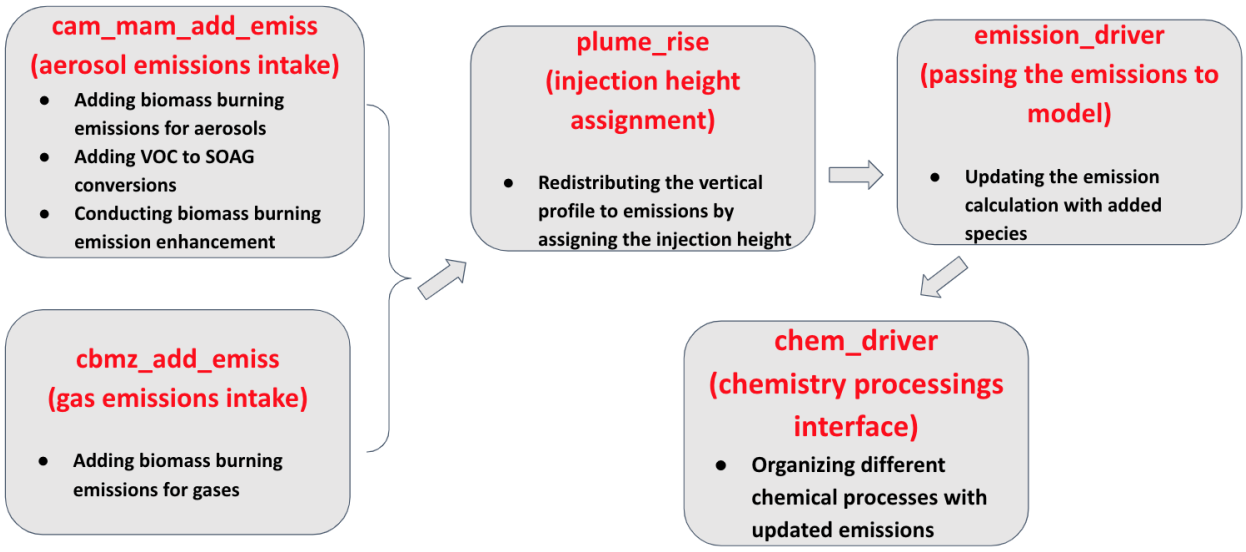


Figure 21. Schematics of model modules. Brackets indicate that these two steps are implemented in parallel. Arrows indicate the proceeding orders (i.e., later steps require inputs from previous steps). Black bullet points are modification/contribution done in this study.

For the plume rise module, additional adjustments are necessary. The first step is to identify the number of emission levels from inventories. In this case, FINN assumes the emissions all originated from the surface and the level is therefore set to 1. Then, we pass each emitted species to the vertical redistribution section where the module extracts the read-in emissions, stretching it vertically and assigning designated injection heights for each of the species based on the fire intensity. Figure 21 shows a schematic of module relationships and processing steps.

Aside from all modules modified above, we need to define all simulated species in the registry of WRF-CAM5. The CBMZ-MAM3 module was coupled to WRF-CAM5 using the second generation Regional Acid Deposition Model (RADM2; Stockwell et al., 1990) and such emission conversion option was defined as option 9 in WRF-CAM5. However, the current WRF-CAM5 version (3.9.1.1) does not have exhaustive VOC species listed in the registry. Changing the

chemistry modules alone without editing the registry would result in a significant underestimation of the total simulated SOA, since the model ignores the major VOC species we added to the MAM3 module. . Thus, we add all the aforementioned but currently unlisted VOC species to the chemistry registry and align all species names to be consistent with the input inventory. Accordingly, the MAM3 chemistry module would be able to recognize the added species and process them successfully.

## 4.4 Results

### 4.4.1 Validation of Meteorology

We first validate the simulated meteorology. Figure 20 compares the spatial distribution of monthly averaged surface temperature and precipitation from WRF-CAM5 simulations during June 2013. When compared to the MERRA2 products, the simulated temperatures are consistent with MERRA2 results with a mean bias of -1.7 K. For surface temperature, the WRF-CAM5 simulation successfully identifies the hot regions inland (near Arizona and Baja California). Also, the magnitude of temperature is highly consistent with the MERRA2. For precipitation, TRMM identifies the Central Pacific and East Pacific at tropics as regions with strong precipitation. Both regions are captured by the WRF-CAM5 model. For inland areas, the simulation agrees with TRMM in that Colorado and New Mexico are states with heavy precipitations. Therefore, we conclude that the simulated precipitation has a decent agreement with the TRMM observations.

For surface temperatures, we also evaluated the simulations against observations from six cities (Figure 22). All six cities witness highly consistent values between the simulated results and observed ones. The simulated results have 0-4 K cold biases for all sites. Nonetheless, for the period simulated, no days fall out of the error bars. The results here indicate that the model

simulations are highly consistent with the observations for temperature. In addition, we also evaluated the simulated temperature against the MAGIC Campaign (Figure 23), the simulated results are highly consistent with the ship observations. For each observational time-step, the ship observed surface temperature is within 1 K of our simulation. The small model error indicates that the meteorology simulations are reliable.

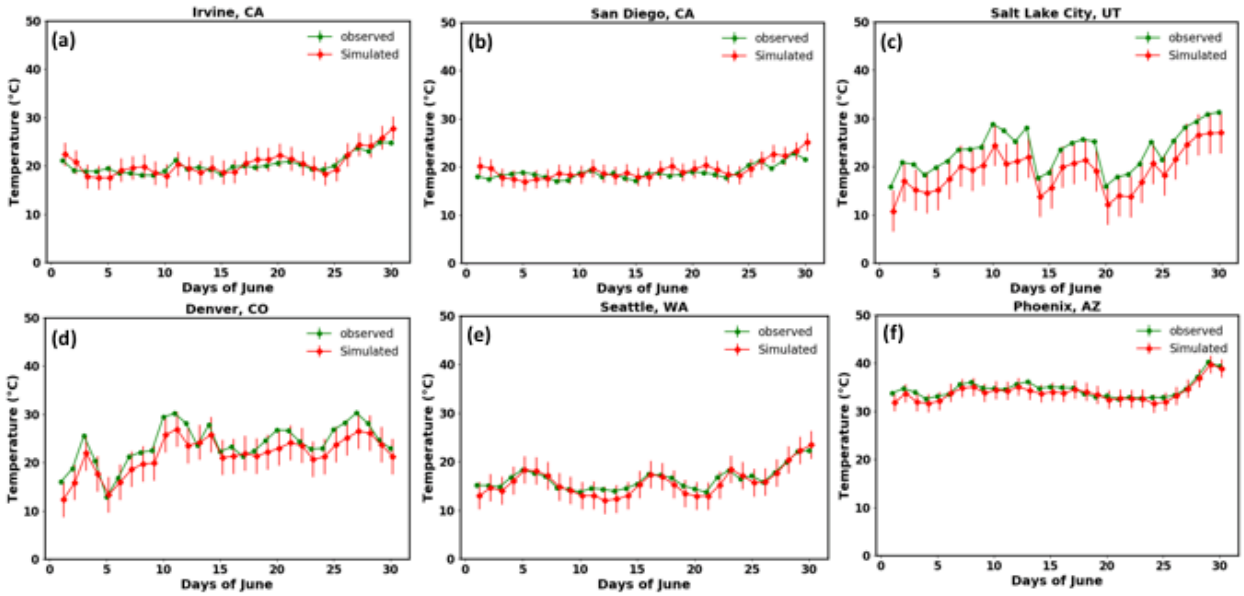


Figure 22. Temperature over six cities (as in panel subtitles). Observations from EPA Air Data are shown in green, and WRF-Chem simulations are shown in red. Error bars are one standard deviation of day-to-day variability for the entire month.

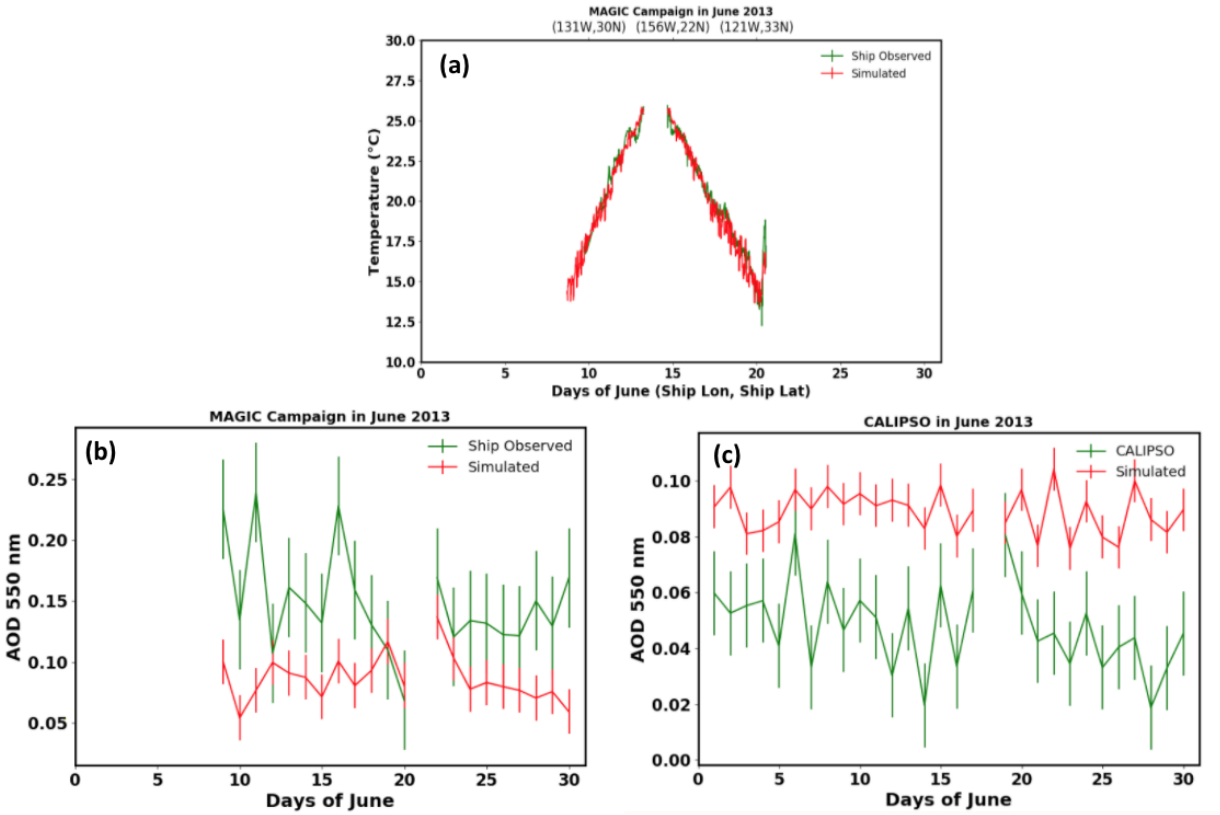


Figure 23. Validations from MAGIC campaign and CALIPSO in June 2013. (a) Surface temperature validation from MAGIC Campaign. (b) AOD validation from MAGIC Campaign and (c) AOD validation from CALIPSO. Error bars are one standard deviation of day-to-day variability for the entire month

### 4.4.2 Validation and Progressive Improvement of the Chemical Fields due to Model Enhancements

#### 4.4.2.1 Improvement of AOD

Here, we show the validation of chemical species along with the demonstration of step-wise model improvements. We first evaluated the simulated AOD at 550 nm against both the reanalysis product and station-wise observations. Generally, the later implemented runs have higher AOD levels compared to the previous ones (Figure 24). The AOD improvement after

adding the biomass burning emissions of aerosols (AddingBBaerosol) was rather trivial in the US, which cannot capture the hotspots shown in MERRA2 products. Instead, the major improvement in this case comes from the Mexico regions. After enabling VOC to SOA conversions (AddingSOA), the spatial pattern in the US side becomes more consistent with MERRA2. However, the magnitude is much smaller than the MERRA2 products (by roughly a factor of 2). Therefore, we further investigate the progress by comparing MERRA2 products with a tripled emission run (TriplingEmission). We find a much smaller model bias under this scenario for both US and Mexican regions. Almost all hotspots shown in MERRA2 are captured by the model simulation, however, the magnitudes at different hotspots are still inconsistent between the model and MERRA2 as MERRA2 has one dominated high AOD region in New Mexico areas. Nonetheless, we do see the progressive advancement of the model after the step-by-step chemistry enhancements.

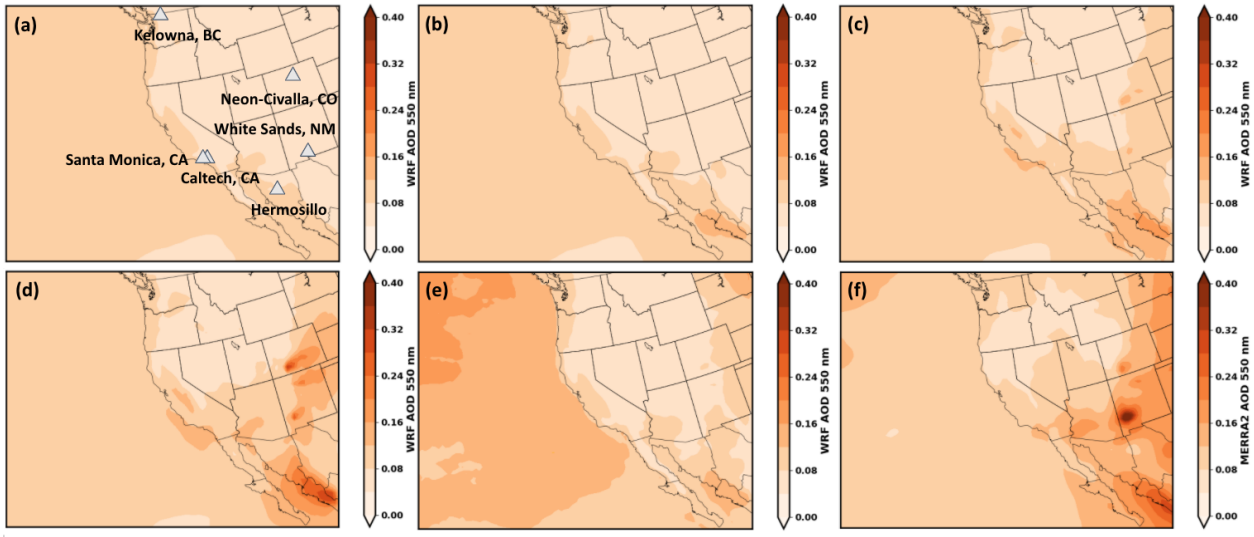


Figure 24. AOD at 550 nm from (a) Baseline, (b) AddingBBaerosol, (c) AddingSOA, (d) TriplingEmission, (e) MOZART-MOSAIC and (f) MERRA2 products.

We also evaluated the AOD against the AERONET observations (Figure 25). Overall, the AERONET observations have higher AOD even compared to the TriplingEmission, the run with the highest simulated AOD, except for a very short period of time in each station (e.g., June 11th at Caltech Station). However, we can clearly identify the gradual progress after each implementation as the biases become increasingly smaller (from -0.07 to -0.02). Such changes and biases are consistent with the results found in the MERRA2 products. Among all stations, the White Sands Station has the most distinctive improvements and is considered to have the best performance among them. The TriplingEmission simulation tracks the observations very well (mean bias of -0.02) for most days in June except for the last few days. Although the simulated AOD levels are generally lower than observations, the simulations have decent performances for some stations (e.g., Santa Monica and Kelowna) but have large biases in others (e.g., CalTech and Hermosillo). Thus, we conclude that the stepwise implementations reduce the biases and shall be considered acceptable for error reductions.

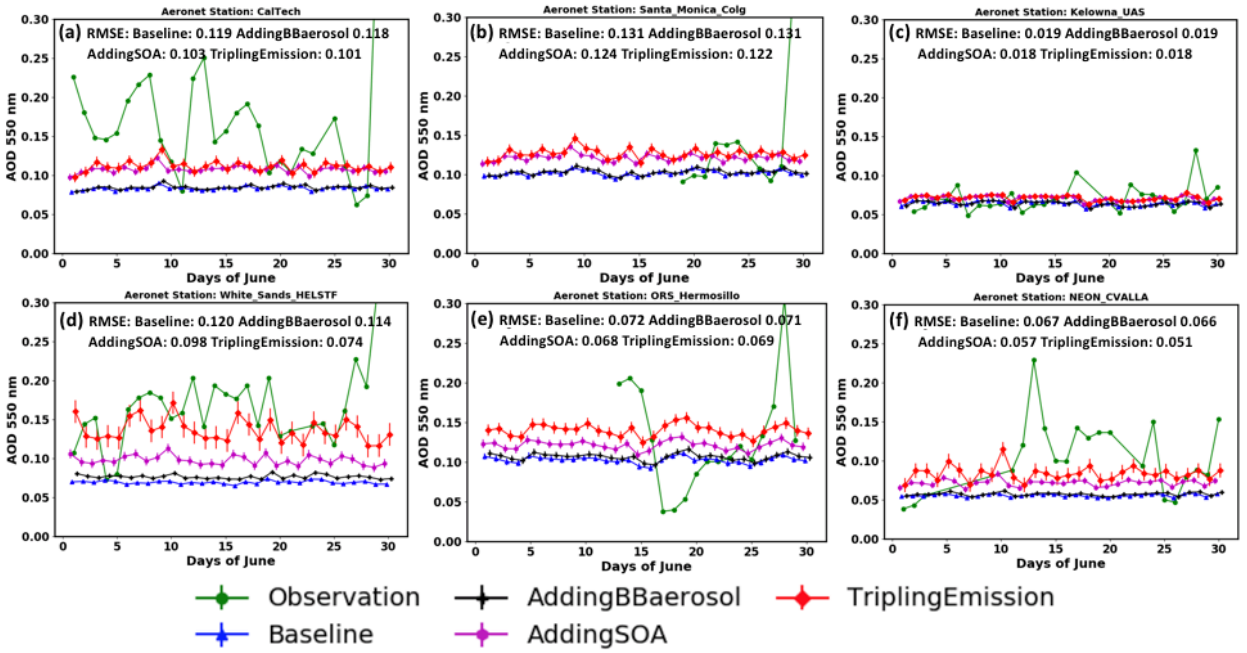


Figure 25. AOD at 550 nm for six stations (as described in panel titles, locations shown in Figure 24a). Green lines are observations from AERONET stations. Blue lines are the Baseline; black lines are the AddingBBaerosol; magenta lines are AddingSOA and red lines are TriplingEmission. Red error bars are one standard deviation of day to day variability for the entire month for TriplingEmission.

The performance of simulated AOD over the ocean is worse than the AOD inland. In Figure 23, we compared the TriplingEmission AOD with both the MAGIC campaign and CALIPSO retrievals over the East Pacific. For the MAGIC campaign, the simulated AOD has consistently low biases between -0.02 to -0.17 and about half of the total observed days are within the range of uncertainties. In contrast, when comparing against the CALIPSO retrieval, our simulated results are consistently showing positive biases ranging from 0.01 to 0.07. For the majority of the period, the simulation results fall outside of the uncertainties except for one day (June 19). The inconsistent biases between simulations and benchmarks indicate that the improved WRF-CAM5 is less capable of producing accurate results over the ocean than land. This is likely because the AOD

over oceans are mainly controlled by sea salt productions and aerosol transport from continental source regions, which are not strongly affected by the several model enhancements made in this study.

#### 4.4.2.2 Improvement of BC and CO

In addition to AOD, we also evaluated individual species. Figure 26 shows one-month averaged surface BC concentrations from each model modification comparing with MERRA2. For BC, the Baseline simulation completely misses the hotspots shown in MERRA2 with only slight plume footprints found near Los Angeles metropolitan area. After enabling the biomass burning emissions of aerosols (AddingBBaerosol), the spatial distribution of BC shows more consistent patterns compared to the MERRA2 results with a reduced bias from -0.3 to -0.1. Such improvement is furthered by TriplingEmission. Under this scenario, the simulated BC is comparable with MERRA2 results with only some overestimation of BC concentrations in Mexico. Such discrepancy could be attributed to the different intensities of biomass burning emissions in the US and Mexico considered in the model and reanalysis product.

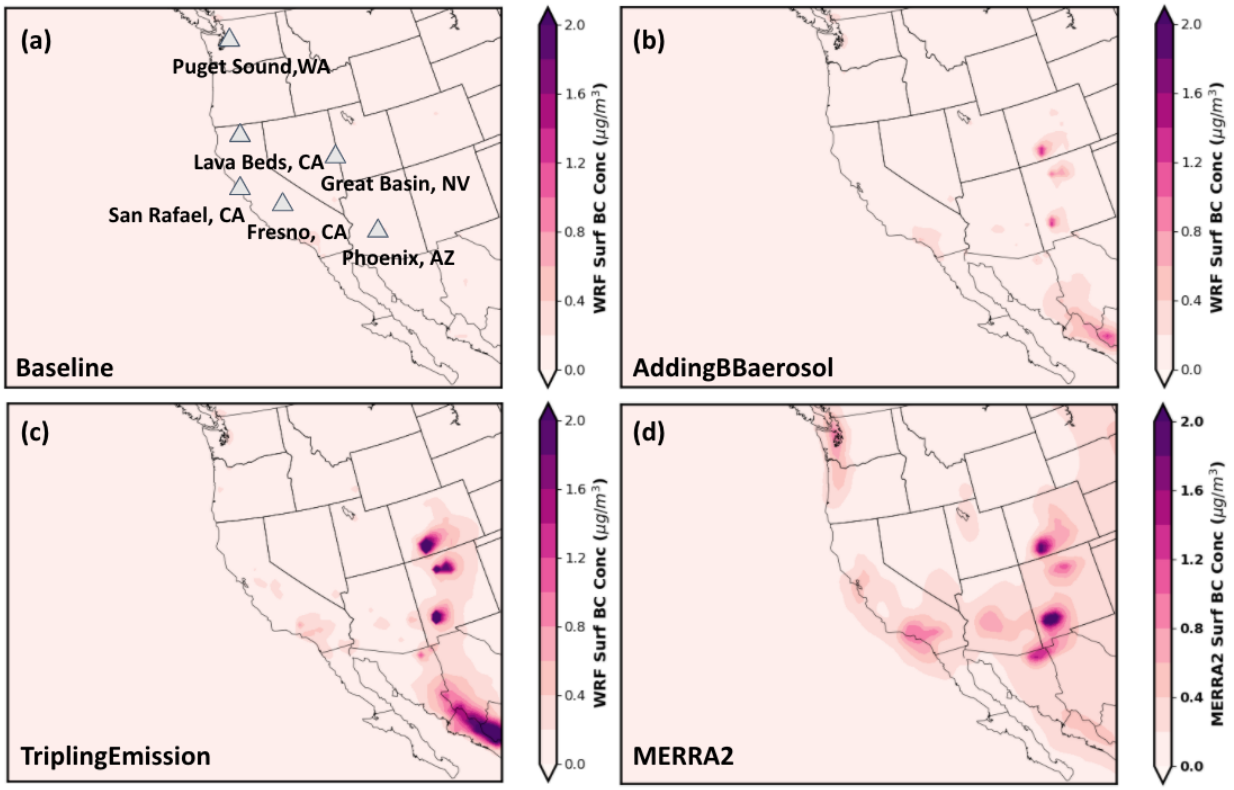


Figure 26. Surface BC concentrations from (a) Baseline, (b) AddingBBaerosol, (c) TriplingEmission (d) MERRA2 product.

Figure 27 shows the station-wise comparison between the simulated and observed surface BC concentrations at six IMPROVE sites. Generally, the observed BC is higher than the simulated values, especially for the Baseline simulation. Further chemistry and emission enhancements help mitigate the gap between the observations and simulated results. For most observed daily BC values, they are within the range of uncertainty of simulation, indicating that our simulation performs decently in most of the sites. Puget Sound, WA is the only site that the simulation failed to capture the observations. The large day-to-day variability is beyond the range and uncertainty of model results albeit witnessing some large values are closer to the improved/emission enhanced.

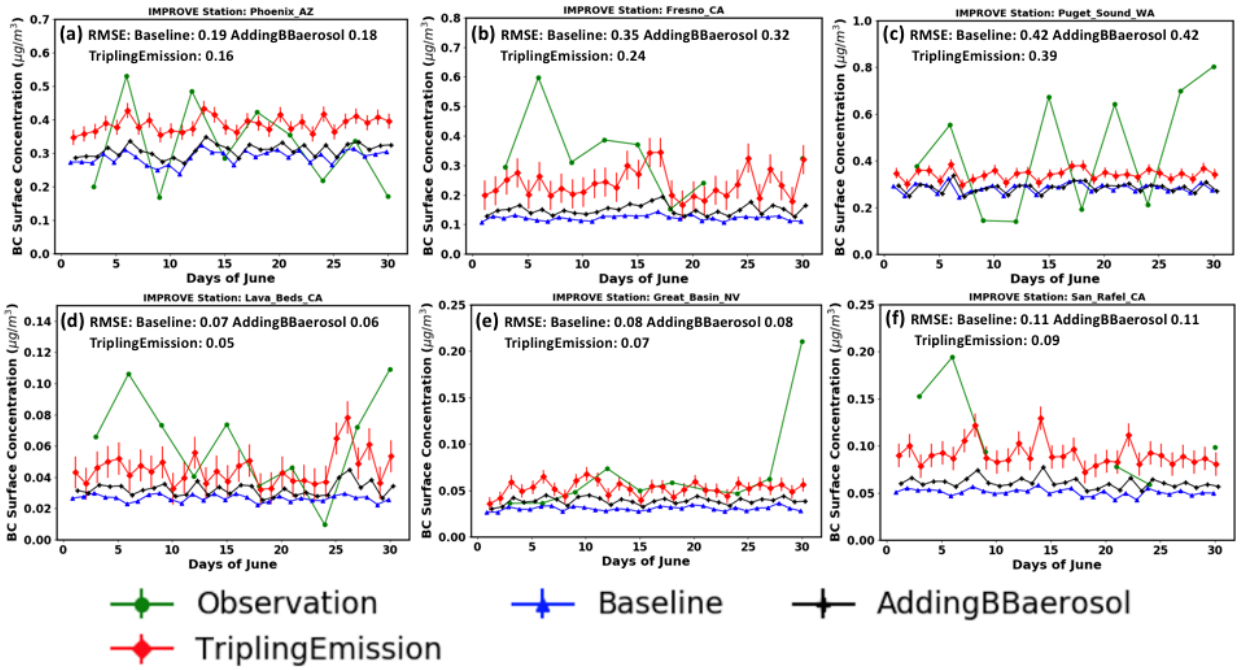


Figure 27. BC surface concentration for six stations (as described in panel titles, locations shown in Figure 27a). Green lines are observations from IMPROVE stations. Blue lines are the Baseline simulation; black lines are AddingBBaerosol and red lines are TriplingEmission. Red error bars are one standard deviation of day-to-day variability for the entire month for TriplingEmission.

For primarily emitted chemicals, we also made modifications to gas-phase species. Such improvement is documented in Figure 28 using CO as an example. In Figure 28, the biomass burning emitted CO begins to show up in the state of New Mexico as well as the southwestern part of Colorado. These hotspots of high CO mixing ratios coincide with the hotspots of high BC concentrations shown in Figure 26, implying that biomass burning dominates the contributions of these species in these areas. After adding biomass burning emissions of gas species, the spatial pattern of CO mixing ratios becomes closer to MERRA2 products shown in panel c. For surface observations of CO, we compared the daily mixing ratios against the observations (Figure 29) at the same sites as we did for temperature. For Irvine, CA, and Seattle, WA, the simulated CO

mixing ratios match observations very well. The results are less accurate in Salt Lake City, UT, and Phoenix, AZ. Simulated levels suffer 0.1 to 0.2 low biases in these two cities when compared against the observations. However, the daily results in both cities are within the range of observational uncertainties and shall be considered doing reasonably well. For the remaining two cities, San Diego, CA and Denver, CO, the simulated results were rather poor. The low biases are generally between 0.2 and 0.3. Most importantly, the model results in these cities are beyond the observational uncertainties for most of the days, especially for San Diego. Nonetheless, for most of the sites, the simulated CO mixing ratios are reasonable and trustworthy.

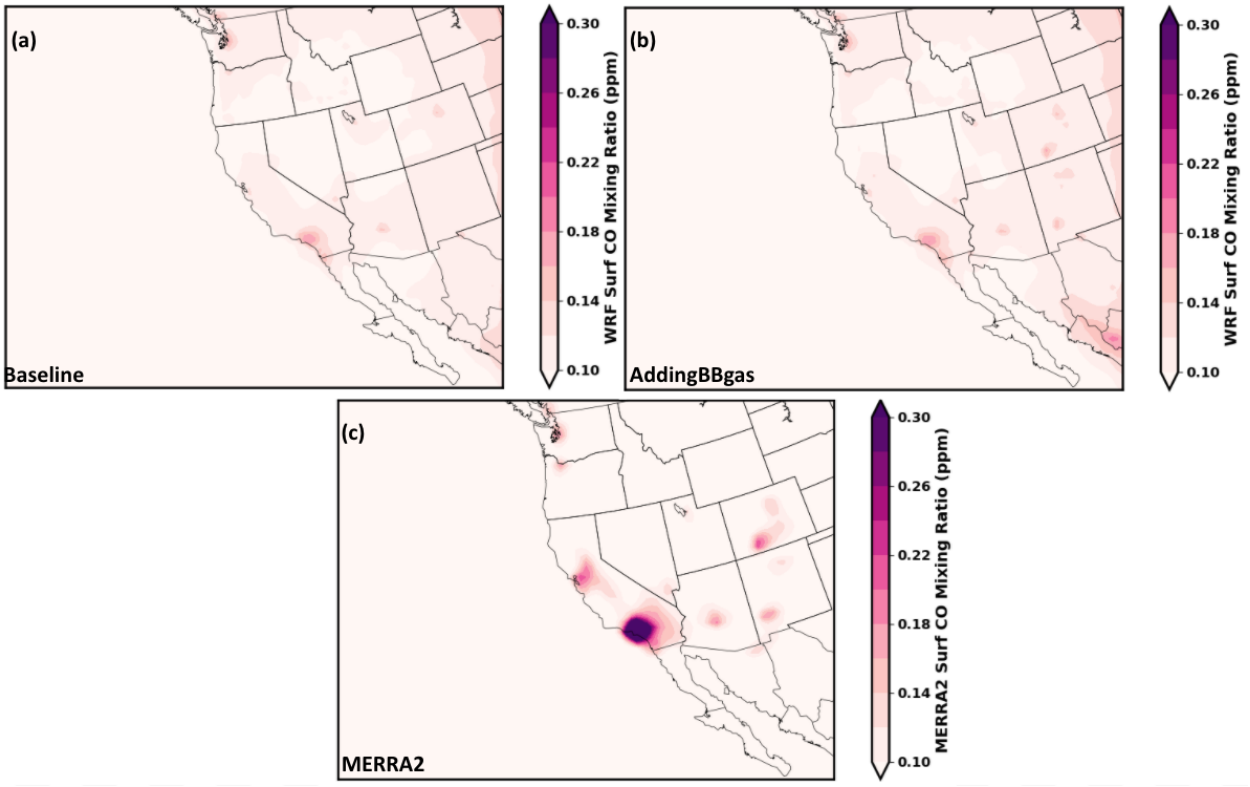


Figure 28. Surface CO mixing ratios from (a) Baseline, (b) AddingBBgas and (c) MERRA2 products.

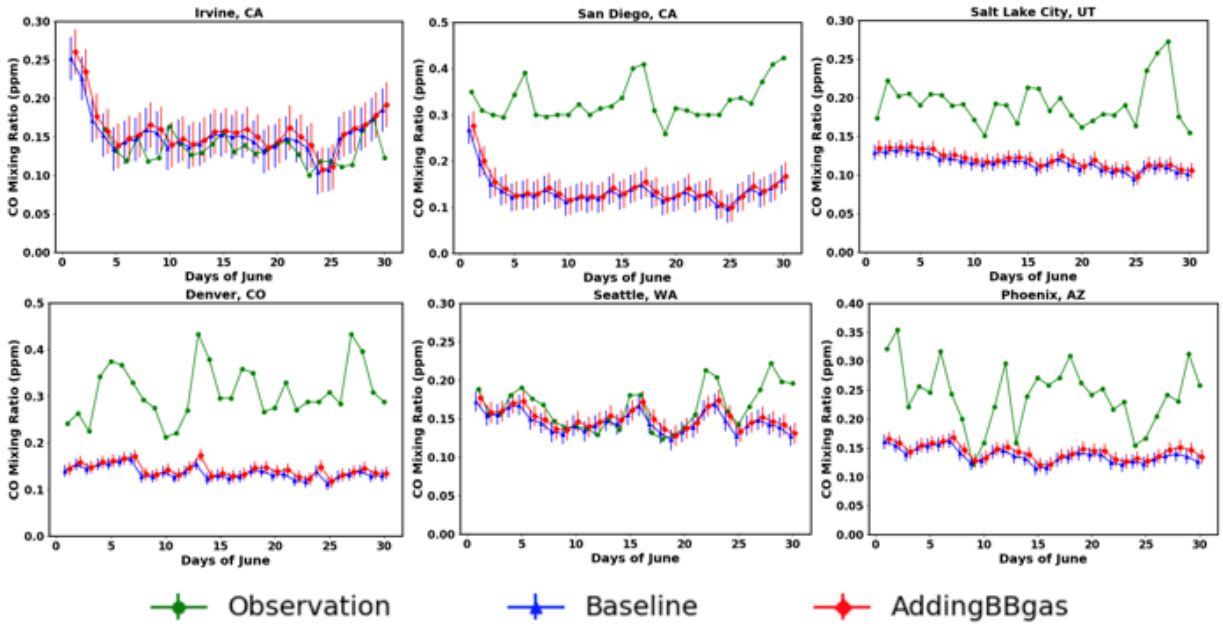


Figure 29. CO mixing ratio validations for six cities (as described in panel titles). Green lines are observations from EPA Air Data. Blue lines are Baseline simulation. Red lines are AddingBBgas simulation. Error bars are one standard deviation of day-to-day variability for the entire month.

#### 4.4.2.3 Improvement of OC

Similar to BC, simulated OC concentrations and spatial distributions underwent stage-wise improvements for the modifications mentioned above. In addition, OC does not only consist of primary sources but also secondary sources. Therefore, when comparing OC against observations or reanalysis products, we added one more simulation case VOC-to-SOA conversion (AddingSOA) for comparison. Figure 30 shows this improvement spatially (in log scale). Similar to BC, the OC spatial pattern is significantly impacted by the biomass burning locations. After AddingBBaerosol, the locations that witness strong biomass burning emissions become spatially consistent with MERRA2 products. Improvements as we see after adding the primary OC, the discrepancy between the simulation results and reanalysis remains large. Such differences can be

significantly reduced by comparing the AddingSOA with MERRA2 results. We also tested the results for TriplingEmission. In such cases, the simulated total OC tends to overshoot MERRA2 products.

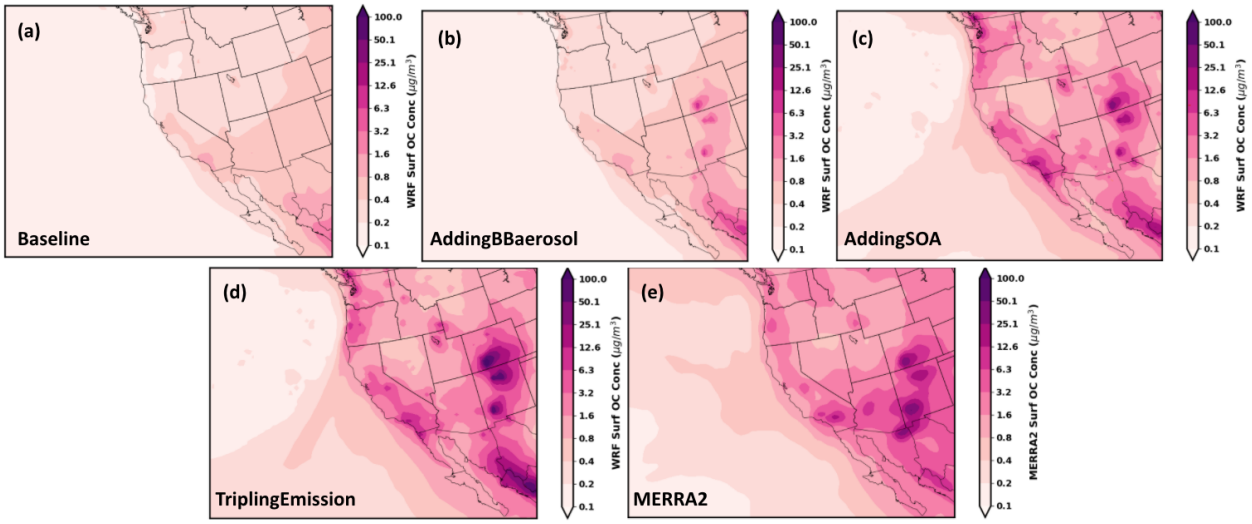


Figure 30. Surface OC concentrations in (a) Baseline, (b) AddingBBaerosol, (c) AddingSOA, (d) TriplingEmission and (e) MERRA2 products.

When comparing the simulated OC with observations from IMPROVE stations, the enhanced versions have much better performance than the Baseline (Figure 31). For most stations, the observed OC falls between the AddingSOA and TriplingEmission. Two stations (Lava Beds, CA, and Great Basin, NV) h ave the observed OC even higher, albeit slightly than the TriplingEmission. For most observed days, the observations fall within the range of simulation results, indicating that the enhanced model implementation successfully captures the overall levels of OC concentrations correctly.

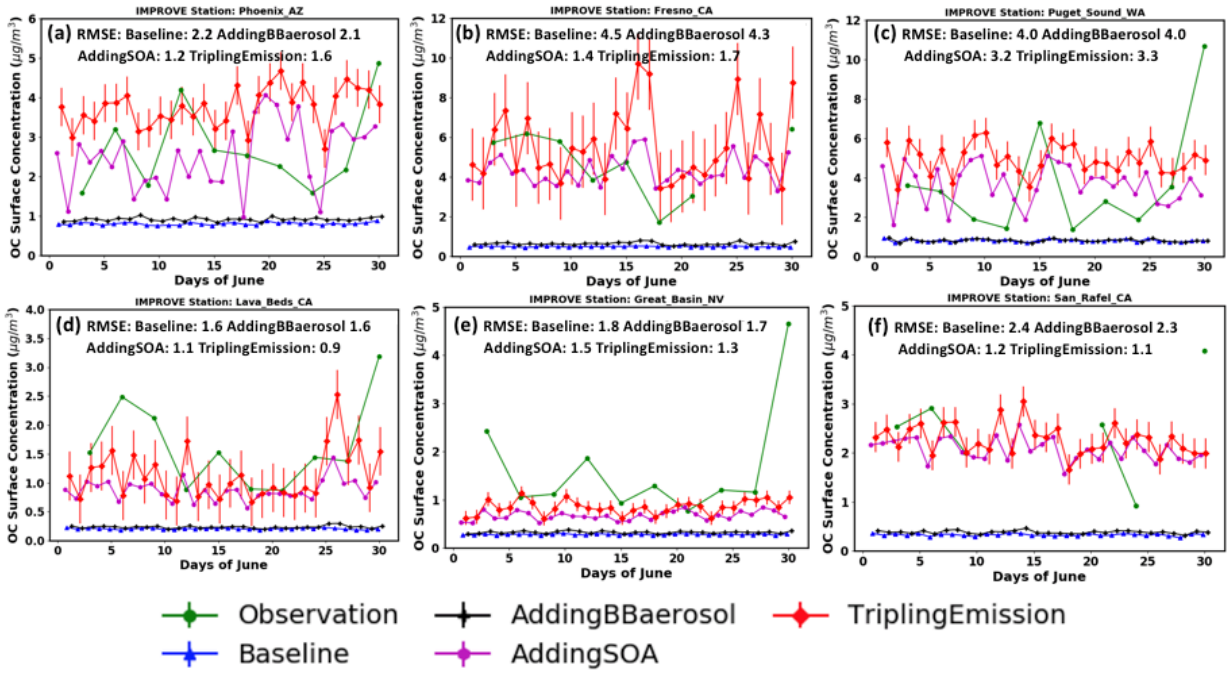


Figure 31. OC surface concentration for six stations. Green lines are observations from IMPROVE stations. Blue lines are the Baseline; black lines are AddingBBaerosol; magenta lines are AddingSOA and red lines are TriplingEmission. Red error bars are one standard deviation of day-to-day variability for the entire month for TriplingEmission.

One may wonder why the simulated day one concentrations are different for AddingSOA and TriplingEmission as model should have the same initial state. The reason is straightforward. For plotted data, we conducted daily average as model were initiated at hour zero with forward running time step of 90 seconds and hourly output frames. Figure 32 shows that all selected sites have same initial states but the TriplingEmission curve tend to reach higher values hours after the initial state. We also selected Fresno, CA and Great Basin, NV to illustrate this. Fresno, CA sees relatively large value discrepancies between TriplingEmission and AddingSOA later in the day while Great Basin, NV has almost identical values throughout the day. Panel (g)-(f) of Figure 32 explains such pattern. Fresno, CA locates right next to a biomass burning hotspot (<100 miles)

while Great Basin, NV has little emission sources nearby and therefore witness an almost identical simulated levels for two configurations.

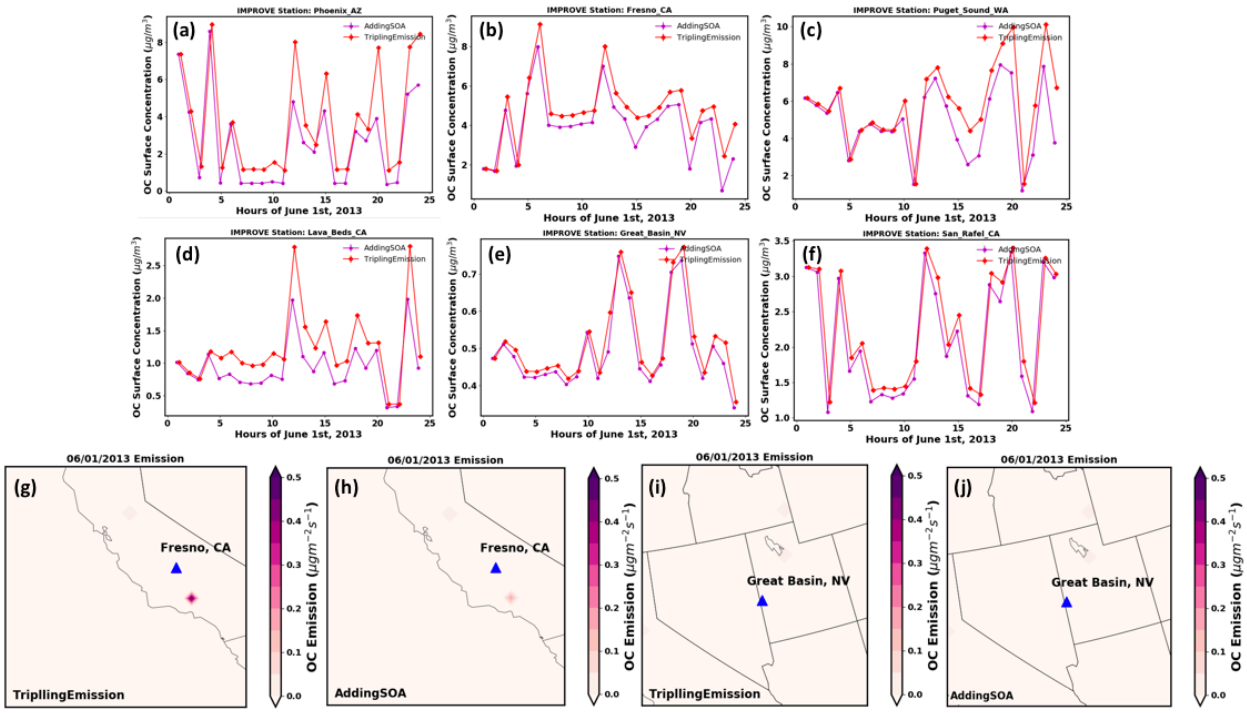


Figure 32. (a)-(f) hourly outputs for simulated OC concentrations for six sites on 06/01/2013. (g)-(f) Biomass burning spatial distribution for surrounding areas for Fresno, CA and Great Basin, NV. Panels (g) and (i) are for TriplingEmission and (h) and (j) are for AddingSOA.

### 4.4.3 Comparison with MOZART-MOSAIC

One crucial question we aim to answer here is how good the results are from the CBMZ-MAM3 simulation compared to the MOZART-MOSAIC counterpart. Thus, we evaluated the BC, OC, and AOD results for MOZART-MOSAIC simulation as well. To maintain input consistency, the evaluation was conducted based on the original emission levels (no enhancements). Figure 33 shows the comparison between MOZART-MOSAIC and CBMZ-MAM3 simulation results. For

BC, the MOZART-MOSAIC yields comparable levels of concentrations compared to CBMZ-MAM3 simulations while for OC, the MOZART-MOSAIC has much lower values compared to the CBMZ-MAM3 results. When using MERRA2 products as the benchmark, the improved CBMZ-MAM3 actually produces better results despite being a less sophisticated chemistry scheme. For AOD, the two suites have comparable performance in terms of the absolute magnitude but we are still able to identify better spatial agreement for the CBMZ-MAM3 scheme. Moreover, the CBMZ-MAM3 chemistry suite demands 2.5-time less computational core hours compared to MOZART-MOSAIC simulations.

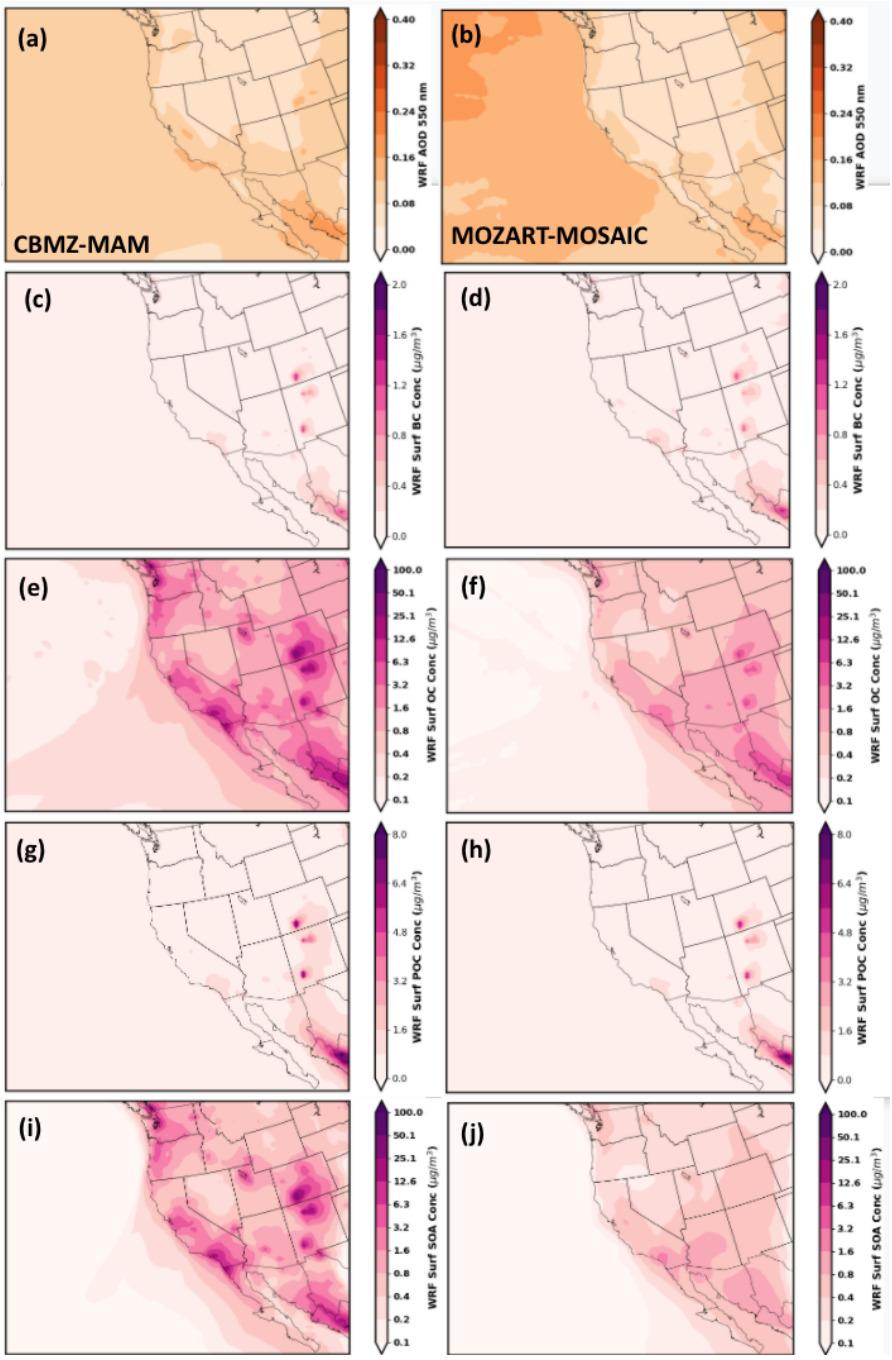


Figure 33. Comparison of two chemistry suites. (Left column: a, c, e, g, i) are for CBMZ-MAM and (right column: b, d, f, h, j) are for MOZART-MOSAIC runs of AddingSOA, but not TriplingEmission. First row (a, b) is for AOD at 550 nm. Second row (c, d) is for BC. Third row (e, f) is for OC (in log scale). Fourth row (g, h) is for Primary OC and fifth row is for SOA (in log scale).

The major simulated OC difference between the two suites comes from the treatment of SOA. Figure 33 also shows the comparison of both primary OC and secondary OC between MOZART-MOSAIC simulations and CBMZ-MAM3 simulations. For primary OC, two chemistry suites show comparable results both in spatial pattern and magnitude. However, the enhanced CBMZ-MAM3 simulation is capable of picking up the SOA but MOZART-MOSAIC fails. One plausible explanation could be that the added VOC species contain hydroxyacetone for MAM3 and this species dominates the VOC to SOA conversion. However, the current MOZART-MOSAIC simulation has not incorporated this process yet.

## 4.5 Summary

WRF-CAM5 is widely used in many atmospheric chemistry applications, such as air quality, chemistry and climate interaction (Zhang et al., 2015). In this study, we enhanced the CBMZ-MAM3 chemistry suite in WRF-CAM5 by modifying both CBMZ and MAM modules and any accompanying modules or registry (i.e., plume rise module, emission driver module and chemistry driver module). We performed four modifications, including (1) adding the model capability of ingesting the biomass burning emitted aerosols in MAM (AddingBBaerosol); (2) adding the model capability of ingesting the biomass burning emitted gases in CBMZ (AddingBBgas); (3) implementing the VOC to SOA conversions (AddingSOA) and (4) enhancing the original emissions by 3 times (TriplingEmission).

The simulated results see stepwise improvements after each modification. These improvements lead to not only more spatially consistent but also with higher surface observational agreements. Both the modeled concentrations of aerosol and gas-phase species and the AOD at 550 nm show significant improvements after the aforementioned modifications. Species-wise, the

BC has better agreement with observations compared to the OC, potentially due to the simpler OC-related chemistry process involved as we only need to care about the direct emissions of BC instead of secondary processes. Nonetheless, we are still able to identify clear advancements for OC after introducing the secondary VOC-to-SOA processes and emission enhancement. In general, when compared to the observations, the model performance follows the order of TriplingEmission > AddingSOA > AddingBBaerosol > Baseline. This study suggests that the low biases of the current version (Baseline) comes from both model deficiencies (no ingested biomass burning emissions and VOC to SOA conversions) and imperfect emission inventories. The readers are reminded that there remain uncenrtainties regarding the tripling sectors of emissions (e.g., anthropogenic, biomass burning or bogenic emissions).

Furthermore, we also tested the modified chemistry package with a parallel MOZART-MOSAIC set-up. Results suggest that for directly emitted species (e.g., BC), they are comparable and for species involving secondary processes (e.g., OC), CBMZ-MAM3 has a higher agreement with the MERRA2 reanalysis data. It is noteworthy that the MOZART-MOSAIC chemistry suite is generally considered to be more sophisticated and the CBMZ-MAM3 chemistry suite actually costs 2.5-time less computational core hours than the MOZART-MOSAIC counterparts. Results here suggest that our improved WRF-CAM5 model with CBMZ-MAM3 schemes can not only produce trustworthy simulations but also make prospective examinations more computationally feasible. Future studies may consider implementing our upgraded CBMZ-MAM3 chemistry suites for testing elsewhere or in other temporal periods to check if these improved modules are indeed boosting the WRF-CAM5 performance consistently.

# CHAPTER V

# WRF-CAM5 SIMULATED CLOUDS IN THE US WEST COAST

## 5.1 Introduction

The west coast of US consists of more than 15% of total US residents, which translates to more than 48 million population (US Census, 2010). California alone, for example, contributes to more than 3 trillion Gross domestic product (GDP) or approximately 1/7 of total GDP of the entire country (BEA, 2019). The juxtaposition of two major metropolitans: Los Angeles metropolitans and San Francisco Bay Area emit more than 270 million tons of CO2 per year (CARB, 2017) along with other major aerosol species (BC, OC, $SO_4$, etc.). In addition, California becomes a hotspot of wildfires in summertime (Herndon and Whiteside, 2018). The overwhelming amount of aerosol release from biomass burning not only causes significant economic losses, but also poses alarming respiratory health threats to local residents (Reid et al., 2016). In addition, studies (Grell et al., 2011; Tomaz et al., 2018) has suggested that biomass burning introduced aerosols can later turn into cloud seeds by serving as cloud condensation nuclei.

The wide-ranging MBL clouds near the US west coast makes these low clouds particularly susceptible to the influences of continental aerosols from both anthropogenic and biomass burning origins (Painemal, et al., 2015; Petters, et al., 2006). It has been noticed that, MBL tends to have biased dependency on aerosol types. For example, Tomlinson et al., (2007) investigated the presence of MBL in Southeast Pacific and noticed that despite the abundance of primary OC particles, the seeding efficiency for CCN is rather poor. In addition, for chemical species, other studies (e.g., Allan et al., 2000; Carpenter, 2003; Gomez et al., 2013) also emphasized the

importance of MBL iodine interactions in the lower levels as iodine, a halogen, is capable of catalyzed destruction of ozone in the marine boundary layer.

In this study we aim to use the updated model to characterize the role of different aerosols (from both anthropogenic and biomass burning origins) at different height (by showing vertical proles) in cloud properties changes, and further investigate the cloud dependencies on various aerosols types. Finally, we integrate the chemistry analyses with ambient meteorological fields to account for such biases in different parts of the US west coast.

## 5.2 Methods

In this study, we adopt the same model setups as in Section 2.3. Instead of using multiple model configurations, we choose TriplingEmission run, the final and best performing simulation compared to various benchmarks, for the examination.

For this study, we extend the simulation of updated WRF-CAM5 model for additional two month, making the total simulation covering the entire summertime (June 1st, 2013 to August 31st, 2013) with same setups, including emissions, as one-month TriplingEmission run. We define a coastal area, focusing on cloud properties and aerosol-cloud interactions in this region. The defined off coast region was a tilted rectangular area (Figure 34a) with longitude spans from 132 °W to 122°W and latitude from 30°N to 48°N. Please note that the defined area shown in Figure 34a may look like trapezoid instead of rectangle. This is due to the distortion caused by the map projection (lambert conformal) here and the defined area will look like a rectangle in a Mercator projection.

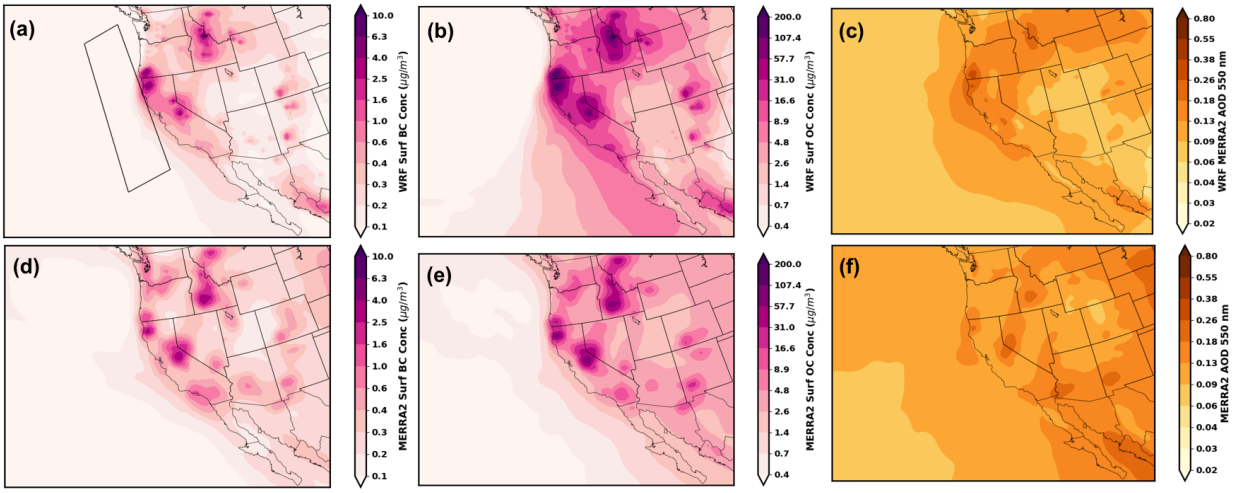


Figure 34. TriplingEmission simulation (First Row) and MERRA2 products (Second Row) for (a,d) BC, (b,e) OC, (c,f) AOD at 550 nm.

After defining the coastal area, we aim to separate such area into three sections: North Box, Central Box and South Box (Figure 35) to test their respective cloud properties and responses to the presence of aerosols. For simplicity, we make the heights of all boxes equal, from surface to 1000 m aloft. For Latitude of separations, the North Box is bounded between 42.67°N and 48°N; the Central Box is bounded between 35.33°N and 42.67°N and the South Box is bounded between 30°N and 37.33 °N. Since the off coast selection area is tilted (i.e., not in parallel with longitudinal lines), when conducting the spatial averages for vertical profile analyses, we proceed along a tilted line with angle of 0.38 rad to a constant latitude line. In addition, for temporal analyses, we conduct the running average to turn hourly data in to weekly data to reduce the noise.

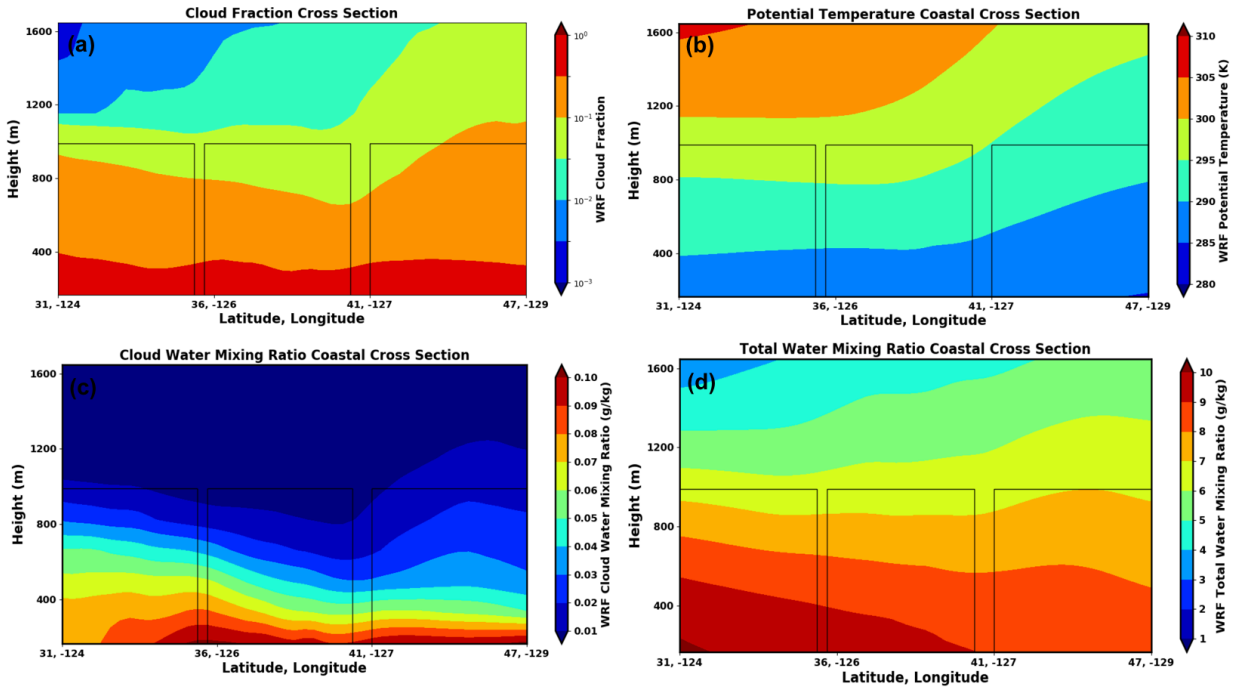


Figure 35. Averaged west coast boxed area vertical cross sections for (a) TriplingEmission simulation and (b) MODIS product. Total column summed water vapor from (c) TriplingEmission simulation and (d) MERRA2 product. Three boxes in each figure indicate the selected north, central and south boxes.

In addition to model simulations, we also used multiple sources of criterion for both chemistry and cloud property comparisons. We use The Moderate Resolution Imaging Spectroradiometer (MODIS; Platnick et al., 2003) for validations of simulated cloud fractions and similar to section 2.3, we use MERRA2 products for both the validations of both chemical species (BC, OC and AOD) and cloud property (e.g., column burden of water vapor) for the entire three-month long period.

## 5.3 Results

### 5.3.1 Validations for Three-Month Simulations

We first compare the three-month chemistry results with MERRA2 products and Figure 34 shows such comparisons of BC, OC and AOD. Similar to one-month simulation shown in Section 3.3, the three-month results are highly consistent when compared to the benchmark and for both BC, and OC, the spatial patterns align with reanalysis product. Unlike, one-month simulation whose hot spots are concentrated in Colorado and New Mexico, the three-month simulation witnesses the highest BC and OC concentrations in west coast (California, Portland and Idaho). The biomass burning hot spots shown in the one-month simulation remains, however, dwarfed by the later and much more intense wildfires along the west coast. Like BC and OC, the AOD values are significantly impacted by the coastal biomass burnings and therefore demonstrate dominant high values in these regions.

In addition to chemistry fields, we also evaluated the three-month cloud-related properties. Figure 36 shows the spatial distribution comparisons of cloud fractions and column summed (burden) water vapor. For cloud fraction, the WRF-CAM5 simulation captures the spatial pattern as demonstrated from MODIS product. Two major peaks from simulation reside to the north and south of California with a local minimum in between. Similarly, in MODIS, both northern and southern areas show local maximum with central area showing local minimum of cloud fractions. For the magnitude of cloud fraction, the simulated results have on average 0.1 larger bias compared to the benchmark. Nonetheless, such value only accounts for less 12% of errors and shall be considered acceptable with comparable spatial patterns. Like cloud fraction, the simulated column summed (burden) water vapor is highly consistent with MERRA2 products as well. We see local

minimums along the coastal region and particularly close to the California. The farther south region was shown with much more abundant water vapors as expected due to its proximity towards the tropical areas. MERRA2 products show agreements on both minimums, maximums and overall spatial distributions with slightly higher values (~5 kg/m$^3$). Again, the difference here is small compared to the overall magnitude and shall be considered acceptable.

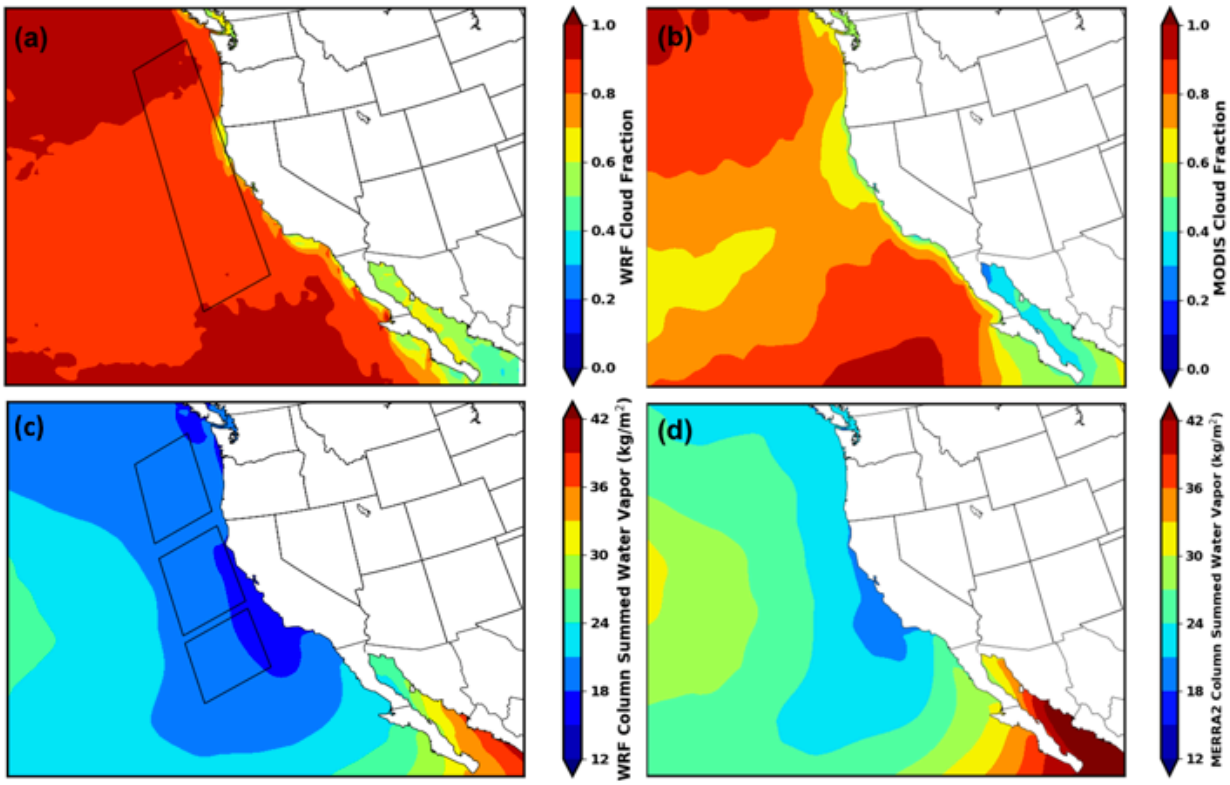


Figure 36. Cloud fraction from (a) TriplingEmission simulation and (b) MODIS product. Total column summed water vapor from (c) TriplingEmission simulation and (d) MERRA2 product. The black box in (a) indicates the selected region for off coast analyses and three black boxes in (c) indicate the breakdown of North, Central and South boxes.

### 5.3.2 Cloud Interactions with Aerosols

Figure 35 shows the ambient meteorological conditions for north, central and south boxes along the coastal area. For both cloud fractions and potential temperature, three boxes show comparable and largely invariant distributions. However, when considering the water content, three boxes demonstrate distinctive patterns. For example, the South Box has the lowest cloud water mixing ratio among three boxes while it has the highest total water mixing ratios among three boxes. In contrast to South Box, both Central and North Boxes see the high cloud water mixing ratios while they the low total water mixing ratio. Such inconsistency indicates that the water availability is not the only factor that dominate the cloud formation in this region.

Aerosols can serve as CCN and therefore facilitate the formation of cloud (Roberts et al., 2006). Thus, we show the vertical profile of total aerosol concentrations in the area. Figure 37a shows the total aerosol concentration in the region with Central Box showing a dominant level followed by the South Box. The North Box, on the contrary, has much lower aerosol concentrations compared to both Central and South Boxes. We also show the cloud effective radius (Figure 37b) in company with aerosol levels. For effective radius, the Central Box is smaller than the South Box. This is expected because the Central Box has more abundant aerosols compared to the South Box. However, the North Box has the smallest cloud effective radius despite being the box with lowest aerosol concentrations. Although such distribution seems to contradict the Twomey Effect (Feingold et al., 2003), we should also consider the availability of cloud water as well. Figure 37c shows the cloud water number concentration and we can clearly identify that both South and Central Boxes have much less cloud water concentrations compared to the North Box. Additionally, when comparing the time series of all three variables analyzed in the Figure 37, the supply of aerosols tends to be heavily affected by the biomass burning events in the latter half of

the study period, during which time the supply of water number concentration is relatively low in the area and therefore potentially resulting a larger than expected cloud effective radius in the South and Central Boxes.

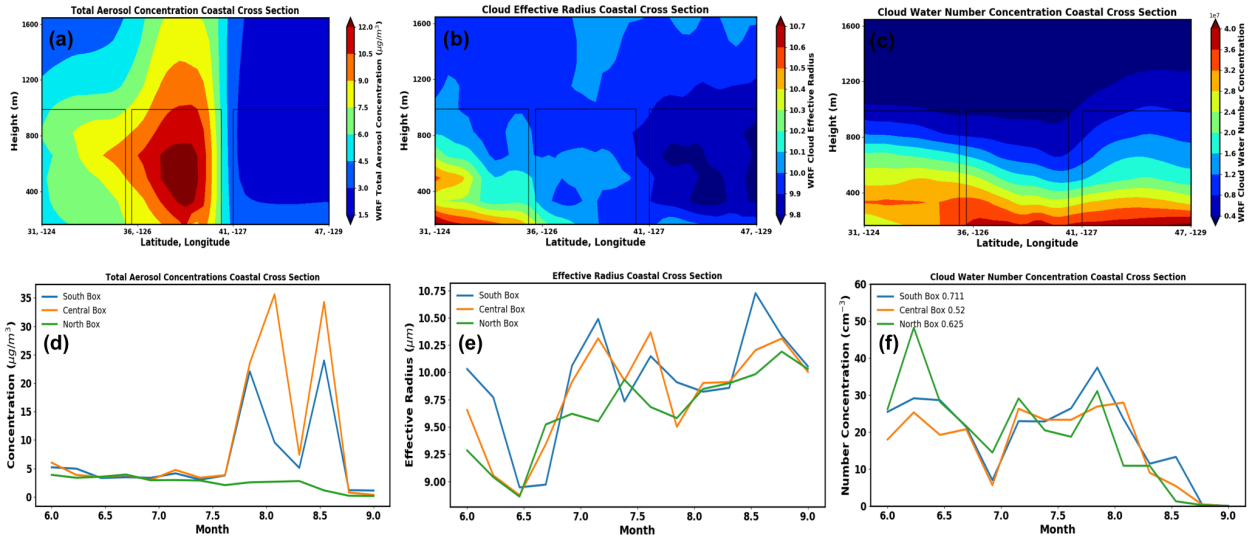


Figure 37. Averaged west coast boxed area vertical cross sections for (a) Total aerosol concentrations (b) cloud effective radius and (c) cloud water number concentrations. Three boxes in each figure indicate the selected north, central and south boxes. (d), (e), (f) are time series for (a), (b), (c), respectively.

We next break the aerosol compositions down for all three boxes (Figure 38). For all three boxes, two species dominate the total concentration: OC and $SO_4$. Both South and Central Boxes have very similar aerosol composition with OC as the most abundant aerosol followed by $SO_4$. However, such composition is not true for the North Box where the $SO_4$ becomes the most abundant aerosol and OC falls even behind the levels of sea salt. The discrepancy here implies that there are biased supplies to the aerosol in three different boxes.

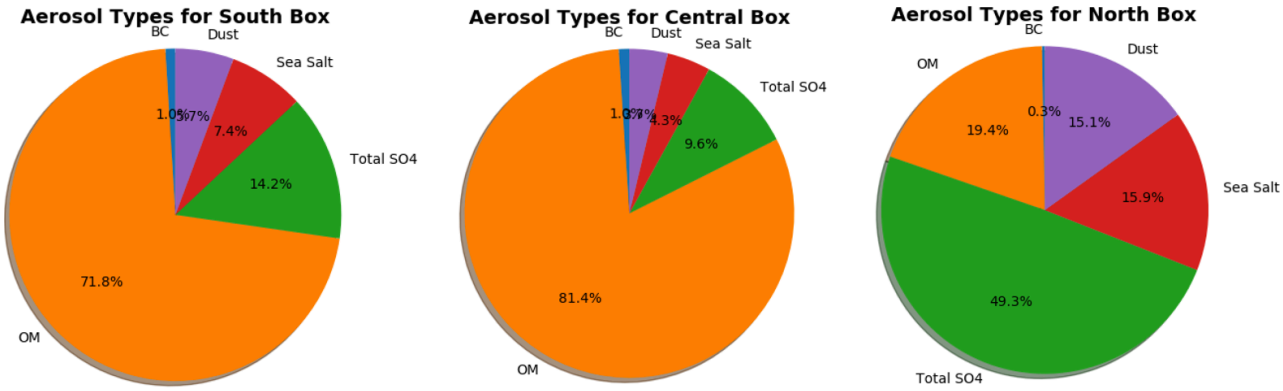


Figure 38. Aerosol distributions for (a) South, (b) Central and (c) North boxes.

Since OC and $SO_4$ are two most important aerosols in the region, we examine their concentrations and vertical profiles individually (Figure 39). OC has very similar vertical distributions and time series compared to the total aerosol concentrations (Figure 37), which is expected as OC dominates the aerosol composition in both South and Central Box. For $SO_4$, the North Box has the highest levels and the other two boxes share similar total concentrations. Such variation also helps explain the cloud effective radius distribution shown in Figure 37b as $SO_4$ has higher hygroscopicity compare to OC (Cruz and Pandis, 2000). More importantly, the abundance of $SO_4$ coincides with the time period when the water number concentration stays high for the North Box as well (first half of the time period).

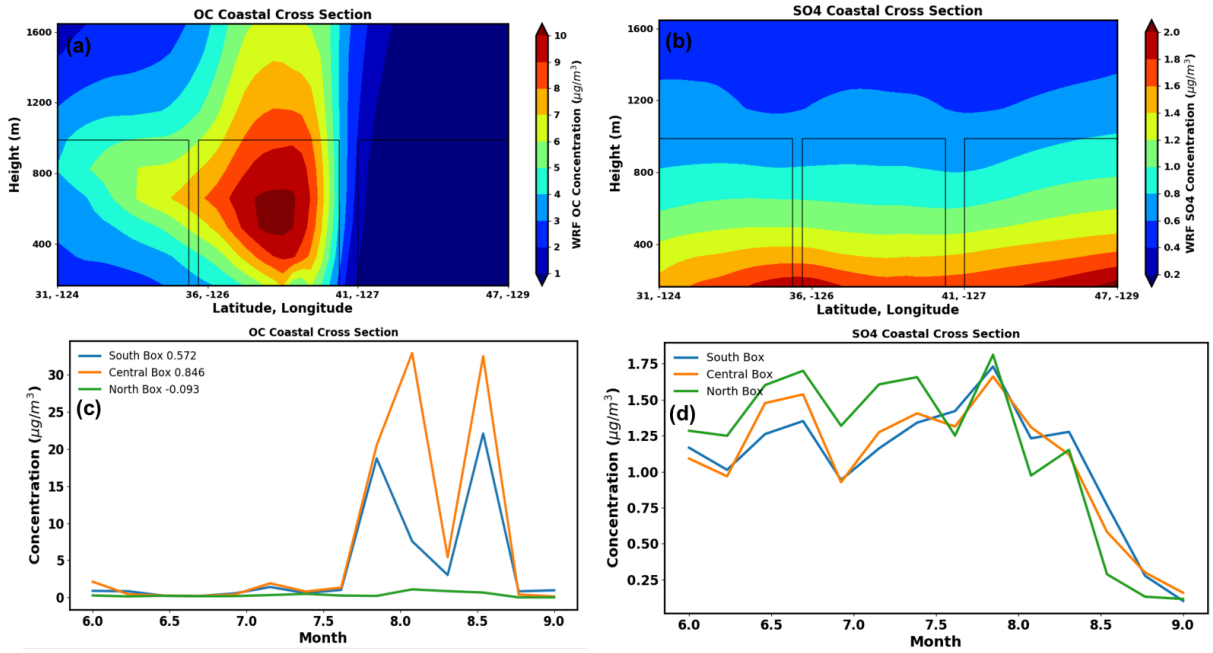


Figure 39. Averaged west coast boxed area vertical cross sections for (a) OC and (b) $SO_4$. (c) and (d) are time series for (a) and (b).

Moreover, to justify the biased coastal cloud response to OC and $SO_4$ concentrations, we select the days with top 25% OC and $SO_4$ concentrations and examine their responses to high aerosol concentration scenarios. In Figure 40, the distinctive cloud fraction spatial patterns are very obvious. In days with elevated OC levels, the Central and Southern part of coastal area see net increases in cloud fraction while in days with high $SO_4$ values, the northern part of coastal area experiences the most remarkable cloud fraction boost followed by the southern part. In contrast, the Central part stays largely invariant according to the changes of $SO_4$ levels.

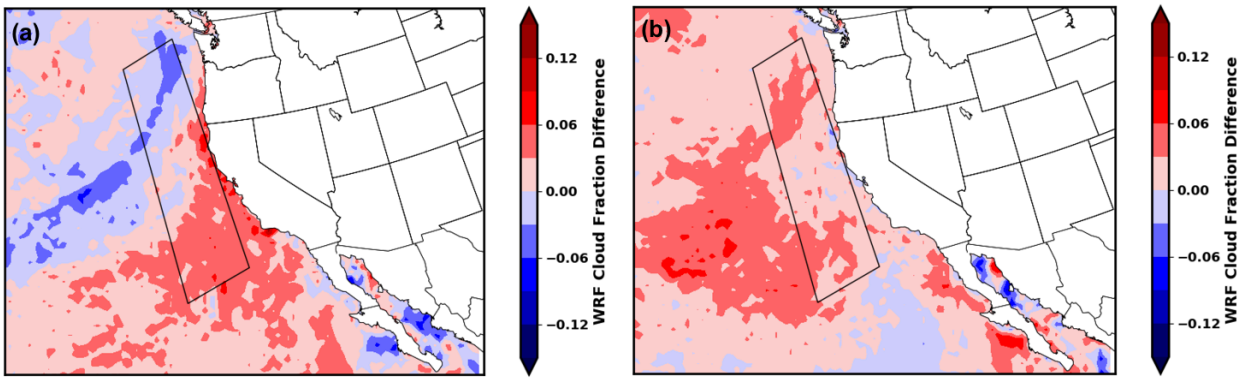


Figure 40. Cloud fractions for days with top 25% of (a) BC Concentrations and (b) Sulfate Concentrations.

The biased aerosol concentrations off the west US coast raises the question that what has caused the biased aerosol dependencies in different boxes? The answer lies in the emission sources and ambient meteorological conditions. Figure 41 shows the spatial distributions for OC and $SO_4$ along with averaged surface wind vectors overlaid. For OC, the emission source overwhelmingly comes from the biomass burning events near the California-Portland border along the coast while for $SO_4$, the dominant sources actually come from the long-range transport and this is consistent with some Asian-originated aerosol transport studies (Van Donkelaar et al., 2008). Additionally, wind fields served different purpose for three boxes. When biomass burning plumes get dispersed into the air, the southward prevailing wind carries OC particles towards Central and South Boxes. Since the North Box resides in the opposite direction of wind, it receives little OC from coastal biomass burnings despite being in the proximity. For $SO_4$, which potentially has an Asian origin, the North Box becomes the area with shortest distance after aerosols take a northern trans-Pacific route (Van Donkelaar et al., 2008). Therefore, the North Box is dominated by $SO_4$ aerosols and

see higher levels when compared to the other two boxes. Finally, it contributes to various cloud properties in North Box as mentioned above.

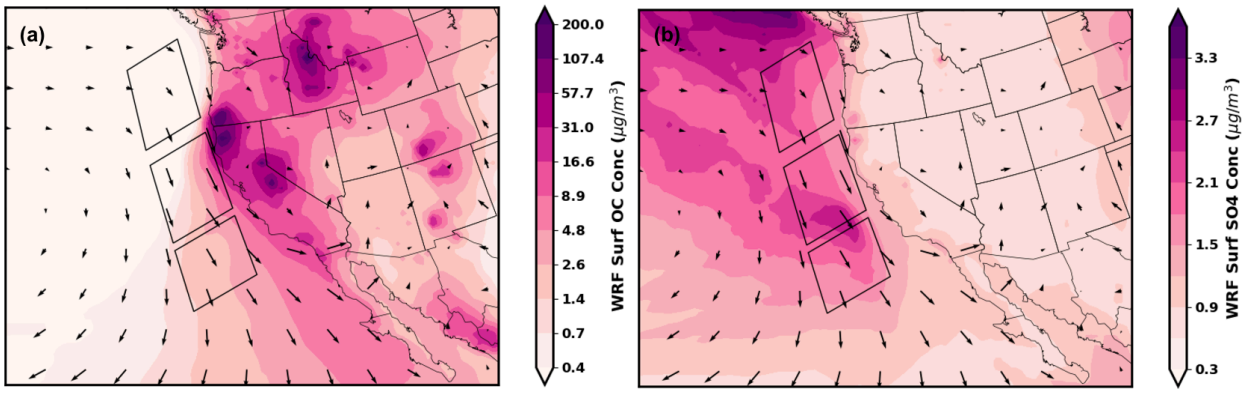


Figure 41. Aerosol concentration spatial distributions for (a) OC and (b) $SO_4$. Arrows are temporal averaged wind vectors. Three boxes in each panel corresponds to three surface boxes.

### 5.4 Concluding Remarks

The three-month TriplingEmission simulation produced reasonable results for both chemistry fields and cloud properties when compared to MODIS and MERRA2 benchmarks. We selected a boxed area along the coast for studies of off coast MBL clouds and their interactions with various types of aerosols.

For the selected coastal box, we further divide them into three parts: North, Central and South Boxes. In general, the South and Central Boxes share a lot of similarities while the North Box have distinctive patterns compared to the other two. The South Box contains the highest total water mixing ratio while demonstrating the lowest cloud water content. Such discrepancy is aerosol-related as the Central and South Boxes have much higher total aerosol concentrations when

compared to the North Box. In addition, the OC dominates the South and Central Boxes while the North Box sees the $SO_4$ to be the aerosol with highest concentrations. Due to its higher hygroscopicity and co-occurrences of water abundant time period, the $SO_4$ has led the North Box to produce lower cloud effective radius compared to both Central and South Boxes.

Finally, the biased aerosol dependencies in three boxes are aerosol source and origin dependent. The OC abundant boxes (South and Central) receive the OC aerosols from coastal biomass burning sources while the $SO_4$ rich box (North) accepts the $SO_4$ aerosols from East Asia long-range transport. Moreover, the local wind fields promote the southward dispersions of OC particles, impeding the OC particles to reach North Box. On the contrary, such wind direction facilitates the trans-Pacific $SO_4$ to reach North Box with a shorter distance.

### 5.5 Summary of WRF-CAM5 Improvements and Cloud-Aerosol Interactions

We improved a chemistry suite (CBMZ-MAM3) for WRF-CAM5 model. We performed four modifications (AddingBBaerosol, AddingBBgas, AddingSOA and TriplingEmission) for the original model. The simulated results show progressive improvement out of each version for various chemical species as well as AOD when compared with the benchmarks. In addition, we compared our improved WRF-CAM5 model with WRF-Chem model using a much more complicated chemistry suite (MOZART-MOSAIC). Our model demonstrates higher agreement with reanalysis products despite using ~2.5 time less computational resources for simulation.

In Chapter V, we conducted preliminary aerosol-cloud studies in the off coast area of US west coast. We extended the WRF-CAM5 simulation from one month to three months. The simulated results show agreement not only for chemistry fields but also cloud properties. We divide the selected off coast areas into three boxes and identified different aerosol and cloud patterns in the

North Box when compared to the other two boxes. The North Box is heavily $SO_4$ dominated while the other two are OC dominated. The different hygroscopicity of different aerosols lead to different cloud properties like: cloud effective radius. The biased aerosol dominance in three boxes are due to their source of origins and local wind patterns.

# REFERENCES


Abdul-Razzak, H., & Ghan, S. J. (2002). A parameterization of aerosol activation 3. Sectional representation. Journal of Geophysical Research, 107(D3), 4026.

Adler, R. F., Huffman, G. J., Bolvin, D. T., Curtis, S., & Nelkin, E. J. (2000). Tropical rainfall distributions determined using TRMM combined with other satellite and rain gauge information. Journal of Applied Meteorology, 39(12), 2007-2023.

Ahlgrimm, M., Forbes, R. M., Hogan, R. J., & Sandu, I. (2018). Understanding global model systematic shortwave radiation errors in subtropical marine boundary layer cloud regimes. Journal of Advances in Modeling Earth Systems, 10(8), 2042-2060.

Aiken, A. C., Decarlo, P. F., Kroll, J. H., Worsnop, D. R., Huffman, J. A., Docherty, K. S., ... & Sun, Y. (2008). O/C and OM/OC ratios of primary, secondary, and ambient organic aerosols with high-resolution time-of-flight aerosol mass spectrometry. Environmental Science & Technology, 42(12), 4478-4485.

Allan, B. J., McFiggans, G., Plane, J. M., & Coe, H. (2000). Observations of iodine monoxide in the remote marine boundary layer. Journal of Geophysical Research: Atmospheres, 105(D11), 14363-14369.Anderson, G. B., Bell, M. L., & Peng, R. D. (2013). Methods to calculate the heat index as an exposure metric in environmental health research. *Environmental Health Perspectives*, *121*(10), 1111.

Alexander, L. V. (2016). Global observed long-term changes in temperature and precipitation extremes: a review of progress and limitations in IPCC assessments and beyond. Weather and Climate Extremes, 11, 4-16.

Allen, R. J., W. Landuyt, and S. T. Rumbold (2016), An increase in aerosol burden and radiative effects in a warmer world, Nat. Clim. Change, 6(3), 269.

Appelhans, T., A. Sturman, and P. Zawar-Reza (2013), Synoptic and climatological controls of particulate matter pollution in a southern hemisphere coastal city, Int. J. Climatol., 394 33(2), 463–479.

Arya, S. P. (1999), Air pollution meteorology and dispersion, vol. 310, Oxford University Press New York.

Auffhammer, M. (2014). Cooling China: The weather dependence of air conditioner adoption. *Frontiers of Economics in China,* 9(1), 70-84.

Aumont, B., F. Chervier, and S. Laval (2003), Contribution of hono sources to the nox/hox/o3 chemistry in the polluted boundary layer, Atmos. Environ., 37(4), 487–498.

Azhar, G. S., Mavalankar, D., Nori-Sarma, A., Rajiva, A., Dutta, P., Jaiswal, A., ... & Hess, J. J. (2014). Heat-related mortality in India: Excess all-cause mortality associated with the 2010 Ahmedabad heat wave. *PLoS One*, *9*(3), e91831.

BEA, 2019.

https://apps.bea.gov/itable/iTable.cfm?ReqID=70&step=1#reqid=70&step=1&isuri=1

Barnard, J. C., Fast, J. D., Paredes-Miranda, G., Arnott, W. P., & Laskin, A. (2010). Evaluation of the WRF-CAM5" Aerosol Chemical to Aerosol Optical Properties" Module using data from the MILAGRO campaign. Atmospheric Chemistry & Physics, 10(15).

Balakrishnaiah, G., Kumar, K. R., Reddy, B., Gopal, K. R., Reddy, R. R., Reddy, L. S. S., ... & Babu, S. S. (2011). Characterization of PM, PM 10 and PM 2.5 mass concentrations at a tropical semi-arid station in Anantapur, India. 92.60. Mt; 92.60. Sz.

Banta, R. M., C. J. Senff, A. B. White, M. Trainer, R. T. McNider, R. J. Valente, S. D. Mayor, R. J. Alvarez, R. M. Hardesty, D. Parrish, et al. (1998), Daytime buildup and nighttime

transport of urban ozone in the boundary layer during a stagnation episode, J. Geophys. Res., 103(D17), 22,519–22,544.

Bennartz, R. (2007). Global assessment of marine boundary layer cloud droplet number concentration from satellite. Journal of Geophysical Research: Atmospheres, 112(D2). Bey, I., Jacob, D. J., Yantosca, R. M., Logan, J. A., Field, B. D., Fiore, A. M., ... & Schultz, M. G. (2001). Global modeling of tropospheric chemistry with assimilated meteorology: Model description and evaluation. Journal of Geophysical Research: Atmospheres, 106(D19), 23073-23095.

Bhattacharya, S. K., Froehlich, K., Aggarwal, P. K., & Kulkarni, K. M. (2003). Isotopic variation in Indian Monsoon precipitation: records from Bombay and New Delhi. Geophysical Research Letters, 30(24).

Binkowski, F. S., & Shankar, U. (1995). The regional particulate matter model: 1. Model description and preliminary results. Journal of Geophysical Research, 100(D12), 26,191–26,209.

Bony, S., & Dufresne, J. L. (2005). Marine boundary layer clouds at the heart of tropical cloud feedback uncertainties in climate models. Geophysical Research Letters, 32(20).

Boos, W. R., and Z. Kuang (2010), Dominant control of the south asian monsoon by orographic insulation versus plateau heating, Nature, 463(7278), 218.

Brasseur, G. P., & Jacob, D. J. (2017). Modeling of atmospheric chemistry. Cambridge University Press.

Bruyère, C. L., Done, J. M., Holland, G. J., & Fredrick, S. (2014). Bias corrections of global models for regional climate simulations of high-impact weather. Climate Dynamics, 43(7-8), 1847-1856.

Cai, W., K. Li, H. Liao, H. Wang, and L. Wu (2017), Weather conditions conducive to beijing severe haze more frequent under climate change, Nat. Clim. Change, 7(4), 257–262.

California Air Resource Board, 2017. https://ww3.arb.ca.gov/cc/inventory/pubs/reports/2000_2016/ghg_inventory_trends_00-16.pdf

Cao, C., Lee, X., Liu, S., Schultz, N., Xiao, W., Zhang, M., & Zhao, L. (2016). Urban heat islands in China enhanced by high-PM pollution. *Nature communications*, *7*, 12509.

Carpenter, L. J. (2003). Iodine in the marine boundary layer. Chemical reviews, 103(12), 4953-4962.

Chen, H., Wang, H., Sun, J., Xu, Y., & Yin, Z. (2019). Anthropogenic fine particulate matter pollution will be exacerbated in eastern China due to 21st century GHG warming. Atmospheric Chemistry and Physics, 19(1), 233-243.

Chin, M., Rood, R. B., Lin, S. J., Müller, J. F., & Thompson, A. M. (2000). Atmospheric sulfur cycle simulated in the global model GOCART: Model description and global properties. Journal of Geophysical Research: Atmospheres, 105(D20), 24671-24687.

Chaturvedi, R. K., Joshi, J., Jayaraman, M., Bala, G., & Ravindranath, N. H. (2012). Multi-model climate change projections for India under representative concentration pathways. Current Science, 791-802.

Cohen, A. J., H. Ross Anderson, B. Ostro, K. D. Pandey, M. Krzyzanowski, N. Künzli, K. Gutschmidt, A. Pope, I. Romieu, J. M. Samet, et al. (2005), The global burden of disease due to outdoor air pollution, J. Toxicol. Environ. Health, 68(13-14), 1301–1307.

Cohen, A. J., Brauer, M., Burnett, R., Anderson, H. R., Frostad, J., Estep, K., ... & Feigin, V. (2017). Estimates and 25-year trends of the global burden of disease attributable to ambient

air pollution: an analysis of data from the Global Burden of Diseases Study 2015. The Lancet, 389(10082), 1907-1918.

Chow, J. C., & Watson, J. G. (2002). PM2. 5 carbonate concentrations at regionally representative Interagency Monitoring of Protected Visual Environment sites. Journal of Geophysical Research: Atmospheres, 107(D21), ICC-6.

Conibear, L., Butt, E. W., Knote, C., Arnold, S. R., & Spracklen, D. V. (2018). Stringent emission control policies can provide large improvements in air quality and public health in India. GeoHealth, 2(7), 196-211.

CPCB. 2009. National Ambient Air Quality Status 2009. http://cpcb.nic.in/cpcbold/upload/Publications/Publication_514_airqualitystatus2009.pdf

Cruz, C. N., & Pandis, S. N. (2000). Deliquescence and hygroscopic growth of mixed inorganic−organic atmospheric aerosol. Environmental Science & Technology, 34(20), 4313-4319.

Creilson, J., J. Fishman, and A. Wozniak (2003), Intercontinental transport of tropospheric ozone: a study of its seasonal variability across the north atlantic utilizing tropospheric ozone residuals and its relationship to the north atlantic oscillation, Atmos. Chem. Phys., 418 3(6), 2053–2066.

Dai, A. (2006). Recent climatology, variability, and trends in global surface humidity. *Journal of Climate*, *19*(15), 3589-3606.

Dar, S. S., & Ghosh, P. (2017). Estimates of land and sea moisture contributions to the monsoonal rain over Kolkata, deduced based on isotopic analysis of rainwater. Earth System Dynamics, 8(2).

Dash, S. K., & Mamgain, A. (2011). Changes in the frequency of different categories of temperature extremes in India. *Journal of Applied Meteorology and Climatology*, *50*(9), 1842-1858.

David, L. M., Ravishankara, A. R., Kodros, J. K., Pierce, J. R., Venkataraman, C., & Sadavarte, P. (2019). Premature mortality due to PM2. 5 over India: Effect of atmospheric transport and anthropogenic emissions. GeoHealth, 3(1), 2-10.

Davies, F., D. Middleton, and K. Bozier (2007), Urban air pollution modelling and measurements of boundary layer height, Atmos. Environ., 41(19), 4040–4049.

Davy, R., Esau, I., Chernokulsky, A., Outten, S., & Zilitinkevich, S. (2017). Diurnal asymmetry to the observed global warming. *International Journal of Climatology*, *37*(1), 79-93.

Dawson, J. P., B. J. Bloomer, D. A. Winner, and C. P. Weaver (2014), Understanding the meteorological drivers of us particulate matter concentrations in a changing climate, Bull. Am. Meteorol. Soc., 95(4), 521–532.

Dee, D. P., Uppala, S. M., Simmons, A. J., Berrisford, P., Poli, P., Kobayashi, S., ... & Bechtold, P. (2011). The ERA-Interim reanalysis: Configuration and performance of the data assimilation system. Quarterly Journal of the royal meteorological society, 137(656), 553-597.Doherty, R. M., Heal, M. R., Wilkinson, P., Pattenden, S., Vieno, M., Armstrong, B., ... & Stevenson, D. S. (2009). Current and future climate-and air pollution-mediated impacts on human health. *Environmental health*, *8*(1), S8.

Dee, D. P., S. Uppala, A. Simmons, P. Berrisford, P. Poli, S. Kobayashi, U. Andrae, M. Balmaseda, G. Balsamo, P. Bauer, et al. (2011), The era-interim reanalysis: Configuration and performance of the data assimilation system, Q. J. Royal Meteorol. Soc., 137(656), 553–427 597.

De Laat, A. T. J., & Lelieveld, J. (2002). Interannual variability of the Indian winter monsoon circulation and consequences for pollution levels. J. of Geophys. Research: Atmospheres, 107(D24).

De Sario, M., Katsouyanni, K., & Michelozzi, P. (2013). Climate change, extreme weather events, air pollution and respiratory health in Europe. European Respiratory Journal, 42(3), 826-843.Deshmukh, D. K., Deb, M. K., & Mkoma, S. L. (2013). Size distribution and seasonal variation of size-segregated particulate matter in the ambient air of Raipur city, India. Air Quality, Atmosphere & Health, 6(1), 259-276.

Díaz, J. P., Expósito, F. J., Pérez, J. C., González, A., Wang, Y., Haimberger, L., & Wang, J. (2019). Long-Term Trends in Marine Boundary Layer Properties over the Atlantic Ocean. Journal of Climate, 32(10), 2991-3004.

Dickerson, R., S. Kondragunta, G. Stenchikov, K. Civerolo, B. Doddridge, and B. Holben (1997), The impact of aerosols on solar ultraviolet radiation and photochemical smog, Science, 278(5339), 827–830.

Doherty, R. M., Heal, M. R., Wilkinson, P., Pattenden, S., Vieno, M., Armstrong, B., ... & Stevenson, D. S. (2009). Current and future climate-and air pollution-mediated impacts on human health. Environmental health, 8(1), S8.

Doherty, R., O. Wild, D. Shindell, G. Zeng, I. MacKenzie, W. Collins, A. M. Fiore, D. Stevenson, F. Dentener, M. Schultz, et al. (2013), Impacts of climate change on surface ozone and intercontinental ozone pollution: A multi-model study, J. Geophys. Res., 118(9), 3744–3763.

Dubovik, O., & King, M. D. (2000). A flexible inversion algorithm for retrieval of aerosol optical properties from Sun and sky radiance measurements. Journal of Geophysical Research: Atmospheres, 105(D16), 20673-20696.

Durdina, L., Brem, B. T., Setyan, A., Siegerist, F., Rindlisbacher, T., & Wang, J. (2017). Assessment of particle pollution from jetliners: from smoke visibility to nanoparticle counting. Environmental Science & Technology, 51(6), 3534-3541.

Drury, E., Jacob, D. J., Spurr, R. J., Wang, J., Shinozuka, Y., Anderson, B. E., ... & Weber, R. (2010). Synthesis of satellite (MODIS), aircraft (ICARTT), and surface (IMPROVE, EPA-AQS, AERONET) aerosol observations over eastern North America to improve MODIS aerosol retrievals and constrain surface aerosol concentrations and sources. Journal of Geophysical Research: Atmospheres, 115(D14).

Easter, R. C., Ghan, S. J., Zhang, Y., Saylor, R. D., Chapman, E. G., Laulainen, N. S., ... Zaveri, R. A. (2004). MIRAGE: Model description and evaluation of aerosols and trace gases. J. of Geophys. Research, 109, D20210.

Eder, B. K., J. M. Davis, and P. Bloomfield (1993), A characterization of the spatiotemporal variability of non-urban ozone concentrations over the eastern united states, Atmos. Environ., 27(16), 2645–2668.

El-Zanan, H. S., Lowenthal, D. H., Zielinska, B., Chow, J. C., & Kumar, N. (2005). Determination of the organic aerosol mass to organic carbon ratio in IMPROVE samples. Chemosphere, 60(4), 485-496.Emmerson, K. M., & Evans, M. J. (2009). Comparison of tropospheric gas-phase chemistry schemes for use within global models. Atmospheric Chemistry & Physics, 9(5).

Emmons, L. K., Walters, S., Hess, P. G., Lamarque, J. F., Pfister, G. G., Fillmore, D., ... Kloster, S. (2010). Description and evaluation of the model for ozone and related chemical tracers, version 4 (MOZART-4). Geoscientific Model Development, 3, 43–67. https://doi.org/10.5194/gmd-3-43-2010.

EPA (2017). Air Data: Air Quality Data Collected at Outdoor Monitors Across the US. https://www.epa.gov/outdoor-air-quality-data

Fast, J. D., Gustafson Jr, W. I., Easter, R. C., Zaveri, R. A., Barnard, J. C., Chapman, E. G., ... & Peckham, S. E. (2006). Evolution of ozone, particulates, and aerosol direct radiative forcing in the vicinity of Houston using a fully coupled meteorology-chemistry-aerosol model. Journal of Geophysical Research: Atmospheres, 111(D21).

Feingold, G., Eberhard, W. L., Veron, D. E., & Previdi, M. (2003). First measurements of the Twomey indirect effect using ground-based remote sensors. Geophysical Research Letters, 30(6).

Feng, Y., & Ramanathan, V. (2010). Investigation of aerosol–cloud interactions using a chemical transport model constrained by satellite observations. Tellus B: Chemical and Physical Meteorology, 62(1), 69-86.

Fischer, E., D. Jaffe, D. Reidmiller, and L. Jaegle (2010), Meteorological controls on observed peroxyacetyl nitrate at mount bachelor during the spring of 2008, J. Geophys. Res.,

440 115(D3).

Fischer, E. M., & Knutti, R. (2013). Robust projections of combined humidity and temperature extremes. *Nature Climate Change*, *3*(2), 126-130.

Gadgil, S. (2003). The Indian monsoon and its variability. Annual Review of Earth and Planetary Sciences, 31(1), 429-467.

Gan, C. M., Pleim, J., Mathur, R., Hogrefe, C., Long, C. N., Xing, J., ... & Wei, C. (2015). Assessment of long-term WRF--CMAQ simulations for understanding direct aerosol effects on radiation" brightening" in the United States. Atmospheric Chemistry & Physics, 15(21).

Gan, M. A., Rao, V. B., & Moscati, M. C. (2005). South American monsoon indices. Atmospheric Science Letters, 6(4), 219-223.

Ganguly, D., P. J. Rasch, H. Wang, and J.-h. Yoon (2012), Fast and slow responses of the south asian monsoon system to anthropogenic aerosols, Geophys. Res. Lett., 39(18).

Galin, V. Y., Smyshlyaev, S. P., & Volodin, E. M. (2007). Combined chemistry-climate model of the atmosphere. Izvestiya, Atmospheric and Oceanic Physics, 43(4), 399-412.

Gantt, B., He, J., Zhang, X., Zhang, Y., & Nenes, A. (2014). Incorporation of advanced aerosol activation treatments into CESM/CAM5: model evaluation and impacts on aerosol indirect effects. Atmospheric Chemistry & Physics, 14(14).

Gelaro, R., McCarty, W., Suárez, M. J., Todling, R., Molod, A., Takacs, L., ... & Wargan, K. (2017). The modern-era retrospective analysis for research and applications, version 2 (MERRA-2). Journal of Climate, 30(14), 5419-5454.

Ghude, S. D., D. Chate, C. Jena, G. Beig, R. Kumar, M. Barth, G. Pfister, S. Fadnavis, and P. Pithani (2016), Premature mortality in india due to pm2.5 and ozone exposure, Geophys. Res. Lett., 43(9), 4650–4658.

Gómez Martín, J. C., Mahajan, A. S., Hay, T. D., Prados-Román, C., Ordóñez, C., MacDonald, S. M., ... & Agama Reyes, M. V. (2013). Iodine chemistry in the eastern Pacific marine boundary layer. Journal of Geophysical Research: Atmospheres, 118(2) , 887-904.

Gosling, S. N., McGregor, G. R., & Lowe, J. A. (2009). Climate change and heat-related mortality in six cities Part 2: climate model evaluation and projected impacts from changes in the mean and variability of temperature with climate change. International journal of biometeorology, 53(1), 31-51.

Goswami, B. N., Ajayamohan, R. S., Xavier, P. K., & Sengupta, D. (2003). Clustering of synoptic activity by Indian summer monsoon intraseasonal oscillations. Geophysical Research Letters, 30(8).

Goswami, B. N., & Mohan, R. A. (2001). Intraseasonal oscillations and interannual variability of the Indian summer monsoon. Journal of Climate, 14(6), 1180-1198.

Grell, G., Freitas, S. R., Stuefer, M., & Fast, J. (2011). Inclusion of biomass burning in WRF-Chem: impact of wildfires on weather forecasts. Atmospheric Chemistry & Physics, 11(11).Grell, G. A., Peckham, S. E., Schmitz, R., McKeen, S. A., Frost, G., Skamarock, W. C., & Eder, B. (2005). Fully coupled "online" chemistry within the WRF model. Atmospheric Environment, 39(37), 6957-6975.

Grell, G., Freitas, S. R., Stuefer, M., & Fast, J. (2011). Inclusion of biomass burning in WRF-CAM5: impact of wildfires on weather forecasts. Atmospheric Chemistry & Physics, 11(11).

Gu, Y., Liou, K. N., Ou, S. C., & Fovell, R. (2011). Cirrus cloud simulations using WRF with improved radiation parameterization and increased vertical resolution. Journal of Geophysical Research: Atmospheres, 116(D6).

Guenther, A., Karl, T., Harley, P., Wiedinmyer, C., Palmer, P. I., & Geron, C. (2006). Estimates of global terrestrial isoprene emissions using MEGAN (Model of Emissions of Gases and Aerosols from Nature).

Han, W., Vialard, J., McPhaden, M. J., Lee, T., Masumoto, Y., Feng, M., & De Ruijter, W. P. (2014). Indian Ocean decadal variability: A review. Bulletin of the American Meteorological Society, 95(11), 1679-1703.

Hawbaker, T. J., Radeloff, V. C., Syphard, A. D., Zhu, Z., & Stewart, S. I. (2008). Detection rates of the MODIS active fire product in the United States. Remote Sensing of Environment, 112(5), 2656-2664.

He, C., Flanner, M. G., Chen, F., Barlage, M., Liou, K. N., Kang, S., ... & Qian, Y. (2018). Black carbon-induced snow albedo reduction over the Tibetan Plateau: uncertainties from snow grain shape and aerosol–snow mixing state based on an updated SNICAR model. Atmospheric Chemistry and Physics (Online), 18(PNNL-SA-137623).

He, J., Zhang, Y., Wang, K., Chen, Y., Leung, L. R., Fan, J., ... & He, K. (2017). Multi-year application of WRF-CAM5 over East Asia-Part I: Comprehensive evaluation and formation regimes of O3 and PM2. 5. Atmospheric Environment, 165, 122-142.

Herring, S. C., Hoell, A., Hoerling, M. P., Kossin, J. P., Schreck III, C. J., & Stott, P. A. (2016). Explaining extreme events of 2015 from a climate perspective. Bulletin of the American Meteorological Society, 97(12), S1-S145.

Hong, S.-Y., Y. Noh, and J. Dudhia (2006), A new vertical diffusion package with an explicit treatment of entrainment processes, Mon. Weather Rev., 134(9), 2318–2341.

Holben, B. N., Eck, T. F., Slutsker, I. A., Tanre, D., Buis, J. P., Setzer, A., ... & Lavenu, F. (1998). AERONET—A federated instrument network and data archive for aerosol characterization. Remote sensing of environment, 66(1), 1-16.

Horton, D. E., C. B. Skinner, D. Singh, and N. S. Diffenbaugh (2014), Occurrence and persistence of future atmospheric stagnation events, Nat. Clim. Change, 4(8), 698.

Hu, X.-M., P. M. Klein, M. Xue, A. Shapiro, and A. Nallapareddy (2013), Enhanced vertical mixing associated with a nocturnal cold front passage and its impact on near-surface temperature and ozone concentration, J. Geophys. Res., 118(7), 2714–2728.

Hu, J., Zhang, H., Ying, Q., Chen, S. H., Vandenberghe, F., & Kleeman, M. J. (2015). Long-term particulate matter modeling for health effect studies in California–Part 1: Model performance on temporal and spatial variations. Atmospheric Chemistry and Physics, 15(6), 3445-3461.

Hurrell, J. W., Holland, M. M., Gent, P. R., Ghan, S., Kay, J. E., Kushner, P. J., ... & Lipscomb, W. H. (2013). The community earth system model: a framework for collaborative research. Bulletin of the American Meteorological Society, 94(9), 1339-1360.

Iacono, M. J., Delamere, J. S., Mlawer, E. J., Shephard, M. W., Clough, S. A., & Collins, W. D. (2008). Radiative forcing by long-lived greenhouse gases: Calculations with the AER radiative transfer models. Journal of Geophysical Research: Atmospheres, 113(D13).

Ihara, C., Kushnir, Y., Cane, M. A., & De la Pena, V. H. (2007). Indian summer monsoon rainfall and its link with ENSO and Indian Ocean climate indices. International Journal of Climatology: A Journal of the Royal Meteorological Society, 27(2), 179-187.

Im, E. S., Pal, J. S., & Eltahir, E. A. (2017). Deadly heat waves projected in the densely populated agricultural regions of South Asia. *Science advances*, *3*(8), e1603322.

Jackson, J. E., Yost, M. G., Karr, C., Fitzpatrick, C., Lamb, B. K., Chung, S. H., ... & Fenske, R. A. (2010). Public health impacts of climate change in Washington State: projected mortality risks due to heat events and air pollution. *Climatic Change*, *102*(1-2), 159-186.

Jacob, D. J., and D. A. Winner (2009), Effect of climate change on air quality, Atmos. Environ., 43(1), 51–63.

James, K. (2011), India's demographic change: opportunities and challenges, Science, 465 333(6042), 576–580.

Janssens-Maenhout, G., F. Dentener, J. Van Aardenne, S. Monni, V. Pagliari, L. Orlandini, Z. Klimont, J.-i. Kurokawa, H. Akimoto, T. Ohara, et al. (2012), Edgar-htap: a harmonized gridded air pollution emission dataset based on national inventories, European Commission Joint Research Centre Institute for Environment and Sustainability. JRC 68434 UR 25229 EUR 25229, ISBN 978-92-79-23123-0.

Jayasankar, C., S. Surendran, and K. Rajendran (2015), Robust signals of future projections of indian summer monsoon rainfall by ipcc ar5 climate models: Role of seasonal cycle and interannual variability, Geophys. Res. Lett., 42(9), 3513–3520.

Jendritzky et al.. UTCI—Why another thermal index? International Journal of Biometeorology. May 2012, Volume 56, Issue 3, pp 421–428

Jin, Y., Andersson, H., & Zhang, S. (2016). Air pollution control policies in China: a retrospective and prospects. International journal of environmental research and public health, 13(12), 1219.

Jones, B., & O'Neill, B. C. (2016). Spatially explicit global population scenarios consistent with the Shared Socioeconomic Pathways. Environmental Research Letters, 11(8), 084003.

Kang, S., & Eltahir, E. A. (2018). North China Plain threatened by deadly heatwaves due to climate change and irrigation. Nature communications, 9(1), 2894.

Katsouyanni, K., & Analitis, A. (2009). Investigating the synergistic effects between meteorological variables and air pollutants: results from the European PHEWE, EUROheatwave and CIRCE projects. Epidemiology, 20(6), S264.

Katsouyanni, K., & Analitis, A. (2009). Investigating the synergistic effects between meteorological variables and air pollutants: results from the European PHEWE, EUROheatwave and CIRCE projects. Epidemiology, 20(6), S264.

Khan, N., Shahid, S., bin Ismail, T., & Wang, X. J. (2019). Spatial distribution of unidirectional trends in temperature and temperature extremes in Pakistan. Theoretical and Applied Climatology, 136(3-4), 899-913.

Kharol, S. K., McLinden, C. A., Sioris, C. E., Shephard, M. W., Fioletov, V., van Donkelaar, A., ... & Martin, R. V. (2017). OMI satellite observations of decadal changes in ground-level sulfur dioxide over North America. Atmospheric Chemistry and Physics, 17(9), 5921.

Knote, C., Hodzic, A., Jimenez, J. L., Volkamer, R., Orlando, J. J., Baidar, S., ... Zhang, Q. (2014). Simulation of semi-explicit mechanisms of SOA formation from glyoxal in aerosol in a 3-D model. Atmospheric Chemistry and Physics, 14(12), 6213–6239.

Knutson, T. R., & Ploshay, J. J. (2016). Detection of anthropogenic influence on a summertime heat stress index. Climatic Change, 138(1-2), 25-39.

Kovats, R. S., & Hajat, S. (2008). Heat stress and public health: a critical review. *Annu. Rev. Public Health*, *29*, 41-55.

Koumoutsaris, S., I. Bey, S. Generoso, and V. Thouret (2008), Influence of el niño–southern oscillation on the interannual variability of tropospheric ozone in the northern midlatitudes, J. Geophys. Res., 113(D19).

Krishnamurthy, L., Vecchi, G. A., Yang, X., van der Wiel, K., Balaji, V., Kapnick, S. B., ... & Underwood, S. (2018). Causes and probability of occurrence of extreme precipitation events like Chennai 2015. Journal of Climate, 31(10), 3831-3848.

Krishnan, R., Zhang, C., & Sugi, M. (2000). Dynamics of breaks in the Indian summer monsoon. Journal of the atmospheric sciences, 57(9), 1354-1372.

Kumar, O. B., Naidu, C. V., Rao, S. R. L., & Rao, B. R. S. (2004). Prediction of southern Indian winter monsoon rainfall from September local upper‐air temperatures. Meteorological Applications: A journal of forecasting, practical applications, training techniques and modelling, 11(3), 189-199.

Kumar, R., Barth, M. C., Pfister, G. G., Delle Monache, L., Lamarque, J. F., Archer-Nicholls, S., ... & Walters, S. (2018). How will air quality change in South Asia by 2050?. Journal of Geophysical Research: Atmospheres, 123(3), 1840-1864.

Kumar, R., Delle Monache, L., Bresch, J., Saide, P. E., Tang, Y., Liu, Z., ... & Lee, P. (2019). Toward Improving Short-Term Predictions of Fine Particulate Matter Over the United States Via Assimilation of Satellite Aerosol Optical Depth Retrievals. Journal of Geophysical Research: Atmospheres, 124(5), 2753-2773.

Lal, M., & Harasawa, H. (2001). Future climate change scenarios for Asia as inferred from selected coupled atmosphere-ocean global climate models. Journal of the Meteorological Society of Japan. Ser. II, 79(1), 219-227.

Lamarque, J.-F., and P. G. Hess (2004), Arctic oscillation modulation of the northern hemisphere spring tropospheric ozone, Geophys. Res. Lett., 31(6).

Lamarque, J. F., Emmons, L. K., Hess, P. G., Kinnison, D. E., Tilmes, S., Vitt, F., ... & Orlando, J. J. (2012). CAM-chem: Description and evaluation of interactive atmospheric chemistry in the Community Earth System Model. Geoscientific Model Development, 5(2), 369.

Lamarque, J.-F., G. P. Kyle, M. Meinshausen, K. Riahi, S. J. Smith, D. P. van Vuuren, A. J. Conley, and F. Vitt (2011), Global and regional evolution of short-lived radiatively-active

gases and aerosols in the representative concentration pathways, Clim. change, 109(1-2), 191.

Langford, A., T. O'Leary, C. Masters, K. Aikin, and M. Proffitt (1998), Modulation of middle and upper tropospheric ozone at northern midlatitudes by the el niño/southern oscillation, Geophys. Res. Lett., 25(14), 2667–2670.

Latha, K. M., & Badarinath, K. V. S. (2003). Black carbon aerosols over tropical urban environment—a case study. Atmospheric Research, 69(1-2), 125-133.

Lelieveld, J., Evans, J. S., Fnais, M., Giannadaki, D., & Pozzer, A. (2015). The contribution of outdoor air pollution sources to premature mortality on a global scale. Nature, 525(7569), 367-371.

Lelieveld, J., & Pöschl, U. (2017). Chemists can help to solve the air-pollution health crisis. Nature, 291

Lelieveld, J., Bourtsoukidis, E., Brühl, C., Fischer, H., Fuchs, H., Harder, H., ... & Pozzer, A. (2018). The South Asian monsoon—pollution pump and purifier. Science, 361(6399), 270-273.

Lemke, B., & Kjellstrom, T. (2012). Calculating workplace WBGT from meteorological data: a tool for climate change assessment. Industrial Health, 50(4), 267-278.

Li, C., McLinden, C., Fioletov, V., Krotkov, N., Carn, S., Joiner, J., ... & Dickerson, R. R. (2017). India is overtaking China as the world's largest emitter of anthropogenic sulfur dioxide. Scientific reports, 7(1), 14304.

Li, C., and M. Yanai (1996), The onset and interannual variability of the asian summer monsoon in relation to land–sea thermal contrast, J. Clim., 9(2), 358–375.

Li, G., Zhou, M., Cai, Y., Zhang, Y., & Pan, X. (2011). Does temperature enhance acute mortality effects of ambient particle pollution in Tianjin City, China. Science of the Total Environment, 409(10), 1811-1817.

Li, K., Liao, H., Cai, W., & Yang, Y. (2018). Attribution of anthropogenic influence on atmospheric patterns conducive to recent most severe haze over eastern China. Geophysical Research Letters, 45(4), 2072-2081.

Lim, S. S., T. Vos, A. D. Flaxman, G. Danaei, K. Shibuya, H. Adair-Rohani, M. A. Al-Mazroa, M. Amann, H. R. Anderson, K. G. Andrews, et al. (2012), A comparative risk assessment of burden of disease and injury attributable to 67 risk factors and risk factor clusters in 21 regions, 1990–2010: a systematic analysis for the global burden of disease study 2010, The lancet, 380(9859), 2224–2260.

Lin, M., A. M. Fiore, L. W. Horowitz, O. R. Cooper, V. Naik, J. Holloway, B. J. Johnson, A. M. Middlebrook, S. J. Oltmans, I. B. Pollack, et al. (2012), Transport of asian ozone pollution into surface air over the western united states in spring, J. Geophys. Res., 117(D21).

Liu, H., Liao, J., Yang, D., Du, X., Hu, P., Yang, Y., & Li, B. (2014). The response of human thermal perception and skin temperature to step-change transient thermal environments. *Building and environment*, *73*, 232-238.

Liu, X., Easter, R. C., Ghan, S. J., Zaveri, R., Rasch, P., Shi, X., ... & Conley, A. (2012). Toward a minimal representation of aerosols in climate models: Description and evaluation in the Community Atmosphere Model CAM5. Geoscientific Model Development, 5(3), 709.

Lu, X., Hu, Y., Trepte, C., Zeng, S., & Churnside, J. H. (2014). Ocean subsurface studies with the CALIPSO spaceborne lidar. Journal of Geophysical Research: Oceans, 119(7), 4305-4317.

Ma, P. L., Rasch, P. J., Fast, J. D., Easter, R. C., Gustafson Jr, W. I., Liu, X., ... & Singh, B. (2014). Assessing the CAM5 physics suite in the WRF-CAM5 model: Implementation, resolution sensitivity, and a first evaluation for a regional case study. Geoscientific Model Development, 7(3), 755.

Mahmud, A., M. Hixson, J. Hu, Z. Zhao, S.-H. Chen, and M. Kleeman (2010), Climate impact on airborne particulate matter concentrations in california using seven year analysis periods, Atmos. Chem. Phys., 10(22), 11,097–11,114.

Maria, S. F., Russell, L. M., Gilles, M. K., & Myneni, S. C. (2004). Organic aerosol growth mechanisms and their climate-forcing implications. Science, 306(5703), 1921-1924.

Matthews, T. K., Wilby, R. L., & Murphy, C. (2017). Communicating the deadly consequences of global warming for human heat stress. Proceedings of the National Academy of Sciences, 201617526.

Meehl, G. A., Arblaster, J. M., & Tebaldi, C. (2005). Understanding future patterns of increased precipitation intensity in climate model simulations. Geophysical Research Letters, 32(18).

Meehl, G. A., & Tebaldi, C. (2004). More intense, more frequent, and longer lasting heat waves in the 21st century. Science, 305(5686), 994-997.

Meehl, G. A., Tebaldi, C., Tilmes, S., Lamarque, J. F., Bates, S., Pendergrass, A., & Lombardozzi, D. (2018). Future heat waves and surface ozone. *Environmental Research Letters*, 13(6), 064004.

Meyer, K., Platnick, S., Oreopoulos, L., & Lee, D. (2013). Estimating the direct radiative effect of absorbing aerosols overlying marine boundary layer clouds in the southeast Atlantic using MODIS and CALIOP. Journal of Geophysical Research: Atmospheres, 118(10), 4801-4815. Miao, Y., J. Guo, S. Liu, H. Liu, Z. Li, W. Zhang, and P. Zhai (2017), Classification

of summertime synoptic patterns in beijing and their associations with boundary layer structure affecting aerosol pollution, Atmos. Chem. Phys., 17(4), 3097–3110.

McFiggans, G., Plane, J. M., Allan, B. J., Carpenter, L. J., Coe, H., & O'Dowd, C. (2000). A modeling study of iodine chemistry in the marine boundary layer. Journal of Geophysical Research: Atmospheres, 105(D11), 14371-14385.Miller, N. L., Hayhoe, K., Jin, J., & Auffhammer, M. (2008). Climate, extreme heat, and electricity demand in California. Journal of Applied Meteorology and Climatology, 47(6), 1834-1844.

Mishra, V., Mukherjee, S., Kumar, R., & Stone, D. A. (2017). Heat wave exposure in India in current, 1.5 C, and 2.0 C worlds. *Environmental Research Letters*, *12*(12), 124012.

Mitchell, D. M., Thorne, P. W., Stott, P. A., & Gray, L. J. (2013). Revisiting the controversial issue of tropical tropospheric temperature trends. Geophysical Research Letters, 40(11), 2801-2806.

Molina, M. J., and L. T. Molina (2004), Megacities and atmospheric pollution, J Air Waste Manag. Assoc., 54(6), 644–680.

Mora, C., Dousset, B., Caldwell, I. R., Powell, F. E., Geronimo, R. C., Bielecki, C. R., ... & Lucas, M. P. (2017). Global risk of deadly heat. *Nature Climate Change*, *7*(7), 501.

Morrison, H., Thompson, G., & Tatarskii, V. (2009). Impact of cloud microphysics on the development of trailing stratiform precipitation in a simulated squall line: Comparison of one-and two-moment schemes. Monthly weather review, 137(3), 991-1007.

Nawrot, T. S., Torfs, R., Fierens, F., De Henauw, S., Hoet, P. H., Van Kersschaever, G., ... & Nemery, B. (2007). Stronger associations between daily mortality and fine particulate air pollution in summer than in winter: evidence from a heavily polluted region in western Europe. Journal of Epidemiology & Community Health, 61(2), 146-149.

Neu, J. L., & Prather, M. J. (2012). Toward a more physical representation of precipitation scavenging in global chemistry models: Cloud overlap and ice physics and their impact on tropospheric ozone. Atmos. Chem, and Phys., 12, 3289–3310.

Obradovich, N., Migliorini, R., Mednick, S. C., & Fowler, J. H. (2017). Nighttime temperature and human sleep loss in a changing climate. *Science advances*, 3(5), e1601555.

Ogata, T., Ueda, H., Inoue, T., Hayasaki, M., Yoshida, A., Watanabe, S., ... & Kumai, A. (2014). Projected future changes in the Asian monsoon: a comparison of CMIP3 and CMIP5 model results. Journal of the Meteorological Society of Japan. Ser. II, 92(3), 207-225.

Pachauri, R. K., Allen, M. R., Barros, V. R., Broome, J., Cramer, W., Christ, R., ... & Dubash, N. K. (2014). Climate change 2014: synthesis report. Contribution of Working Groups I, II and III to the fifth assessment report of the Intergovernmental Panel on Climate Change (p. 151). Ipcc.

Pai, D. S., Thapliyal, V., & Kokate, P. D. (2004). Decadal variation in the heatwave and cold waves over India during 1971-2000. *Mausam*, *55*(2), 281-292.

Painemal, D., Minnis, P., & Nordeen, M. (2015). Aerosol variability, synoptic-scale processes, and their link to the cloud microphysics over the northeast Pacific during MAGIC. Journal of Geophysical Research: Atmospheres, 120(10), 5122-5139.

Painemal, D., Clayton, M., Ferrare, R., Burton, S., Josset, D., & Vaughan, M. (2019). Novel aerosol extinction coefficients and lidar ratios over the ocean from CALIPSO–CloudSat: evaluation and global statistics. Atmospheric Measurement Techniques, 12(4), 2201-2217.

Park, S., & Bretherton, C. S. (2009). The University of Washington shallow convection and moist turbulence schemes and their impact on climate simulations with the Community Atmosphere Model. Journal of Climate, 22(12), 3449-3469.

Parrish, D., K. Aikin, S. Oltmans, B. Johnson, M. Ives, and C. Sweeny (2010), Impact of transported background ozone inflow on summertime air quality in a california ozone exceedance area, Atmos. Chem. and Phys., 10(20), 10,093.

Parthasarathy, B., K. R. Kumar, and N. Sontakke (1990), Surface and upper air temperatures over india in relation to monsoon rainfall, Theor. Appl. Climatol., 42(2), 93–110.

Peckham, S. E. (2012). WRF/Chem version 3.3 user's guide.

Peckham, S. E., Grell, G. A., McKeen, S. A., Ahmadov, R., Wong, K. Y., Barth, M., ... & Ghan, S. J. (2017). WRF-CAM5 Version 3.8. 1 User's Guide January 2017.

Petäjä, T., L. Järvi, V.-M. Kerminen, A. Ding, J. Sun, W. Nie, J. Kujansuu, A. Virkkula, X. Yang, C. Fu, et al. (2016), Enhanced air pollution via aerosol-boundary layer feedback in china, Sci. Rep., 6, 18,998.

Petters, M. D., Snider, J. R., Stevens, B., Vali, G., Faloona, I., & Russell, L. M. (2006). Accumulation mode aerosol, pockets of open cells, and particle nucleation in the remote subtropical Pacific marine boundary layer. Journal of Geophysical Research: Atmospheres, 111(D2).

Phoenix, D. B., Homeyer, C. R., & Barth, M. C. (2017). Sensitivity of simulated convection-driven stratosphere-troposphere exchange in WRF-Chem to the choice of physical and chemical parameterization. Earth and Space Science, 4(8), 454-471.

Pillai, P. S., Babu, S. S., & Moorthy, K. K. (2002). A study of PM, PM10 and PM2.5 concentration at a tropical coastal station. Atmospheric Research, 61(2), 149-167.

Platnick, S., King, M. D., Ackerman, S. A., Menzel, W. P., Baum, B. A., Riédi, J. C., & Frey, R. A. (2003). The MODIS cloud products: Algorithms and examples from Terra. IEEE Transactions on Geoscience and Remote Sensing, 41(2), 459-473.

Pommier, M., Fagerli, H., Gauss, M., Simpson, D., Sharma, S., Sinha, V., ... & Wind, P. (2018). Impact of regional climate change and future emission scenarios on surface O 3 and PM 2.5 over India. Atmospheric Chemistry and Physics, 18(1), 103-127.

Puviarasan, N., Sharma, A. K., Ranalkar, M., & Giri, R. K. (2015). Onset, advance and withdrawal of southwest monsoon over Indian subcontinent: A study from precipitable water measurement using ground based GPS receivers. Journal of Atmospheric and Solar-Terrestrial Physics, 122, 45-57.

Qian, Z., He, Q., Lin, H. M., Kong, L., Bentley, C. M., Liu, W., & Zhou, D. (2008). High temperatures enhanced acute mortality effects of ambient particle pollution in the "oven" city of Wuhan, China. Environmental health perspectives, 116(9), 1172-1178.

Querol, X., A. Alastuey, S. Rodriguez, F. Plana, E. Mantilla, and C. R. Ruiz (2001), Monitoring of pm10 and pm2.5 around primary particulate anthropogenic emission sources, Atmos. Environ., 35(5), 845–858.

Rajput, P., Gupta, T., & Kumar, A. (2016). The diurnal variability of sulfate and nitrate aerosols during wintertime in the Indo-Gangetic Plain: implications for heterogeneous phase chemistry. RSC Advances, 6(92), 89879-89887

Rana, A., Uvo, C. B., Bengtsson, L., & Sarthi, P. P. (2012). Trend analysis for rainfall in Delhi and Mumbai, India. Climate dynamics, 38(1-2), 45-56.

Randles, C. A., Da Silva, A. M., Buchard, V., Colarco, P. R., Darmenov, A., Govindaraju, R., ... & Shinozuka, Y. (2017). The MERRA-2 aerosol reanalysis, 1980 onward. Part I: System description and data assimilation evaluation. Journal of Climate, 30(17), 6823-6850.

Rao, S., Klimont, Z., Smith, S. J., Van Dingenen, R., Dentener, F., Bouwman, L., ... & Reis, L. A. (2017). Future air pollution in the Shared Socio-economic Pathways. Global

Environmental Change, 42, 346-358.Ren, C., Williams, G. M., & Tong, S. (2006). Does particulate matter modify the association between temperature and cardiorespiratory diseases?. *Environmental health perspectives*, *114*(11), 1690.

Ren, C., Williams, G. M., & Tong, S. (2006). Does particulate matter modify the association between temperature and cardiorespiratory diseases?. Environmental health perspectives, 114(11), 1690-1696.

Reichle, R. H., Draper, C. S., Liu, Q., Girotto, M., Mahanama, S. P., Koster, R. D., & De Lannoy, G. J. (2017). Assessment of MERRA-2 land surface hydrology estimates. Journal of Climate, 30(8), 2937-2960.

Roberts, G., Mauger, G., Hadley, O., & Ramanathan, V. (2006). North American and Asian aerosols over the eastern Pacific Ocean and their role in regulating cloud condensation nuclei. Journal of Geophysical Research: Atmospheres, 111(D13).

Rocklov, J., Barnett, A. G., & Woodward, A. (2012). On the estimation of heat-intensity and heat-duration effects in time series models of temperature-related mortality in Stockholm, Sweden. Environmental Health, 11(1), 23.

Rohde, R. A., and R. A. Muller (2015), Air pollution in china: mapping of concentrations and sources, PloS one, 10(8), e0135,749.

Russo, S., Sillmann, J., & Sterl, A. (2017). Humid heat waves at different warming levels. *Scientific reports*, *7*(1), 7477.

Schnell, J. L., & Prather, M. J. (2017). Co-occurrence of extremes in surface ozone, particulate matter, and temperature over eastern North America. *Proceedings of the National Academy of Sciences*, *114*(11), 2854-2859.

Sharma, A. R., Kharol, S. K., Badarinath, K. V. S., & Singh, D. (2010). Impact of agriculture crop residue burning on atmospheric aerosol loading--a study over Punjab State, India. Annales Geophysicae (09927689), 28(2).

Sharmila, S., S. Joseph, A. Sahai, S. Abhilash, and R. Chattopadhyay (2015), Future projection of indian summer monsoon variability under climate change scenario: An assessment from cmip5 climate models, Glob. Planet. Change, 124, 62–78.

Sherwood, S. C., & Huber, M. (2010). An adaptability limit to climate change due to heat stress. *Proceedings of the National Academy of Sciences*, *107*(21), 9552-9555.

Sherwood, S., & Fu, Q. (2014). A drier future?. *Science*, 343(6172), 737-739.

Shi, Y., Gao, X., Xu, Y., Giorgi, F., & Chen, D. (2016). Effects of climate change on heating and cooling degree days and potential energy demand in the household sector of China. Climate Research, 67(2), 135-149.

Shrivastava, M., Fast, J., Easter, R., Gustafson Jr, W. I., Zaveri, R. A., Jimenez, J. L., ... & Hodzic, A. (2011). Modeling organic aerosols in a megacity: comparison of simple and complex representations of the volatility basis set approach. Atmospheric Chemistry & Physics, 11(13).

Skamarock, W. C., Klemp, J. B., Dudhia, J., Gill, D. O., Barker, D. M., Wang, W., & Powers, J. G. (2005). A description of the Advanced Research WRF version 2. NCAR Tech (p. 88). Note NCAR/TN-4681STR.

Sreekanth, V., B. Mahesh, and K. Niranjan (2017), Satellite remote sensing of fine particulate air pollutants over indian mega cities, Adv. Space Res., 60(10), 2268–2276.

Stafoggia, M., Schwartz, J., Forastiere, F., & Perucci, C. A. (2008). Does temperature modify the association between air pollution and mortality? A multicity case-crossover analysis in Italy. *American journal of epidemiology*, *167*(12), 1476-1485.

Stull, R. (2011). Wet-bulb temperature from relative humidity and air temperature. *Journal of Applied Meteorology and Climatology*, *50*(11), 2267-2269.

Tai, A. P., L. J. Mickley, D. J. Jacob, E. Leibensperger, L. Zhang, J. A. Fisher, and H. Pye (2012), Meteorological modes of variability for fine particulate matter (pm2.5) air quality in the united states: implications for pm2.5 sensitivity to climate change, Atmos. Chem. and Phys., 12(6), 3131–3145.

Tang, G., J. Zhang, X. Zhu, T. Song, C. Münkel, B. Hu, K. Schäfer, Z. Liu, J. Zhang, L. Wang, et al. (2016), Mixing layer height and its implications for air pollution over beijing, china, Atmos. Chem. Phys., 16(4), 2459–2475.

Tao, M., L. Chen, Z. Wang, P. Ma, J. Tao, and S. Jia (2014), A study of urban pollution and haze clouds over northern china during the dusty season based on satellite and surface observations, Atmos. environ., 82, 183–192.

Tecer, L. H., O. Alagha, F. Karaca, G. Tuncel, and N. Eldes (2008), Particulate matter (pm2.5, pm10-2.5, and pm10) and children's hospital admissions for asthma and respiratory diseases: A bidirectional case-crossover study, J. Toxicol. Environ. Health, 71(8), 512–520.

Tewari, M., Chen, F., Wang, W., Dudhia, J., LeMone, M. A., Mitchell, K., ... & Cuenca, R. H. (2004, January). Implementation and verification of the unified NOAH land surface model in the WRF model. In 20th conference on weather analysis and forecasting/16th conference

on numerical weather prediction (Vol. 1115, No. 6). Seattle, WA: American Meteorological Society.

Tie, X., Madronich, S., Walters, S., Edwards, D. P., Ginoux, P., Mahowald, N., ... & Brasseur, G. (2005). Assessment of the global impact of aerosols on tropospheric oxidants. Journal of Geophysical Research: Atmospheres, 110(D3).

Tiwari, S., Srivastava, A. K., Bisht, D. S., Bano, T., Singh, S., Behura, S., ... & Padmanabhamurty, B. (2009). Black carbon and chemical characteristics of PM 10 and PM 2.5 at an urban site of North India. Journal of Atmospheric Chemistry, 62(3), 193-209.

Tiwari, S., Srivastava, A. K., Bisht, D. S., Parmita, P., Srivastava, M. K., & Attri, S. D. (2013). Diurnal and seasonal variations of black carbon and PM2. 5 over New Delhi, India: influence of meteorology. Atmospheric Research, 125, 50-62.

Tomaz, S., Cui, T., Chen, Y., Sexton, K. G., Roberts, J. M., Warneke, C., ... & Turpin, B. J. (2018). Photochemical cloud processing of primary wildfire emissions as a potential source of secondary organic aerosol. Environmental science & technology, 52(19), 11027-11037.Turner, M. C., Krewski, D., Pope III, C. A., Chen, Y., Gapstur, S. M., & Thun, M. J. (2011). Long-term ambient fine particulate matter air pollution and lung cancer in a large cohort of never-smokers. American journal of respiratory and critical care medicine, 184(12), 1374-1381.

US Census, 2010. www.census.gov

Van Donkelaar, A., Martin, R. V., Leaitch, W. R., Macdonald, A. M., Walker, T. W., Streets, D. G., ... & Huley, G. (2008). Analysis of aircraft and satellite measurements from the Intercontinental Chemical Transport Experiment (INTEX-B) to quantify long-range transport of East Asian sulfur to Canada.

Van Oldenborgh, G. J., Otto, F. E., Haustein, K., & AchutaRao, K. (2016). The heavy precipitation event of December 2015 in Chennai, India. Bulletin of the American Meteorological Society, 97(12), S87-S91.

Van Oldenborgh, G., Philip, S., Kew, S., van Weele, M., Uhe, P., Otto, F., AchutaRao, K., (2017). Extreme heat in India and anthropogenic climate change. *Nat. Hazards Earth Syst. Sci*. 107, 1–23.

Venkataraman, C., Brauer, M., Tibrewal, K., Sadavarte, P., Ma, Q., Cohen, A., ... & Millet, D. B. (2018). Source influence on emission pathways and ambient PM 2.5 pollution over India (2015–2050). Atmos. Chem. and Phys, 18(11), 8017-8039.

WHO. 2005. Air quality guidelines - global updates 2005. http://www.euro.who.int/__data/assets/pdf_file/0005/78638/E90038.pdf?ua=1

WHO (2017). Air Pollution. Retrieved from http://www.who.int/airpollution/en/

Wiedinmyer, C., Akagi, S. K., Yokelson, R. J., Emmons, L. K., Al-Saadi, J. A., Orlando, J. J., & Soja, A. J. (2011). The Fire INventory from NCAR (FINN): A high resolution global model to estimate the emissions from open burning. Geoscientific Model Development, 4(3), 625.

Wilby, R. L. (2008). Constructing climate change scenarios of urban heat island intensity and air quality. *Environment and Planning B: Planning and Design*, *35*(5), 902-919.

Wild, O., Zhu, X., & Prather, M. J. (2000). Fast-J: Accurate simulation of in-and below-cloud photolysis in tropospheric chemical models. Journal of Atmospheric Chemistry, 37(3), 245-282.

Willers, S. M., Jonker, M. F., Klok, L., Keuken, M. P., Odink, J., van den Elshout, S., ... & Burdorf, A. (2016). High resolution exposure modelling of heatwave and air pollution and the impact on mortality. *Environment international*, *89*, 102-109.

Willett, K. M., & Sherwood, S. (2012). Exceedance of heat index thresholds for 15 regions under a warming climate using the wet-bulb globe temperature. International Journal of Climatology, 32(2), 161-177.

Wu, X., Xu, Y., Kumar, R., & Barth, M. (2019). Separating Emission and Meteorological Drivers of Mid-21st-Century Air Quality Changes in India Based on Multi year Global-Regional Chemistry-Climate Simulations. Journal of Geophysical Research: Atmospheres, 124(23), 13420-13438.

Xiao, H., Mechoso, C. R., Sun, R., Han, J., Pan, H. L., Park, S., ... & Teixeira, J. (2014). Diagnosis of the marine low cloud simulation in the NCAR community earth system model (CESM) and the NCEP global forecast system (GFS)-modular ocean model v4 (MOM4) coupled model. Climate Dynamics, 43(3-4), 737-752.

Xu, Y., & Lamarque, J. F. (2018). Isolating the meteorological impact of 21st century GHG warming on the removal and atmospheric loading of anthropogenic fine particulate matter pollution at global scale. *Earth's Future*, *6*(3), 428-440.

Xu, Y., Lamarque, J. F., & Sanderson, B. M. (2018). The importance of aerosol scenarios in projections of future heat extremes. Climatic Change, 146(3-4), 393-406.

Xu, Y., Wu, X., Kumar, R., Barth, M., Diao, C., Gao, M., ... & Meehl, G. A. (2020). Substantial Increase in the Joint Occurrence and Human Exposure of Heatwave and High-PM Hazards Over South Asia in the Mid-21st Century. AGU Advances, 1(2), e2019AV000103.

Yamamoto, M. K., Furuzawa, F. A., Higuchi, A., & Nakamura, K. (2008). Comparison of diurnal variations in precipitation systems observed by TRMM PR, TMI, and VIRS. Journal of Climate, 21(16), 4011-4028.

Yang, Y., H. Wang, S. J. Smith, R. Zhang, S. Lou, Y. Qian, P.-L. Ma, and P. J. Rasch (2018), Recent intensification of winter haze in china linked to foreign emissions and meteorology, Sci. Rep., 8(1), 2107.

Yin, H., & Sun, Y. (2018). Detection of anthropogenic influence on fixed threshold indices of extreme temperature. Journal of Climate, 31(16), 6341-6352.

Zaveri, R. A., R. C. Easter, and A. S. Wexler (2005), A new method for multicomponent activity coefficients of electrolytes in aqueous atmospheric aerosols, J. Geophys. Res., 110, D02201.

Zaveri, R. A., Easter, R. C., Fast, J. D., & Peters, L. K. (2008). Model for simulating aerosol interactions and chemistry (MOSAIC). Journal of Geophysical Research: Atmospheres, 113(D13).

Zhang, R., Wang, Y., Smeltzer, C., Qu, H., Koshak, W., & Boersma, K. F. (2018). Comparing OMI-based and EPA AQS in situ NO 2 trends: towards understanding surface NO x emission changes. Atmospheric Measurement Techniques, 11(7), 3955-3967.

Zhang, X., Q. Zhang, C. Hong, Y. Zheng, G. Geng, D. Tong, Y. Zhang, and X. Zhang (2018), Enhancement of pm2.5 concentrations by aerosol-meteorology interactions over china, J. Geophys. Res., 123(2), 1179–1194.

Zhang, Y., Zhang, X., Wang, K., He, J., Leung, L. R., Fan, J., & Nenes, A. (2015). Incorporating an advanced aerosol activation parameterization into WRF-CAM5: Model evaluation and parameterization intercomparison. Journal of Geophysical Research: Atmospheres, 120(14), 6952-6979.

Ziemke, J., S. Chandra, L. Oman, and P. Bhartia (2010), A new enso index derived from satellite measurements of column ozone, Atmos. Chem. Phys., 10(8), 3711–3721.

Zou, Y., Y. Wang, Y. Zhang, and J.-H. Koo (2017), Arctic sea ice, eurasia snow, and extreme winter haze in china, Sci. Adv., 3(3), e1602,751.

Zveryaev, I. I. (2002). Interdecadal changes in the zonal wind and the intensity of intraseasonal oscillations during boreal summer Asian monsoon. Tellus A: Dynamic Meteorology and Oceanography, 54(3), 288-298.